thermo scientific

Materials Analysis Applications Compendium • 2017

FTIR • Raman • NMR • NIR • Extrusion • Rheology

ThermoFisher
SCIENTIFIC

Contents

FTIR	Analysis of artists' pigments by far-infrared microspectroscopy	3
	Attenuated total reflection FTIR imaging of "soft chew" formulations	7
	Protein secondary structure elucidation using FTIR spectroscopy	10
NIR	A case study of using FT-NIR for pharmaceutical hot melt extrusion process monitoring	14
NMR	Measuring the equilibrium constant of a keto-enol tautomerism using benchtop NMR	20
	Benchtop NMR combined with GC/MS confirms identity of forensic case sample	23
	Determination of polymer molecular weight and composition using picoSpin NMR spectroscopy	28
	Qualitative and quantitative analysis of the polymerization of PS-b-PtBA block copolymer using picoSpin 80 NMR	32
	Analysis of acetanilide herbicides and their rotational isomers by picoSpin 80 NMR	36
	Hydrogen content determination by picoSpin NMR	40
	Evaluation of fluoroorganic compounds with benchtop ^{19}F NMR	44
Raman	Classification of polyethylene by Raman spectroscopy	48
	FT-Raman: an invaluable addition to the forensic arsenal to combat the opioid epidemic	54
	Leveraging the lateral spatial resolution of a confocal Raman microscope to resolve micron to sub-micron layers in polymer laminates	57
	FT-Raman mapping of multicomponent solid dosage forms	61
	Characterizing amber and its imitations with dispersive Raman spectroscopy	64
	Confocal Raman analysis of a transdermal nicotine patch by a DXR2 Raman Microscope	67
	In situ density determination of polyethylene in multilayer polymer films using Raman microscopy	71
RheoRaman	Simultaneous rheology and Raman spectroscopy during the melting and recrystallization of polypropylene	77
	Investigating cocoa butter crystallization using simultaneous rheology and Raman spectroscopy (RheoRaman)	82
Other	Raman and FTIR articles	88

Analysis of artists' pigments by far-infrared microspectroscopy

Authors

David W. Schiering[1], Ron Rubinovitz[2], Anthony W. Didomenico[1], Beth Price[3], and Kate Duffy[3]

1. Czitek, 6 Finance Dr., Danbury, CT 06810
2. Thermo Fisher Scientific, 4410 Lottsford Vista Road, Lanham, MD, 20706
3. Philadelphia Museum of Art, PO Box 7646 Philadelphia, PA 19101

Introduction

The chemical identity of materials used in art pieces is of key importance to their authentication and preservation. By comparing the materials used relative to the time period in which the art was purportedly generated, conservators can quickly distinguish authentic pieces from well-made copies. Furthermore, identification of the materials used can also guide conservators on the proper cleaning and preservation techniques to slow the natural degradation processes of those art pieces. In many cases, it's also important to identify previously applied preservation materials.

Fourier transform infrared (FTIR) spectroscopy is a well-established technique to analyze and identify artists' materials.[1-10] Measurements are typically performed in the mid-IR spectral region (4000-400 cm^{-1}). The KBr optics commonly used in FTIR spectrometers impose a low frequency cutoff at about 400 cm^{-1}. Mercury-cadmium-telluride (MCT) detectors employed in FTIR microscopes further restrict the low frequency cutoff to the 700-500 cm^{-1} range. These low frequency cutoffs limit the effectiveness of mid-IR in identifying many inorganic pigments found in artwork, which often have characteristic absorption bands in the far-IR region (600-10 cm^{-1}). Raman spectroscopy, another primary vibrational spectroscopy technique for the molecular identification of cultural heritage materials, has a standard spectral range well below 400 cm^{-1}. However, fluorescence arising from both pigments and binding media is an often-encountered problem in the analysis of artistic pigments using Raman spectroscopy.[11]

Figure 1: Nicolet iS50 FTIR spectrometer with the SurveyIR microspectroscopy accessory in the sample compartment.

The utility of far-IR spectroscopic characterization of pigment materials has been demonstrated for macro samples.[12-15] The far-IR microspectroscopy analysis of pigments, however, has been an unexploited field due to such challenges as the low radiance of thermal sources, relatively low responsivity of room temperature detectors, and reduction of throughput by aperture masks. Recent advances in optical materials and design have overcome many of these challenges and opened the far-IR region for the microspectroscopic application in pigment characterization. In this application note, we demonstrate the microspectroscopic analysis of a number of pigments using the Thermo Scientific™ Nicolet™ iS50 FTIR Spectrometer and the Czitek™ SurveyIR™ Microspectroscopy Accessory (Figure 1).

Experimental

Measurements were done in attenuated total reflectance (ATR) mode using the SurveyIR diamond ATR attachment, or by reflectance with the samples on a low-E glass microscope slides. Spectra were collected using 256 scans at 8 cm^{-1} spectral resolution. Mid-IR spectra were measured using a Ge on KBr beamsplitter and DLaTGS detector with a KBr window allowing collection from 4000 to 400 cm^{-1}. Far-IR spectra in the range of 1800-50 cm^{-1} were collected using a solid substrate beamsplitter and a DLaTGS detector with a polyethylene window. Polyethylene is commonly used as a window material in the far-IR, but its strong absorbances around 1460 cm^{-1} and 770 cm^{-1} do not allow measurements in these specific regions. Changing the beamsplitter between measurements was easily accomplished with the automatic beamsplitter exchanger (ABX) on the Nicolet iS50 spectrometer. The unique ABX design allows automated switching between measurement modes with no loss of purge. No modifications of the SurveyIR accessory were necessary to allow it to measure spectra in both mid- and far-IR regions.

Results and Discussion

To demonstrate the utility of the far-IR method and performance, mid- and far-IR spectra of a coated paperboard were collected. The coating on the paperboard contained calcium carbonate ($CaCO_3$), kaolinite ($Al_2O_3 \cdot 2SiO_2 \cdot 2H_2O$), and a polyester binder. The coating spectra were collected in two modes using the SurveyIR diamond ATR microspectroscopy attachment. First, a spectrum was collected using a conventional KBr substrate beamsplitter and KBr window DLaTGS detector. This spectrum is displayed in Figure 2B in the 1850-400 cm^{-1} region. The optical configuration of the FTIR was then changed to the far-IR mode. The IR spectrum using this configuration was measured from 1850-50 cm^{-1} and is displayed in Figure 2C. The overall spectral quality and signal-to-noise ratios are quite satisfactory. Numerous absorption bands originating from calcium carbonate and kaolinite are observed below 400 cm^{-1} outside of the range of MCT detector and KBr window cut-offs. While these inorganic materials also exhibit features in the mid-IR, extending the range into the far-IR region provides more spectral details that can be beneficial in identifying materials or components in mixtures.

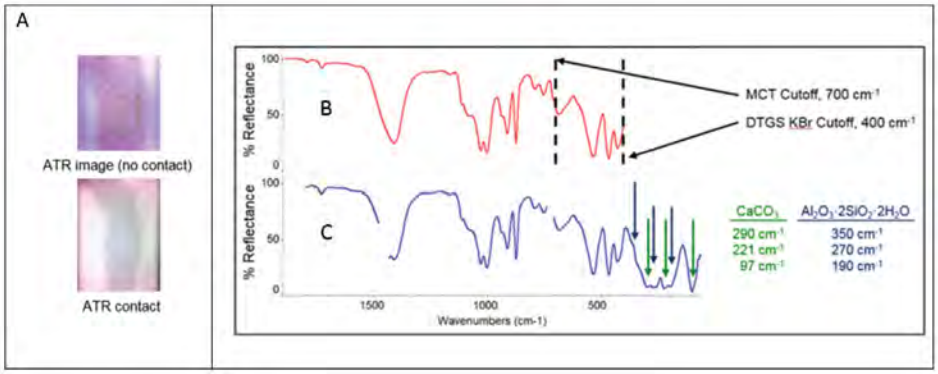

Figure 2: Measurement of coated paperboard by ATR. (A) Image of sample area through diamond ATR crystal before and after contact, allowing the user to verify the sample area being measured. (B) Mid-IR spectra with characteristic low end cut-offs of MCT and DLaTGS detectors indicated by dashed lines. (C) Spectral features seen in the far-IR spectrum indicative of calcium carbonate and kaolinite seen below the KBr and MCT low wavenumber cut-offs. Spectral regions around 1460 and 770 cm^{-1} are blanked due to the strong absorbance of polyethylene detector window at these locations.

The mid-IR and far-IR spectra of a modern paint are shown in Figure 3, as another comparison. These spectra were recorded using the SurveyIR diamond ATR microspectroscopy attachment. The observed mid-IR spectrum is consistent with polymers of ethyl acrylate and methyl methacrylate,[16-18] typical for a modern polymer-based paint binder. However, the far-IR spectrum allows the identification of the inorganic pigment, zinc oxide, or "zinc white" since it contains a characteristic absorbance peak at 380 cm^{-1}. Clearly, measurement of the mid-IR spectrum alone would not allow for a positive identification of zinc white.

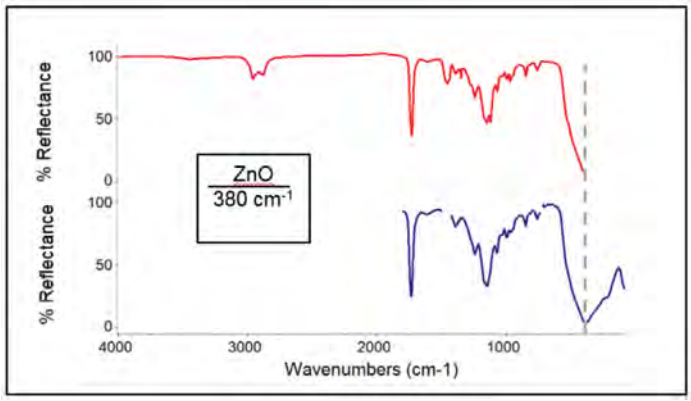

Figure 3: White paint containing zinc oxide. Top: Mid-IR spectrum showing only shoulder of zinc oxide absorption at 380 cm^{-1} (dashed line). Bottom: Far-IR spectrum clearly showing zinc oxide's absorption peak at 380 cm^{-1}.

Far-IR microspectroscopy was also employed in the analysis of pigments from a furniture piece in the collections of the Philadelphia Museum of Art (PMA). The piece, a wardrobe shown in Figure 4, was purportedly fabricated in China in the 18th century during the Qing dynasty. To help plan the conservation treatments, the decorative surfaces were analyzed to determine whether they are consistent with the 18th century in China or are later additions. A cross-section from a sample taken from an interior portion of the wardrobe is also shown in Figure 4.

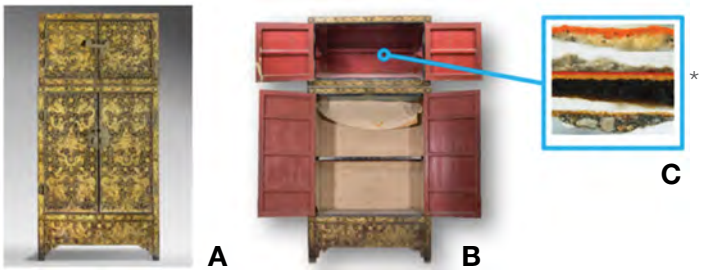

Figure 4. Qing dynasty lacquer clothes wardrobe and inset shows a cross-section from the interior used for analysis. (A) Exterior, (B) interior, and (C) cross-section analyzed from the compound wardrobe. The asterisk represents the original decorative surface. The layers above this point are later additions. *Accession number: 1940-7-2, Philadelphia Museum of Art; Artist/maker unknown Qing Dynasty (1644–1911); Lacquered wood with painted and gilt decoration; brass fittings. Purchased with the Bloomfield Moore Fund, 1940.*

Far-IR microanalysis was performed on the red and yellow layers of the cross-section. The images obtained from the red pigment particles are shown in Figure 5, Section A. Spectra of the red layer obtained by diamond ATR microscopy and a vermilion reference are shown in Figure 5, sections B and C, respectively. The vermilion reference was from the Forbes pigment collection at Harvard University.[19] The two spectra exhibit a high degree of similarity and confirm a positive identification. Vermilion is produced from the mineral cinnabar, HgS, mercury (II) sulfide. The observed bands are consistent with those from trigonal α-mercuric sulfide (cinnabar mineral) and are attributed to the lattice vibrations of the crystal.[20] Vermilion was a common red pigment used in the production of Chinese lacquerware[21] and its presence provides critical evidence of the wardrobe's authenticity. The captured images of the yellow particles (A), the far-IR spectra of the yellow lacquer layer pigment (B), and orpiment reference (As_2S_3) (C) are shown in Figure 6. Both spectra were recorded in the external reflectance mode from samples flattened onto low-E glass substrates. An aperture mask corresponding to 250 microns at the sample was used to target the pigment extracted from the yellow layer. The reference orpiment pigment was also from the Forbes collection. Orpiment is a mineral produced geothermally and was used as a yellow pigment from antiquity into the early 20th century. Prominent absorption bands are indicated in the figure. The absorption bands between the yellow pigment and the orpiment reference spectrum match well and agree with previous reports.[22-23] The results unequivocally indicate that the yellow pigment is orpiment. In the cases of both pigments, the lack of features in the mid-IR regions underscores the importance of far-IR measurements.

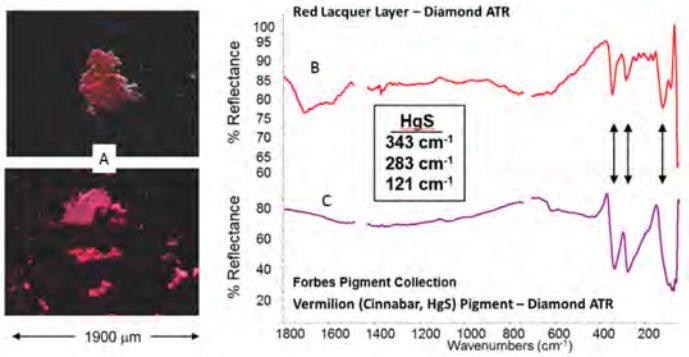

Figure 5: Far-IR ATR spectra: (A) images of red pigment extracted from wardrobe sample, (B) far-IR ATR spectrum of wardrobe sample and (C) vermillion reference.

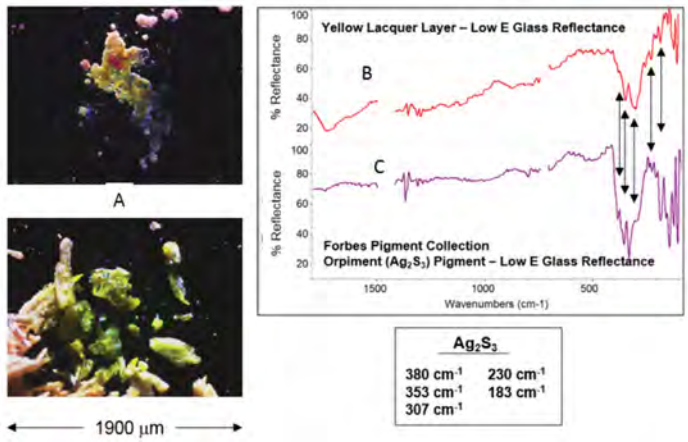

Figure 6: Far-IR ATR spectra: (A) images of yellow pigment extracted from the wardrobe sample, (B) far-IR reflectance spectrum of yellow wardrobe sample and (C) orpiment reference.

Conclusions

Mid-IR FTIR spectroscopy is an effective analytical tool for artworks, and the combination with microscopy is particularly beneficial as minimal sample is required for analysis. However, many materials, particularly pigments containing inorganic components, cannot be fully characterized with FTIR microscopes configured only for mid-IR operation. The analyses of zinc white and two layers of an antique artifact demonstrate the benefits of combining far-IR spectroscopy with microspectroscopy accessories, which allow for more insightful characterization of pigment materials. The chemical information gleaned from the interpretation of these spectra can be used to establish authenticity through dating of artworks, characterize previous conservation attempts, and plan new conservation campaigns.

thermo scientific

References

1. *Infrared Spectroscopy in Conservation Science*, Michele R. Derrick, Dusan Stulik, and James M. Landry, J. Paul Getty Trust, Getty Conservation Institute, Los Angeles, 1999.
2. Meiluna, Raymond J., James G. Bentson, and Arthur Steinberg. *Analysis of Aged Paint Binders by FTIR Spectroscopy.* Studies in Conservation 35 (1990).
3. Sloggett, Robyn, Caroline Kyi, Nicole Tse, Mark J. Tobin, Ljiljana Puskar, and Stephen P. Best. *Microanalysis of Artworks: IR Microspectroscopy of Paint Cross-sections.* Vibrational Spectroscopy 53.1 (2010): 77-82.
4. Newman, Richard. *Some Applications of Infrared Spectroscopy in the Examination of Paintings Materials*. Journal of the American Institute for Conservation 19.1 (1979): 42-62.
5. Manzano, E., N. Navas, R. Checamoreno, L. Rodriguez-Simon, and L.F. Capitan-Vallvey. *Preliminary Study of UV Ageing Process of Proteinaceous Paint Binder by FTIR and Principal Component Analysis.* Talanta 77.5 (2009): 1724-731.
6. Jonsson, Julia, and Tom Learner. *Separation of Acrylic Paint Components and Their Identification with FTIR Spectroscopy.* Proceedings of the Sixth Infrared and Raman Users Group Conference (IRUG6). Florence, Italy March 29th-April 1st 2004. Ed. Marcello Picollo. Florence: Il Prato, 2005. 58-68.
7. Hodson, J., and J.A. Lander. *The Analysis of Cured Paint Media and a Study of the Weathering of Alkyd Paints by Fourier Transform Infra-red/photoacoustic Spectroscopy.* Polymer 28.2 (1987): 251-56.
8. Lang, Patricia L., Chad D. Keefer, Jessica C. Juenemann, Khoa V. Tran, Scott M. Peters, Nancy M. Huth, and Alain G. Joyaux. *The Infrared Microspectroscopic and Energy Dispersive X-ray Analysis of Paints Removed from a Painted, Medieval Sculpture of Saint Wolfgang.* Microchemical Journal 74.1 (2003): 33-46.
9. Olin, J.S. *The Use of Infrared Spectrophotometry in the Examination of Paintings and Ancient Artifacts.* Instrument News 17 (1966): 1.
10. McClure, A., J. Thomson, and J. Tannahill. *Infrared Spectra of Ninety-six Organic Pigments.* Journal of Oil and Colour Chemists' Association 51 (1968)
11. López-Gil, Ruiz-Moreno, Miralles. *Optimum acquisition of Raman spectra in pigment analysis with IR laser diode and plulsed UV irradiation* Journal of Raman Spectroscopy. 37 (2006); 966-973
12. Kendix, Elsebeth L., Silvia Prati, Edith Joseph, Giorgia Sciutto, and Rocco Mazzeo. *ATR and Transmission Analysis of Pigments by Means of Far Infrared Spectroscopy.* Analytical and Bioanalytical Chemistry 394 (2009): 1023-032.
13. http://lisa.chem.ut.ee/IR_spectra/
14. Afremow, Leonard C., and John T. Vanderberg. *High Resolution Spectra of Inorganic Pigments and Extenders in the Mid-Infrared Region from 1500 cm^{-1} to 200 cm^{-1}*. Journal of Paint Technology 38.495 (1966): 169-202
15. C. Karr and J. Kovach. *Far-Infrared Spectroscopy of Minerals and Inorganics*. Appl. Spectrosc. 23, 219 (1969).
16. M.R. Nelson, *Authentic or Not*, ChemMatters, April 2011, pp. 15-17.

Find out more at
thermofisher.com/is50 and **thermofisher.com/surveyIR**

ThermoFisher SCIENTIFIC

APPLICATION NOTE AN52813

Attenuated total reflection FTIR imaging of “soft chew” formulations

Author
Ron Rubinovitz, Ph.D.
Thermo Fisher Scientific, USA

Keywords
ATR, FTIR, imaging, microscopy, formulations

Thermo Fisher Scientific solutions
Nicolet iN10 MX Infrared Imaging Microscope

Figure 1: Imaging ATR accessory (left) and Nicolet iN10 MX infrared microscope (right)

Introduction

In recent years, the pharmaceutical formulation type in which the active ingredients are dispersed in a “soft chew” matrix has become increasingly popular for a number of over-the-counter (OTC) dosage forms. The sticky and oily nature of these dosage forms, however, poses a particular challenge in sample handling for FTIR measurements. For example, it is often difficult to cut these samples sufficiently thin for transmission analysis, while simply pressing them flat would destroy the innate component distribution within the samples. Reflectance spectra, on the other hand, tend to be of poor quality. The Attenuated Total Reflectance (ATR) measurement of a sample cross section could offer a potential solution since this technique would expect to yield high quality spectra regardless of sample thickness. The “stickiness” of these samples, however, leads to “sample carry over” and complicates single point ATR mapping. In addition, maps acquired by ATR typically require longer measurement times due to the time required to raise and lower the sample stage at each measurement point.

In this note, we demonstrate the use of an imaging ATR accessory that’s well suited for the analysis of these samples. The accessory makes contact with the sample just once, while still permitting measurements across the sample surface. Additionally, germanium ATR microscope measurements offer the benefit of a four times magnification due to presence of germanium (refractive index n=4) instead of air (n=1) at the sample interface, resulting in enhanced spatial resolution compared to non-ATR measurements.

Experimental

Spectra were measured using a Nicolet iN10 MX infrared imaging microscope (Figure 1), configured with the following detectors: a room temperature DTGS, a single point MCT-A and a linear array MCT-A detector. Each sample cross section was cut to a size of approximately 5 x 5 x 2 mm (l x w x h) and was placed on the sample post of an imaging ATR microscope accessory (Figure 1) and raised to make contact with the germanium ATR crystal for measurement.

Unless otherwise indicated, spectra were collected using the array detector in “ultra-fast” mode where a single scan per step at 16 cm^{-1} resolution was collected at each map point at a spatial resolution of 6.25 microns. Sample and background maps of about 625 x 625 microns consisting of about 11,000 spectra were measured in approximately 1.5 minutes each.

Results

Antacid product component distribution

Representative map spectra and their comparison to the library spectra of pure materials are shown in Figure 2. Examination of individual map spectra showed that each spectrum was dominated by features of a specific sample component, although weaker features of the other major components can also be seen. Maps of the active material (calcium carbonate), and two of the main non-active components, oil and corn syrup based on baseline corrected peak heights at 872, 1746, and 1020 cm^{-1}, respectively are shown in Figure 2. It is clear from the similarities in the active component and corn syrup maps that the calcium carbonate is found primarily in the corn syrup regions.

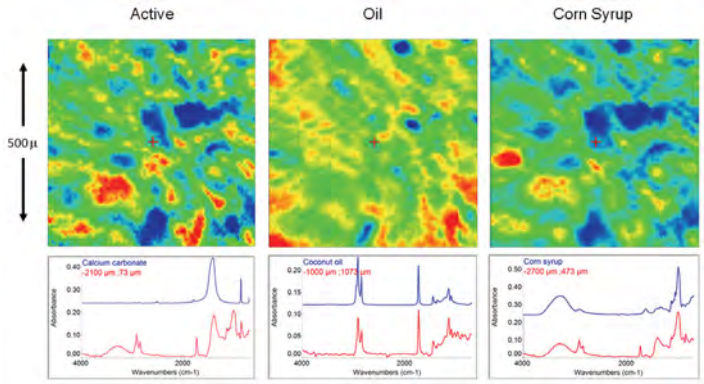

Figure 2: Maps showing distribution of main components of antacid product (top) and representative spectra shown in red, compared to library spectra shown in blue (bottom)

In Figure 3, the quality of the maps created from array spectra is verified by comparing two maps of the same sample measured with array and single point MCT-A detectors, respectively. Each map shows the intensity of the calcium carbonate peak at 872 cm^{-1} and contains approximately 2000 spectra. The array map of single scan spectra at 16 cm^{-1} collected in just 18 seconds shows the same features as the single point detector map collected at 8 cm^{-1} resolution and 16 scans per spectrum that required about two hours to collect.

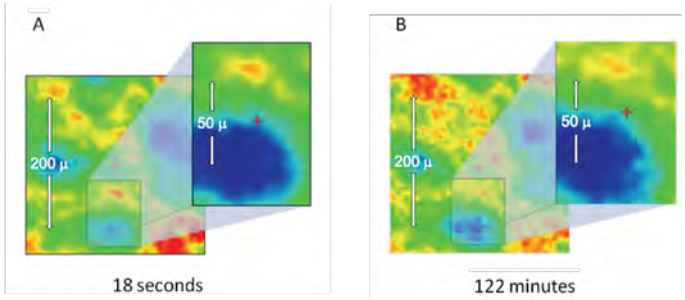

Figure 3: Comparison of maps of active component measured using an array (A) and single point detector (B)

Joint health supplement component distribution

Due to the low spectral intensity of the glucosamine in this product, a multivariate curve resolution (MCR) analysis was performed which readily extracted the spectra of glucosamine and, as expected, the more obvious oil and corn syrup features. The resulting maps are shown in Figure 4, along with the comparison of the MCR components and pure spectra. The minor presence of glucosamine in the measured spectra is demonstrated in Figure 5, using principal component reconstructed spectra. A map spectrum of mostly corn syrup is subtracted from a map spectrum that MCR analysis indicated contained both glucosamine and corn syrup, resulting in spectral features that compare well to the reference spectrum of glucosamine.

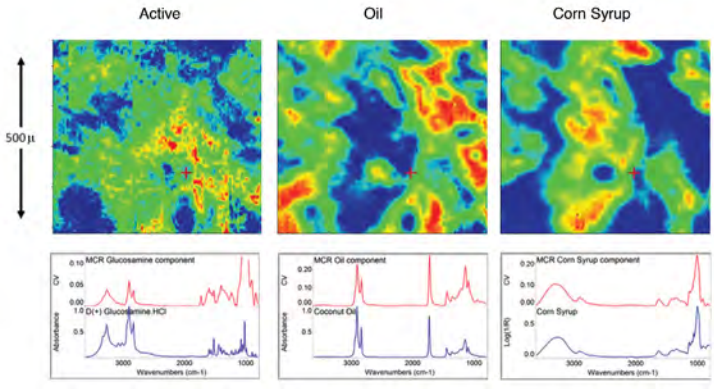

Figure 4: Maps of components obtained with MCR Analysis (top) and MCR components shown in red, compared to library spectra shown in blue (bottom)

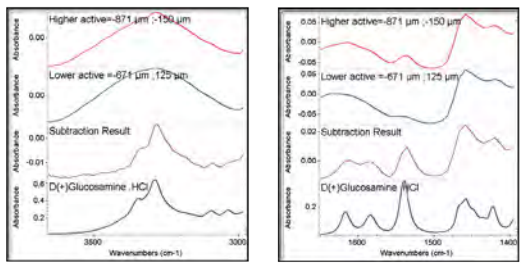

Figure 5: Spectral subtraction confirming the presence of glucosamine as found by MCR analysis

thermo scientific

Conclusions

In this note, the measurement of the key component distribution in two “soft chew” products by ATR FTIR imaging is described. Maps of sample components with relatively intense features were created by straightforward peak-height methods, while significantly weaker features were readily mapped by using MCR techniques. For each sample, the maps were collected in just a few minutes. The improvement in analysis speed was accomplished through the use of an array detector and a “fit-for-purpose” accessory that eliminates the need to raise and lower the microscope stage at each measurement point. The described methodology should have general applicability for QA/QC and analytical laboratories in pharmaceutical, food and associated industries performing similar analyses.

Find out more at **thermofisher.com/ftir**

ThermoFisher SCIENTIFIC

thermo scientific

APPLICATION NOTE AN52985

Protein secondary structure elucidation using FTIR spectroscopy

Author

Suja Sukumaran

Thermo Fisher Scientific, USA

Keywords

FTIR, ATR, protein structure elucidation, Biocell calcium fluoride cell, ConcentrateIR2 ATR, transmission

Abstract

Fourier-transform infrared (FTIR) spectroscopy is one of the most versatile analytical tools used across various disciplines. In this study, the Thermo Scientific™ Nicolet™ iS10 and Nicolet iS50 FTIR spectrometers, equipped with Attenuated Total Reflection (ATR)-FTIR and Transmission-FTIR, were used for the determination of protein secondary structures. Structure calculations based on a protein database as well as spectral deconvolution are discussed. The analyses were quick and easy.

Introduction

Protein secondary structure describes the repetitive conformations of proteins and peptides. There are two major forms of secondary structure, the α-helix and β-sheet, so named by the patterns of hydrogen bonds between amine hydrogen and carbonyl oxygen atoms that create the peptide backbone of a protein.[1] Understanding protein secondary structure is important to gain insight into protein conformation and stability. For example, temperature dependent analysis of the secondary structure is critical in determining storage conditions for maintaining active therapeutic proteins.[2] Protein secondary structure is also crucial in understanding the structure-function relationship and enzyme kinetics of various proteins.[3]

FTIR has long been established as a powerful analytical technique to investigate protein secondary structure and local conformational changes.[1, 4] A typical protein infrared (IR) spectrum often contains nine amide bands, with vibrational contributions from both protein backbone and amino acid side chains. Among which, of particular pertinence to protein secondary structure are Amide I and Amide II bands. The absorptions associated with C=O stretching are denoted as Amide I, whereas those associated with N—H bending are Amide II. Since both C=O and N—H bonds are involved in the hydrogen bonding between different moieties of secondary structure, the positions of both Amide I and Amide II bands are sensitive to the secondary structure composition of a protein,[3, 4] although the Amide II band is widely viewed as a less useful predictor for quantifying the secondary structure of proteins.

ThermoFisher SCIENTIFIC

The shifts in the Amide I band are often small compared to the intrinsic width of the band, resulting in one broad peak instead of a series of resolved peaks for each type of the secondary structure. Mathematical procedures such as Fourier self-deconvolution and second derivatives can be used to resolve the overlapping bands for the quantitative analysis of protein secondary structure.[3] Table 1 shows the secondary structure band assignments for proteins in water. Note that all assignments are depicted as a range, as the exact position of each peak varies from protein to protein due to the differences in hydrogen bonding interactions and the environment of the proteins.

Secondary Structure	Band Assignment in Water
α-Helix	1648-1657 cm^{-1}
β-Sheet (high frequency component)	1623-1641 cm^{-1} 1674-1695 cm^{-1}
Random	1642-1657 cm^{-1}
Coils	1662-1686 cm^{-1}

Table 1: Secondary structure band assignments for protein in water.[2]

With a range of sampling techniques, including transmission, ATR, and infrared reflection absorption spectroscopy (IRRAS), FTIR is particularly advantageous in terms of its versatility and general applicability compared to other analytical techniques for protein secondary structure analysis. Protein sample forms suitable for FTIR analysis include lyophilized powders, water solution, and colloids, to name a few. We report herein two examples of protein secondary structure determination using transmission-FTIR and ATR, respectively. Both methods are fast, consume a minute amount of sample, and require minimal sample preparation.

Experimental

All proteins were procured from Sigma-Aldrich (MO, USA) and used as received. For the transmission studies, a BioCell™ Calcium Fluoride Cell (Biotools, Jupiter, FL) was used, and all measurements were carried out at ambient temperature. A 10 µL protein solution was placed at the center of the window, and the protein solution was sandwiched between the two CaF_2 windows, and placed in the holder. The concentration of protein tested was between 6 and 12 mg/mL. A 6 µm path length was created by sandwiching the two CaF_2 windows. CaF_2 windows are suited for water-based sample analysis. As water has a significant absorption peak at 1645 cm^{-1} region, a small path length of 6 µm can effectively avoid saturated water peaks.

A purged Nicolet iS10 FTIR spectrometer, equipped with a DTGS detector, was used for transmission analysis. The scan parameters used were 256 scans, resolution of 4 cm^{-1}. The Thermo Scientific™ Smart OMNI-Sampler™ Transmission Accessory allows for a quick purge of the chamber, eliminating the need for water vapor subtraction in most analyses. Secondary structure analysis of the buffer-subtracted spectra was carried out using the built-in feature of the PROTA-3S™ FT-IR Protein Structure Analysis Software. Secondary structure calculation in PROTA-3S software is based on a database of 47 secondary structures (for more information visit www.btools.com).

For ATR analysis, a ConcentratIR2™ Multiple Reflection ATR Accessory (Harrick Scientific Products, Inc. Pleasantville, NY) with diamond crystal was used in a Nicolet iS50 FTIR spectrometer equipped with an mercuric cadmium telluride (MCT) detector. The diamond ATR has ten internal reflections with a nominal angle of incidence of 45°. A 10 µL protein solution in phosphate buffer was dried on the surface of the ATR crystal under a stream of nitrogen. Scan parameters used were 256 scans and a resolution of 4 cm^{-1}. Secondary structure determination was carried out using the peak resolve feature of the OMNIC software.

Results and discussion

Transmission-FTIR with Biocell

Figure 1 shows the overlay of three FTIR spectra: phosphate buffer, cytochrome C at 6 mg/mL and 12 mg/mL in phosphate buffer, respectively. At first glance, the spectra are predominantly water bands. The three spectra show little difference, even at a high protein concentration of 12 mg/mL.

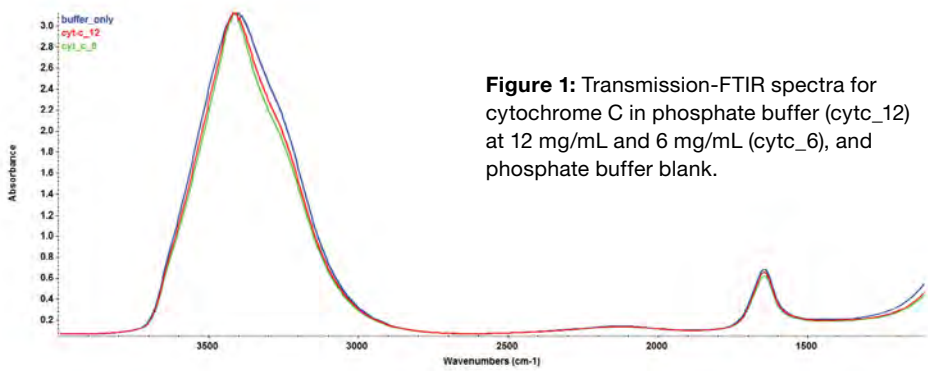

Figure 1: Transmission-FTIR spectra for cytochrome C in phosphate buffer (cytc_12) at 12 mg/mL and 6 mg/mL (cytc_6), and phosphate buffer blank.

Next, the buffer spectrum was subtracted from the raw protein spectra using the PROTA-3S software, and the results are shown Figures 2A (cytochrome C) and 2B (concanavalin). The Amide I and II peaks are clearly discernible in both spectra. The Amide I peak position for cytochrome C spectra is 1654 cm^{-1}, suggesting an α-helix dominant secondary structure. For Concanavalin A, the Amide I peak centers at 1633 cm^{-1}, and there is also a noticeable shoulder peak at 1690 cm^{-1} (red circle), indicative of the β-sheet component and its associated high-frequency component.[2]

Table 2 summarizes the secondary structure prediction using the PROTA-3S software. The cytochrome C has 45% α-helix and 5% β-sheet, whereas Concanavalin A has 42% β-sheet and 4% α-helix. Differences in secondary structure composition between X-ray and FTIR data are likely due to the physicochemical state of the protein samples such as crystalline versus solution, temperature, pH, buffer conditions, etc. Furthermore, different prediction algorithms could have slightly varying outputs.[7] Notwithstanding the differences in analytical technique, sample state, and prediction algorithms, the secondary structure elucidation by FTIR using PROTA-3S software is largely in line with that from X-ray. Transmission-FTIR measurements combined with PROTA-3S software offer a facile and fast means to analyze the secondary structure of proteins in solution[2, 3] with minimal sample prep.

ATR-FTIR with ConcentrateIR Accessory

When the quantity and concentration of protein are limited, FTIR measurements with the ConcentratIR2 ATR accessory offer a better alternative than transmission-FTIR spectroscopy. The unique design of this ATR accessory allows for the direct measurement of protein powders, gels, solutions as well as proteins dried on the ATR surface. When concentrating proteins on the crystal surface, caution should be exercised in buffer selection since buffer will also concentrate on the surface of the crystal.

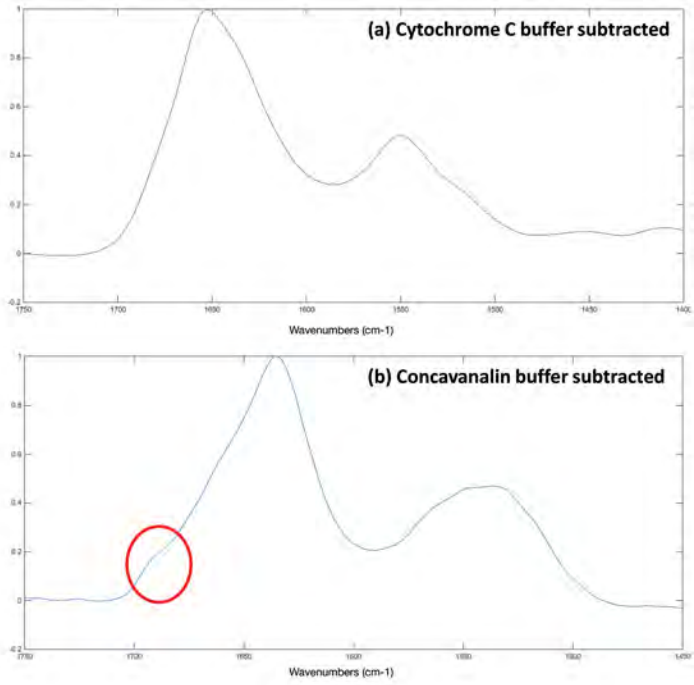

Figure 2: FTIR spectra of (a) cytochrome C and (b) Concanavalin A after the buffer spectrum was subtracted using PROTA-3S software.

	α-Helix (%)		β-Sheet (%)		Random (%)	
Protein	FTIR	X-ray	FTIR	X-ray	FTIR	X-ray
Cytochrome C	45	41	5	0	50	59
Concanavalin A	4	0	42	48	54	52

Table 2: Comparison of secondary structure calculation from FTIR (PROTA-3S) and X-ray data.

Only those buffers with minimum or no peaks in the Amide I and II region should be selected. Figure 3 shows the ATR-FTIR spectra of BSA in phosphate buffer, dried on the crystal from a 1 mg/mL solution. In addition to the Amide I and II bands, there are spectral features of the side chain, such as 1515 cm^{-1} from tyrosine and 1498 cm^{-1} from aspartic acid. Side chain peaks are critical in the elucidation of protonation and de-protonation states of various amino acids.[2]

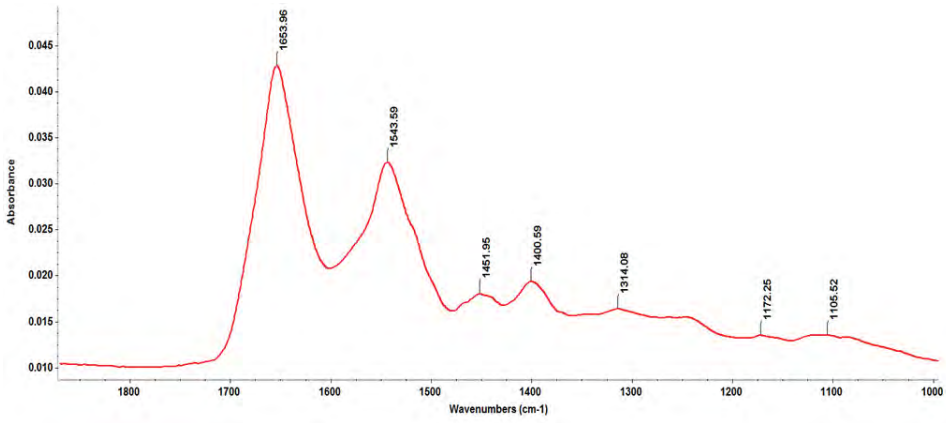

Figure 3: Amide I and II for 1 mg/mL BSA analyzed using ConcentratorIR2 ATR on the Nicolet iS50 FTIR spectrometer equipped with an MCT detector.

Peak deconvolution of the Amide I peak (Figure 4) of BSA was carried out using the OMNIC software. It is important to note that second derivative analysis is often performed prior to deconvolution to clearly identify the peaks required for peak fitting.[2] In the current study, the second derivative peaks obtained (results not shown) well correlate to the secondary structure peak assignments in Table 1. In order to obtain a good peak shape for peak fitting, a baseline correction on the Amide I region was also performed. Baseline correction also effectively excluded the contributions from the Amide II region. The deconvolution of Amide I resulted in 5 peaks, and the area under each peak was then evaluated against the total area. Amide I peak deconvolution shows a secondary structure composition of 47% α-helix, 3% β-sheet, 24% coils, and 26% random, similar to published FTIR[5] and X-ray data.

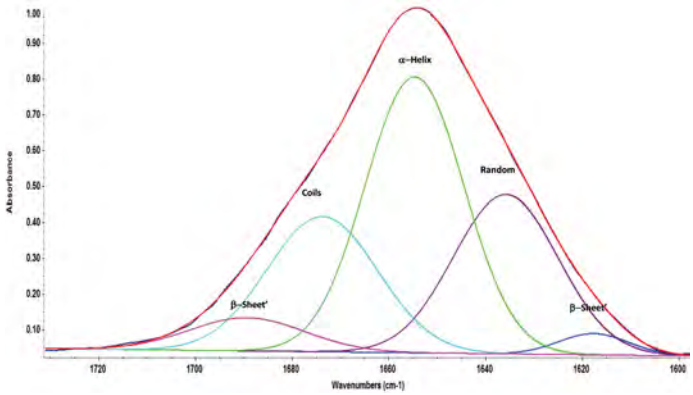

Figure 4: Peak deconvolution of Amide I peak of BSA using Peak Resolve function of OMNIC software.

Conclusion

In this note, we have demonstrated two examples of protein secondary structure elucidation using FTIR spectroscopy. Transmission-FTIR measurements combined with PROTA-3S software provides a facile means to analyze secondary structure of proteins in solution with minimal sample preparation. When the quantity and concentration of protein are limited, ATR-FTIR offers a better alternative by drying the proteins in ATR crystals directly.

References

1. Elliott, A., Ambrose, E. J. *Structure of synthetic polypeptides*, Nature (1950) 165, 921-922.
2. Jackson, M., Mantsch, H.H. *The use and misuse of FTIR spectroscopy in the determination of protein structure*, Crit. Rev. Biochem. Mol. Biol. (1995) 30, 95-120.
3. Barth, A. *Infrared spectroscopy of proteins*, Biochim. Biophys. Acta (2007) 1767, 1073-1101.
4. Byler, D.M., Susi, H. *Examination of the secondary structure of proteins by deconvolved FTIR spectra*, Biopolymers (1986) 25, 469-487.
5. Surewicz, W.K., Mantsch, H.H. *New insight into protein secondary structure from resolution-enhanced infrared spectra*, Biochim. Biophys. Acta (1988) 952, 115-130.
6. Sukumaran, S., Hauser, K., Maier, E., Benz, R., Mantele, W. *Tracking the unfolding and refolding pathways of outer membrane protein porin from Paracoccus denitrificans*, Biochemistry (2006) 45, 3972–3980.
7. Klose, D., Janes R.W. 2Struc – *the protein secondary structure analysis server*, Biophysical Journal (2010) 98, 454-455.

Find out more at **www.thermofisher.com/FTIR**

ThermoFisher SCIENTIFIC

thermo scientific

APPLICATION NOTE AN52307

A case study of using FT-NIR for pharmaceutical hot melt extrusion process monitoring

Author

Herman He[1], Scott Martin[1], Anh Vo[2], Michael Repka[2] and Rui Chen[1]

[1]Thermo Fisher Scientific, USA

[2]School of Pharmacy, University of Mississippi

Keywords

pharmaceutical extrusion, hot melt extrusion (HME), process analytical technology (PAT), FT-NIR Spectroscopy, active pharmaceutical ingredient (API), partial least square (PLS), principle component analysis (PCA)

Application benefits

- Real time in-process monitoring
- Nondestructive and fast
- Provides chemical structural information

Thermo Fisher Scientific solutions

- Antaris FT-NIR Analyzer
- Process 11 Twin Screw Extruder
- Result software
- TQ Analyst software

Introduction

Continuous manufacturing, such as hot melt extrusion (HME), is gaining increasing interest in the pharmaceutical industry due to its high manufacturing efficiency and economic benefits.[1] HME is primarily a mechanical/shear mixing process, but can also include a chemical reaction process in some formulations. During HME an active pharmaceutical ingredient (API) is melted, mixed, and bonded with thermoplastic polymers and/or other binding materials to form a unique polymeric structure. Judiciously designed polymers can promote desired API/polymer bonding structure, improve drug bio-availability, and achieve unique drug delivery profiles.[2, 3, 4] HME process operation parameters, such as screw design and rotational speed, zone temperature, and residence time must be controlled precisely to ensure the consistency and the product quality. In the new era of pharmaceutical process development, quality by design (QbD), one of the key initiatives from the FDA,[5, 6] requires a thorough understanding of all critical process parameters so that an effective process control strategy can be implemented for more uniform product quality and more efficient production operations.

As an invaluable in-process analytical tool, Fourier transform near-infrared (FT-NIR) spectroscopy in conjunction with statistical regression techniques has been used to provide near real-time chemical information. FT-NIR spectroscopy has been widely used as a process analytical technology (PAT) and QbD tool for process development and manufacturing in pharmaceutical industry to monitor and/or control such processes as drying, blending, and extrusion.[7, 8] It is a simple, fast, and nondestructive technique that provides multi-constituent analysis of virtually any matrix without the need for sample preparation and manipulation. More importantly, NIR provides molecular level chemical information through a direct measurement of the material being processed. It is sensitive to the API concentration in a blend, and the interactions between the API and its binding polymers.

In this application note, we demonstrate the use of FT-NIR for in-line API concentration monitoring during an HME process. The considerations in deriving an appropriate partial least square (PLS) model are discussed. In addition, the feasibility of employing NIR spectral responses as an indicator for HME process stability is also explored.

ThermoFisher SCIENTIFIC

Experimental

An 11-mm twin-screw extruder, Thermo Scientific™ Process 11 (Thermo Fisher Scientific, Karlsruhe, Germany) was used for the HME processes. Figure 1 is a schematic showing the screw profile design as well as process configuration, and the effective length-to-diameter ratio (L/D) for the system was defined as 40:1. Three mixing zones were configured for the process.

Pre-blended ketoprofen (API) and Eudragit® L100-55 (polymer), with their chemical structures shown in Figure 2, were fed into the extruder at Zone 1 position. Zones 2 through 8 were mixing, conveying and discharge zones. Zone 9 is a die that reduces the barrel configuration to a single circular orifice.

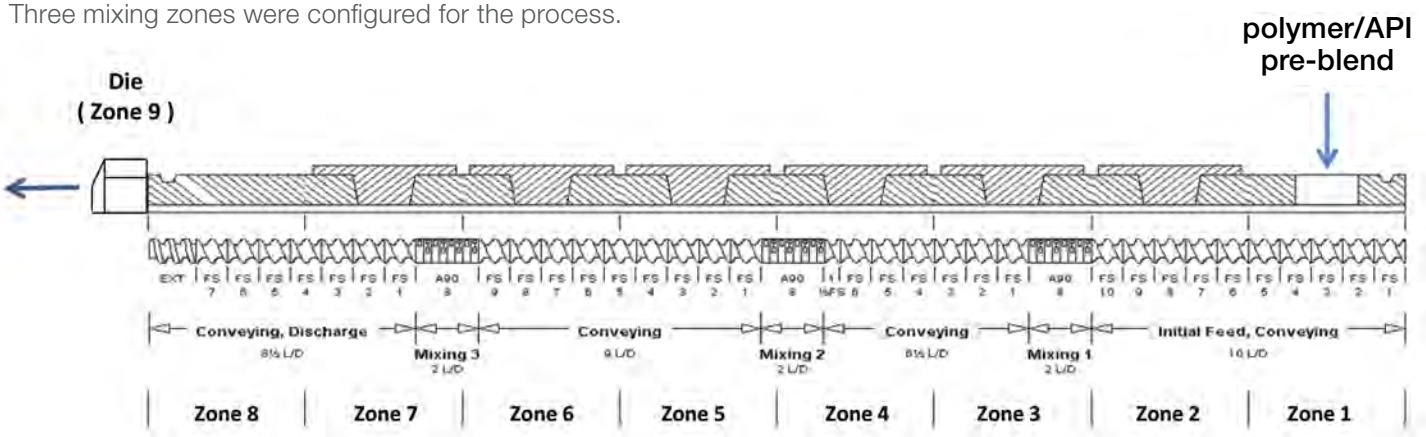

Figure 1: Schematic of a Thermo Scientific Process 11 Twin Screw Extruder configured in this study.

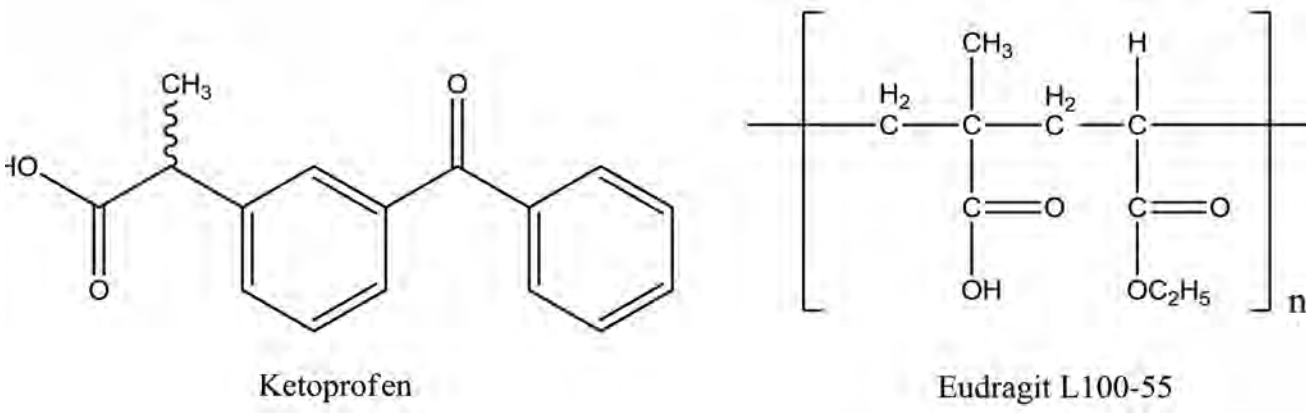

Figure 2: Chemical structures of ketoprofen and Eudragit® L100-55.

A Thermo Scientific™ Antaris™ II MDS FT-NIR spectrometer (Thermo Fisher Scientific, Madison, Wisconsin), equipped with a HME diffuse reflectance probe, was used for spectral acquisition. The reflectance probe has standard 1/2-20 UNF mounting threads and was screwed into one of the sensor ports of the exit block, between the exhaust gas vent and the exit orifice. Since the hot melt is a translucent liquid at the sampling location, a metal reflector was placed on the opposite side of the probe to enhance the NIR signal. The gap between the reflector and the probe surface was ~2 mm. The exit block was heated at 120 °C by an electric heater controlled by the extruder PLC.

The target blending ratio of ketoprofen and Eudragit L100-55 was 50:50 (w/w). The temperature in the mixing and melting zones was set at 120 °C. The material feed rate was 100 g/h. NIR data acquisition was performed using the Thermo Scientific™ RESULT™ v3 software package. The spectral range was 4000–10,000 cm^{-1} and the resolution was 8 cm^{-1}. The number of spectral scans averaged was 16, or 8 seconds per spectrum. A background reference spectrum was acquired using the transmission sampling module at the beginning of each set of experiments.

Results and discussion

Building a PLS model to monitor API concentration for HME

Figure 3A shows the overlaid NIR spectra of ketoprofen, Eudragit, and a 50:50 (w/w) extrudate. Both ketoprofen and Eudragit are powders at room temperature, and their absorption spectra were measured using an integration sphere module of the Antaris II spectrometer. The spectrum of the extrudate was acquired with an NIR HME probe during an extrusion process. All spectra have strong features in the first overtone C-H stretching region (~6000 cm^{-1}). In addition, both Eudragit and the extrudate have noticeable peak features in the first overtone O-H stretching region (~6900 cm^{-1}).

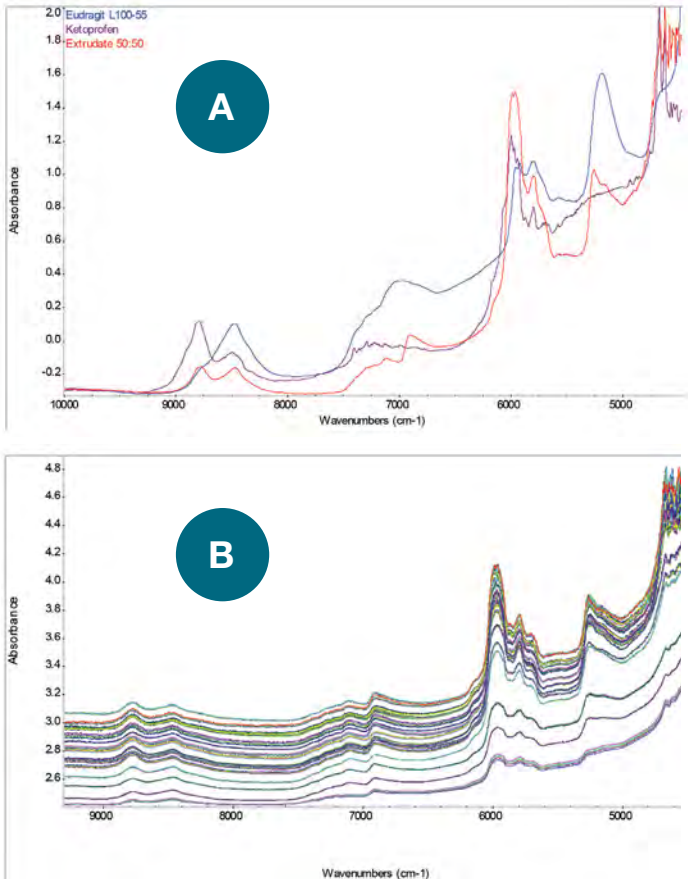

Figure 3. (A) Absorption NIR spectra of ketoprofen, Eudragit L100-55, and a 50/50 (w/w) ketoprofen/Eudragit extrudate in full scale. (B) Transflectance NIR spectra in common scale acquired during extrusion processes.

NIR spectra are often complex and contain broad overlapping absorption bands. Chemical, physical, and structural properties of all species present in a sample influence the measured spectra. As a result, the measured NIR spectra depend on more than one variable simultaneously; hence, multivariate. Chemometrics uses mathematical and statistical procedures, such as PLS and principle component analysis (PCA), for multivariate data analysis to filter information that correlates to a certain property from a large set of data.

To build a calibration model to predict the API concentration during HME, the pre-blend API/polymer ratio was varied from 40 to 60%, bracketing the target API concentration of 50% (w/w). The normal process temperature was set at 120 °C, but +/- 10 °C disturbances were introduced to simulate possible temperature variation in manufacturing process. The feed rate of 100 g/h remained constant throughout the experiment. After each API concentration change was introduced, adequate time was allowed to ensure a steady state was reached before the next process change. The spectral data collected during steady states, including those at different temperatures, were used as calibration samples. NIR spectra were collected at a 20-second interval. The calibration sample set has a total of 85 spectra at 7 concentration levels: 40%, 45%, 47.5%, 50%, 52.5%, 55%, and 60%.

Figure 3B shows the overlaid NIR spectra of the calibration samples. There is a noticeable baseline up-drift in all spectra. While it is difficult to ascertain the exact causes for this up-drift, one likely contributing factor is the scattering by the air bubbles formed during the HME process and the variation in effective pathlength. Because of the relatively low material feed rate (100 g/h); hence, high air/material ratio, the vent nozzle was not able to completely remove air and moisture from the hot melt, resulting in micro-size air and water vapor bubbles.

The Norris second derivative[10] was first applied to the raw spectra to remove the baseline drift, followed by a standard normal variant (SNV) to minimize the spectral pathlength variation. A PLS model[11] to estimate the ketoprofen concentration was then derived using the Thermo Scientific™ TQ Analyst™ software. All spectral data were mean-centered in the PLS regression, and the spectral range of 5500 to 6650 cm-1 was used for the correlation. A total of 85 spectra were divided into two groups: calibration (73 spectra) and validation (12 spectra). PLS finds its significant model factors from the Leave-One-Out cross validation. The number of significant PLS factors represents the number of independent variables that affect sample spectral responses, such as concentration, impurities, density, opaqueness, or sample color. In the current case, the developed PLS model (Figure 4) has a correlation coefficient of 0.998 and a root mean squared error of calibration (RMSEC) of 0.43%. The root mean squared error of prediction (RMSEP) from the validation sample group is 0.62%.

The calibration model was then applied to the spectra collected during the HME process, and the results are shown in Figure 5. As can be seen, the predicted API% tracks the pre-blend API profile. With a feed rate of 100 g/h, the process has a residence time of ~10 min, but it takes 2-3 multiples of the residence time (approximately 20-30 min) to establish a new steady state after the pre-blend ratio is introduced.

Extracting the relevant portion of the multivariate NIR spectral data is critical for a successful chemometrics model. For example, process temperature has a profound impact on measured NIR spectra because temperature can affect samples both physically (e.g. sample density) and chemically (e.g. the degree of hydrogen bonding). Figure 6A shows the 2nd derivative NIR spectra of hot melt samples collected at three process temperatures. There are prominent spectral changes around 6900 cm^{-1}, likely due to the increased H-O bonding at elevated temperatures. However, this spectral region was purposely excluded in the current PLS model so that the model can keenly reflect the API concentration change without the interference from temperature induced spectral variation. The spectral range of 5500 to 6650 cm^{-1} was used instead for the correlation. Figure 6B shows the API% change with temperature ramping from 110 to 130 °C, while maintaining a pre-blend API ratio of 50% (w/w) and feed rate of 100 g/h, simulating potential temperature variations in a real HME process. The predicted API% hovers around 49-51% throughout the experiment. The results suggest that the developed PLS model for API% prediction is robust with a +/- 10 °C temperature variation.

Process stability monitoring with PCA

Continuous manufacturing requires the production process to be controlled in its steady state to ensure smooth production and stable product quality. In an HME process, the controllable process variables include the speed of material flow, extrusion temperature distribution profile, and screw speed, etc. Traditionally, an HME process is considered at its steady state when operational parameters such as torque, material temperature, and pressure reach their equilibria. NIR, on the other hand, not only provides chemical information of the samples, including blending ratio and interactions between the API and the binding material, but also is sensitive to many physical properties of the sample, such as color, temperature, and density. NIR spectra are therefore a more incisive, responsive, and comprehensive process indicator for product quality control.

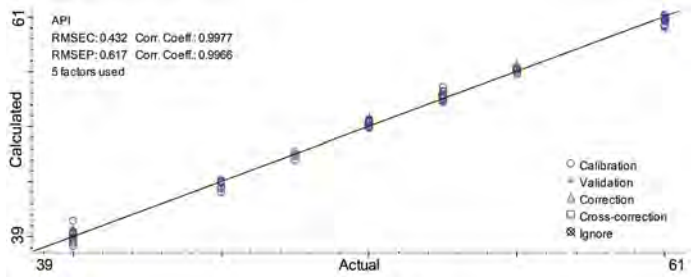

Figure 4. Calibration results of API measurement.

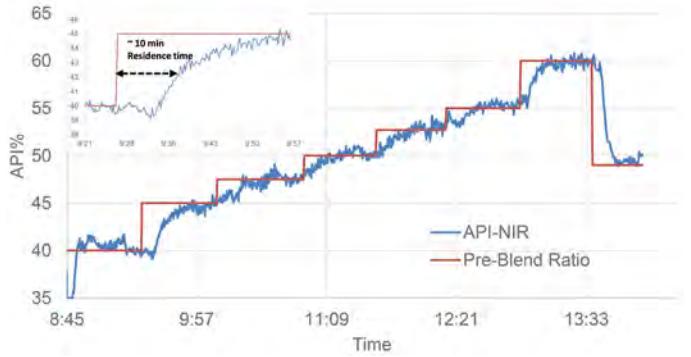

Figure 5. Overlay of the pre-blend profile and the API% trend based on the PLS model.

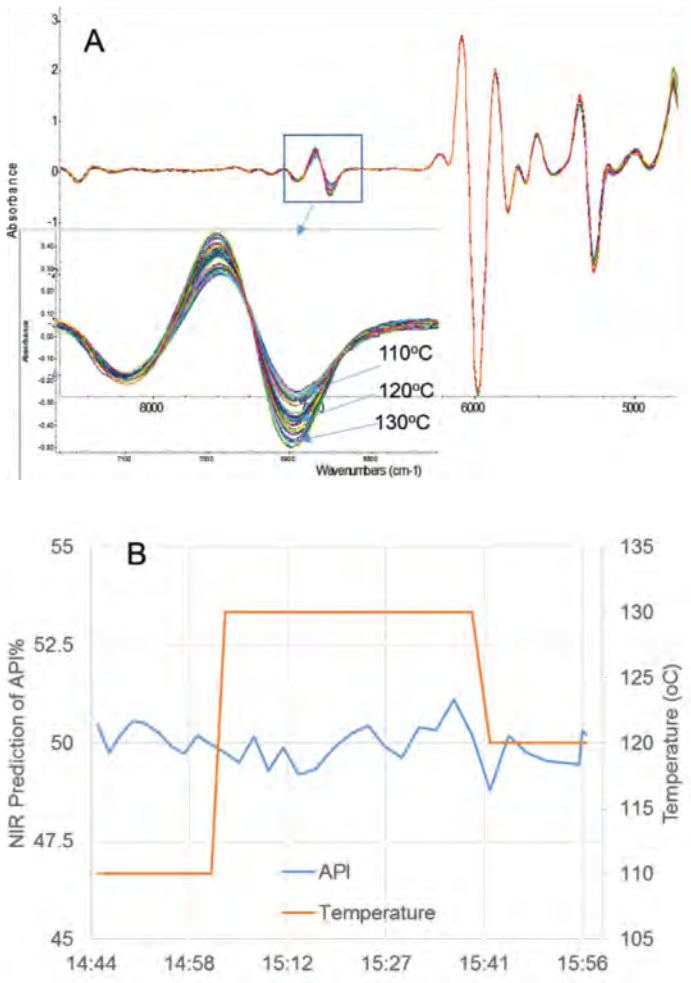

Figure 6. Process temperature robustness study: (A) temperature impact on NIR spectra; and (B) prediction of API% with a +/- 10 °C temperature variation.

To simulate potential process fluctuations during a manufacturing process, two process variables, feed rate and temperature, were introduced as process disturbances. Sample spectra were acquired at a 20-second interval. The raw spectral data was processed with the 2nd derivative and SNV to remove spectral baseline drift and variations in spectral path length, then analyzed using PCA.[9] The spectral wavelength region used for the PCA calculation was from 9150 to 4710 cm^{-1}.

PCA defines its principal component (PC) domain space through an iteration of information extraction from a calibration sample set, and converts each sample spectrum consisting of thousands of data points into a reduced, e.g. 2-3 dimensional, data point in a PC domain. The number of dimensions in a PC domain is related to the number of process variables that affect sample spectra, such as concentration, degree of cross-link, sample color, and density. Generally, the first several principal components cover the majority of the spectral information. Scores, or coefficients, of principal components are projections of a measured sample spectrum in a PC domain. By converting a sample spectrum into a PC point, sample spectral responses during an HME process can be visually displayed in a 2- or 3-dimensional trend plot. Because NIR spectra are a direct measurement of the extrudate product, the trajectory of their PC coordinates movement in a PC domain should be a better representation of a HME process state. The trajectory from one cluster to another offers insight into the process dynamics so that a more comprehensive control strategy can be developed to make the HME process more stable.

Figure 7A is a PC score plot of the temperature experiment. The feed rate was maintained at 100 g/h. The process temperature started at 120 °C. The sample spectra form a tight cluster of PC points (middle) in the PC domain. Once the process was stabilized, a 10 °C temperature decrease was introduced in the temperature controller. The spectral response from the hot melts changed accordingly. As a result, the resulting PC data point moves away from the previous cluster. It took about 6 sampling times, or about 2 minutes for the sample PC point to move from the 120 °C cluster to a new location and start to form a new cluster. The distance between the two clusters represents some property shift in the hot melt. Similar PC point movement was observed for the temperature change from 110 to 130 °C.

Figure 7B is a PC score plot of the feed rate response experiment. The temperature was maintained at 120 °C. The process started with a 100 g/h material feed rate. Once it was stabilized, the feed rate was increased to 120 g/h. Similar to the temperature experiment, it takes about 2 minutes for the PC data points to shift to a new location in response to the feed rate change.

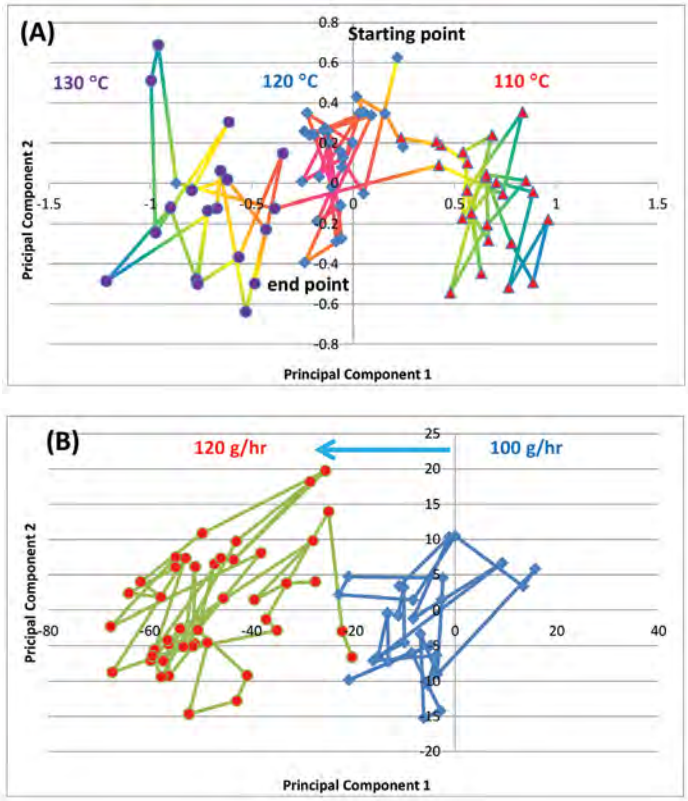

Figure 7. PC score plot of (A) temperature response; and (B) feed rate response.
**Note: The API concentrations for the temperature and feed rate experiments are different; hence, the PC1 / PC2 ranges are different in the plots.*

Conclusions

Continuous manufacturing requires in-process monitoring of critical process parameters to ensure product consistency. In this note, FT-NIR in conjunction with chemometrics modelling for in-line HME process monitoring is demonstrated. In the first case, a PLS model was successfully developed for API concentration prediction by carefully selecting the relevant NIR spectral region. The developed model is also proven robust with a +/- 10 °C temperature fluctuation. The second case is concerned with the use of a PCA based model to monitor the process state shift in response to disturbances such as temperature and material feed rate. Because the NIR spectrum is a direct measurement of the extrudate product, the trajectory of the PC movement offers insight to the process dynamics. Moreover, since the PCA method relies solely on an accumulation of multiple batches of good process spectral data to define the steady state, it does not require a calibration model. It is independent of the product formulation and is easy to implement. Finally, because NIR is nondestructive and fast, an NIR-based quality monitoring methodology can be easily transferred from process development to manufacturing.

References

1. Schaber S.D., Gerogiorgis D.I., Ramachandran R., Evans J.M.B., Barton P.I. and Trout B.L. *Economic analysis of integrated continuous and batch pharmaceutical manufacturing: a case study*, Ind. Eng, Chem. Res., 2011, 50:17, 10083-10092. doi: 10.1021/ie2006752.

2. Thiry J., Krier F., Evrard B. *A review of pharmaceutical extrusion: Critical process parameters and scaling-up*, Int. J. Pharmaceut., 2015, 479:1, 227-240.

3. Breitenbach J. *Melt extrusion: from process to drug delivery technology*, Eur. J. Pharm. Biopharm., 2002, 54:2, 107-117.

4. Crowley M.M., Zhang F., Repka M.A., Thumma S., Upadhye S.B., Battu S.K., McGinity J.W., and Martin C. *Pharmaceutical applications of hot-melt extrusion: Part I*, Drug Dev. Ind. Pharm., 2007, 33:9, 909-926.

5. FDA Guidance for Industry. *PAT – a framework for innovative pharmaceutical development, manufacturing, and quality assurance*. Rockville, MD: Food and Drug Administration, 2004.

6. ICH Q8(R2), *Pharmaceutical Development, Part I: Pharmaceutical development, and Part II: Annex to pharmaceutical development*, 2009.

7. Markl D., Wahl P.R., Menezes J.C., Koller D.M., Kavsek B., Francois K., Roblegg E., and Khinast J.G. *Supervisory control system for monitoring a pharmaceutical hot melt extrusion process*, AAPS PharmSciTech, 2013, 14:3, 1034-44.

8. MacPhail N., Meyer R.F, Phillips, J.X., Gendron C.M., Smith-Goettler B. *NIR Monitoring of a hot-melt extrusion process*, Spectroscopy Special Issues, 2011, 26:8.

9. Abdi H. and Williams L.J., *Principal component analysis*, Wires. Comput. Stat., 2010, 2, 433-459.

10. Rinnan A., van den Berg F., Engelsen S.B. *Review of the most common pre-processing techniques for near-infrared spectra*, Trends Anal. Chem., 2009, 28:10, 1201-1222.

11. Geladi P. and Kowalski B.R., *Partial least-squares regression: a tutorial*, Anal. Chim. Acta, 1986, 185, 1-17.

Find out more at **www.thermofisher.com/extrusion**

ThermoFisher SCIENTIFIC

thermo scientific

APPLICATION NOTE AN52327

Measuring the equilibrium constant of a keto-enol tautomerism using benchtop NMR

Author

Dean Antic, Thermo Fisher Scientific, Boulder, CO, USA

Keywords

pharmaceutical, synthesis, kinetics, tautomerism, equilibrium

Application benefits

The ethyl acetoacetate ^{1}H NMR spectrum demonstrates the utility of benchtop NMR in measuring an intramolecular equilibrium. NMR is ideal for studying reaction kinetics, as it is a nondestructive technique. An advantage of the Thermo Scientific™ picoSpin™ NMR spectrometer in monitoring reaction kinetics is that small quantities of reaction mixtures can be directly injected into the capillary micro probe without the need for dilution in a deuterated solvent.

Abstract

The ^{1}H NMR spectrum of a β-ketoester, ethyl acetoacetate, reveals the presence of tautomerism, a dynamic process of intramolecular hydrogen bonding. Proton exchange between the tautomeric species is slow, allowing for direct measurement of each of the enol and keto forms of ethyl acetoacetate. The signal areas for each species were then integrated. From which, the percent composition of each constitutional isomer was calculated and the equilibrium constant was derived. In addition to qualitative structure elucidation, ^{1}H NMR also provides quantitative information to evaluate solution dynamics.

Introduction

Ethyl acetoacetate (EAA), a β-ketoester, is a colorless liquid with a sweet, fruity aroma and flavor. Its primary application is as a starting material in the synthesis of α-substituted acetoacetic esters and cyclic compounds, as an intermediate in the synthesis of vitamins and pharmaceuticals, and in the manufacture of inks, plastics, dyes and lacquers. Ethyl acetoacetate undergoes self-enolization (Figure 1), where the keto form **1** exists in equilibrium with its enol isomer **2a** and **2b**. The process occurs because the α-hydrogen, adjacent to the carbonyl, is slightly acidic, with p*K*a values ranging from 9-13 in β-dicarbonyls, making ketones readily enolizable.[1] This intramolecular chemical equilibrium between keto and enol isomers is referred to as tautomerism. The chemical equilibrium is thermodynamically driven. Typically, the more stable keto form is favored at room temperature and above. However, in β-diketones, stabilization of the enol form arises from stabilization by π-system conjugation. Terminal groups and α-substituents also play a role in enol formation, where bulky R groups in the α position results in steric effects destabilizing the enol, while electron withdrawing groups in the α position help to stabilize it.

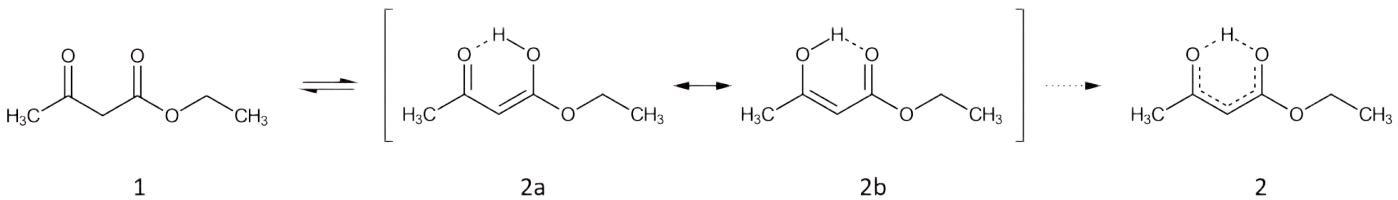

Figure 1: Keto-enol tautomerism of ethyl acetoacetate.

ThermoFisher SCIENTIFIC

Tautomers can be readily studied by proton NMR because the high energy barrier for the interconversion between enol-keto tautomers (Figure 1) makes it a slow process that's amenable to NMR analysis. Hence, keto and enol protons experience different local environments, resulting in easily identifiable proton chemical shifts.[2] For EAA, this is evident in the proton spectrum, where resonances due to the keto form dominate.[1-4] By integrating these signals the equilibrium constant, K_{eq}, and the %enol can be calculated for a given compound at a specific sample temperature.

Experimental

The ^{1}H NMR spectrum of EAA was measured from a neat sample at 82 MHz and 32 °C using the Thermo Scientific™ picoSpin™ 80 spectrometer. The spectrometer's capillary cartridge was fitted with micro-fluidic inlet and outlet connectors that allow liquid sample injection into the spectrometer's RF coil. The fluid path was Teflon/Quartz capillary tubing with a total flow-path volume of 40 microliters (µL). Liquid samples were introduced by manual injection using a disposable 1 mL syringe and a 22-gauge blunt tip needle.

Spectra were acquired using the following acquisition parameters: a 90° RF excitation pulse, a 1000 ms acquisition time, and a 12 second recycle delay. All spectra were acquired with signal averaging. Spectral data were stored in a JCAMP-DX file format and imported into MestrelLab Research's Mnova™ NMR analysis program for processing. Standardized data processing was applied across all spectra, specifically, by applying zero filling, applying phase correction, and filtering using exponential apodization. Resonance signals were fitted using generalized Lorentzian functions, and integrated using Mnova's Global Spectrum Deconvolution method.

Results and discussion

Figure 2 shows the ^{1}H NMR spectrum of ethyl acetoacetate. Based on chemical shifts, multiplicity and relative signal intensities, assignment of signals are straightforward and unambiguous. The enol and keto forms are indicated by 'e' and 'k', respectively, in Figure 2. The signals were internally referenced relative to the large singlet proton resonance at 2.21 ppm originating from the acetyl methyl (C_{18}) protons of the keto isomer.

The chemical shift of ethyl ester protons (-OCH_2CH_3) are unaffected by tautomerization and appear as classic spin-coupled signals. Centered at 1.23 ppm, the terminal methyl protons on C_{14} (e, C_8; $^3J_{HH}$ = 7.12 Hz) generates a triplet due to spin-spin coupling to the adjacent methylene protons on C_{13} (e, C_7). The methylene (CH_2) resonance due to the protons on C_{13} appears as a spin-coupled quartet centered at 4.14 ppm ($^3J_{HH}$ = 7.12 Hz). The enol tautomers **2a** and **2b** do not produce unique resonances separately because their conversion is a rapid exchange process. At the opposite terminus, the acetyl methyl protons are affected by tautomerization due to changes in electron density at the carbonyl carbon (e, C_4), resulting in an upfield shift of the enol signal (C_9) relative to those of the keto signal (C_{18}). The former appears as a weak singlet at 1.94 ppm, while the latter is at 2.21 ppm. The α-protons of the keto and enol (C_3) forms manifest as singlets at 3.48 ppm (C_{15}) and 5.03 ppm (C_3), respectively. The enol hydroxylic proton (C_{5a}) appears as an unsaturated alcohol, but intramolecular hydrogen bonding causes it to behave like a carboxylic acid, shifting its resonance far downfield to 12.14 ppm.

The enol-keto equilibrium constant, K_{eq} = [enol]/[keto], and %enol are functions of temperature. Their values can be determined by integrating the enol and keto signal areas. Table 1 summarizes the equilibrium constant and percent enol concentration values calculated for the different combinations of enol to keto ratio. Note that each peak integration area is weighted according to the number of protons that contribute to the respective signal. For example, the enol methyl contains three protons while the keto methylene has only two protons; the weighting factor, in this case, is 2/3.

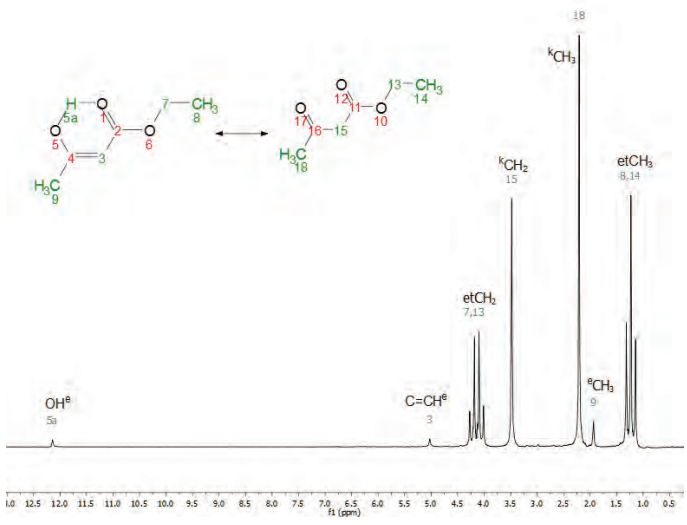

Figure 2: Full ^{1}H NMR spectrum of ethyl acetoacetate. Enol and keto forms are indicated by 'e' and 'k', respectively. The prefix "et" refers to ethyl. Inset shows the numbering system used to assign signals in the NMR spectrum of ethyl acetoacetate.

Signal	K_{eq}	%enol	Signal	K_{eq}	%enol	K_{eq}	%enol
$^{e}CH_3$			^{e}CH			0.09[a]	8.0%[a,b]
$^{k}CH_2$	0.094	9.4%	$^{k}CH_2$	0.103	10.3%		
$^{k}CH_3$	0.096	9.6%	$^{k}CH_3$	0.105	10.5%		

[a] Ref. 4. [b] Ref. 2.

Table 1. Equilibrium constant and percent tautomer composition measured at 32 °C.

From Figure 2, the calculated average K_{eq} is 0.0992 ±0.005 and %enol is 9.9%. Our values compare favorably to those reported by others,[1,4] where the calculated values for K_{eq} and %enol are 0.09 and 8.0%, respectively, at 32 °C. These results confirm that the keto tautomer is the more favorable structure, and that the ethyl ester group doesn't introduce additional steric interaction to destabilize the keto form.

Conclusions

The ^{1}H NMR spectrum of a β-ketoester, ethyl acetoacetate, reveals the presence of tautomerism, a dynamic process of intramolecular hydrogen bonding. Proton exchange between the tautomeric species is slow, allowing for direct measurement of each of the enol and keto forms of ethyl acetoacetate. Integrating signal areas for each species affords relative concentration information to calculate the equilibrium constant and percent composition of each constitutional isomer. In addition to qualitative structure elucidation, ^{1}H NMR also provides quantitative information used to evaluate solution dynamics.

References

1. Allen, G.; Dwek, R. A. *J. Chem. Soc. B,* **1966**, 161-163.
2. Cook, G.; Feltman, P. M. *J. Chem. Educ.* **2007**, *84*, 1827-1829.
3. Drexler, E. J.; Field, K. W. *J. Chem. Educ*. **1976**, *53*, 392-393.
4. Burdett, J. L.; Rogers, M. T. *J. Am. Chem. Soc.* **1964**, *86*, 2105-2109.

Thermo Scientific picoSpin 80 NMR spectrometer

Find out more at **www.thermofisher.com/nmr**

ThermoFisher SCIENTIFIC

APPLICATION NOTE

No. AN52889

Benchtop NMR Combined with GC/MS Confirms Identity of Forensic Case Sample

Authors: Dean Antic, Ph.D.,
Thermo Fisher Scientific,
San Jose, CA, USA

WanLi Wei, Senior Engineer,
Institute of Forensic Sciences, Wuxi Public Security Bureau, Wuxi, China

Key words
NMR, GC/MS, picoSpin, illicit drug, forensics

The benchtop Thermo Scientific™ picoSpin™ 80 ^{1}H NMR spectrometer provides an additional layer of structural identification of drug analogues and precursors, complementing GC/MS analysis. The combination of the two techniques allows for a positive identification of real forensic case samples with high confidence, thereby enhancing the presumptive testing capabilities of illicit drug screening facilities.

Abstract

A forensic case sample of an illicit drug precursor was analyzed by GC/MS and benchtop NMR. The most probable chemical structure from a GC/MS library search, however, conflicts with the spectral features identified by NMR. By interrogating the peak pattern and chemical shifts in the NMR spectra, both experimentally obtained and predicted by Mnova NMR software, the seized sample was identified as a compound with a lower matching score by GC/MS. The combination of the two techniques allows one to discriminate between two possible structural isomers in a real forensic case sample with high confidence.

The case sample demonstrated in this note exemplifies the need for multiple techniques in order to confirm the identity of seized forensic samples, as recommend by SWGDRUG.

Introduction

Illicit drugs identification is a challenge to law enforcement due to the vast assortment of illegal drugs that already exist, and an increasing number of new, “not-yet” illegal analogues of classified drugs appearing on the street. Added to this burden is the identification of clandestine lab chemicals and precursor compounds used in the manufacture of illicit drugs, as well as the excipients used as adulterants to alter street-level drug purity.

Law enforcement has a variety of analytical tools at their disposal, including color tests, Fourier transform infrared (FTIR), gas chromatography/mass spectrometry (GC/MS), Raman spectroscopy and nuclear magnetic resonance spectroscopy (NMR) to aid in characterizing forensic samples and elucidating their structures.

ThermoFisher SCIENTIFIC

Since no single technique can provide definitive structure elucidation, the Scientific Working Group for the Analysis of Seized Drugs[1] (SWGDRUG) proposes a combination of analytical techniques be used depending on the nature of the samples and available techniques for analysis. Initial chemical identification of a seized sample includes a color test and FTIR analysis. Molecular weight information is provided by mass spectrometry. When combined with other spectroscopic techniques, including Raman spectroscopy and NMR, a chemical structure can be elucidated. The power of GC/MS, FTIR and Raman is highly dependent upon the databases of reference samples and related compounds. It is, therefore, an arduous endeavor to maintain and update these databases in the face of increasing numbers of novel structural analogues that are appearing.

Seized sample identification methods

Figure 1 shows the GC/MS chromatogram of a sample seized from a clandestine lab. The unknown sample was a clear, highly volatile, and fragrant organic liquid, suspected as a precursor compound used in the production of illicit drugs. The data was acquired using a Thermo Scientific™ ISQ™ QD Single Quadrupole GC-MS system. The main component of the sample has a retention time of 4.38 min (top trace) and the corresponding mass spectrum is shown at the bottom of Figure 1. The main component has a molecular mass of 202 g/mol. In addition, there are a series of fragmentation peaks at m/z 159, 129, 103, 73, and 57. The subsequent library search yielded a high probability match of the sample to 1,1-dibutoxy butane, with its structure shown in Figure 2A.

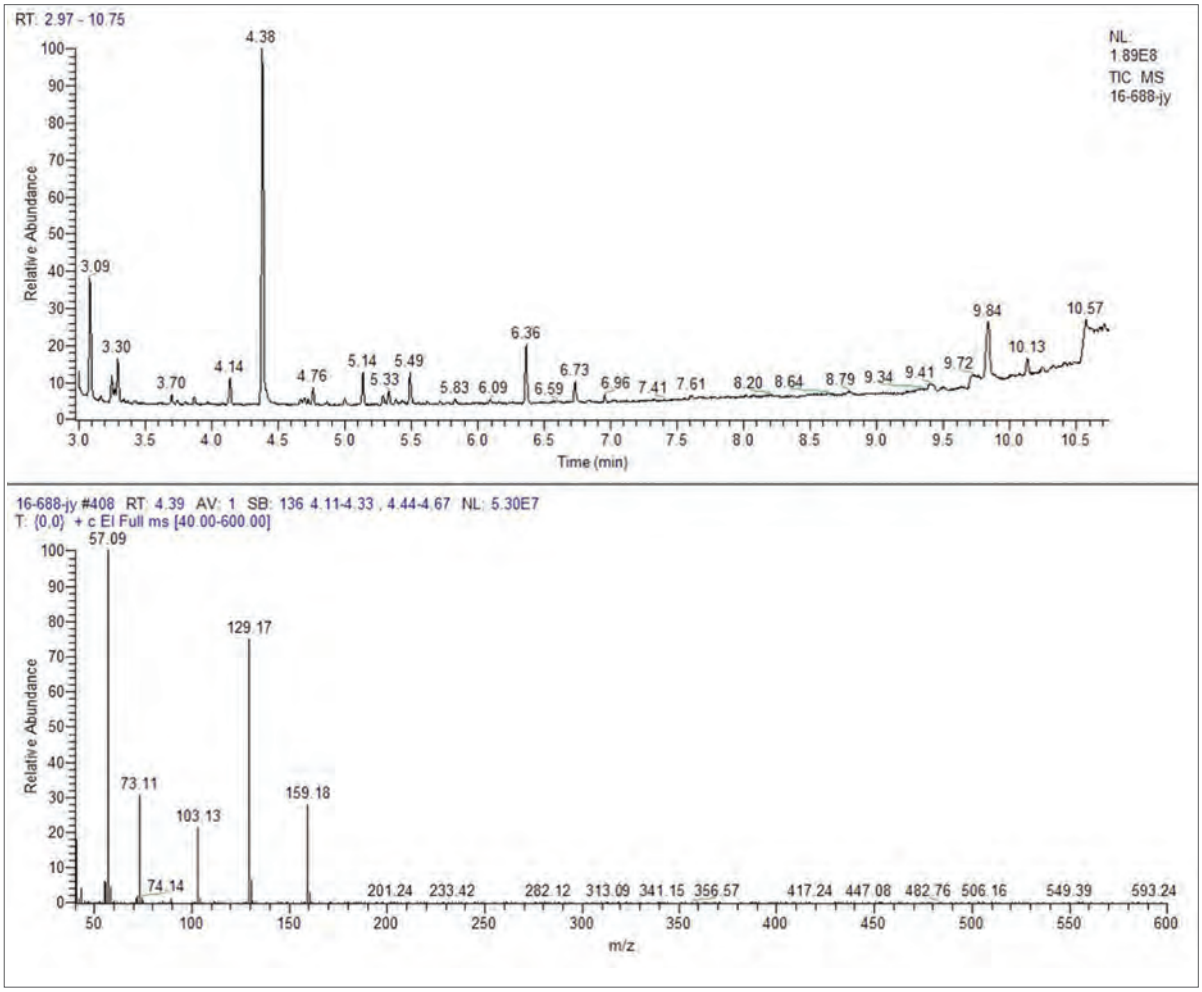

Figure 1
ISQ QD GC-MS chromatogram of unknown liquid (forensic case sample).

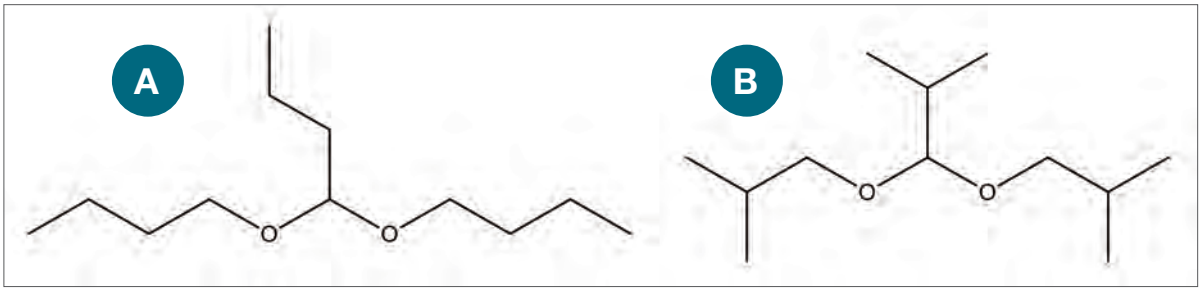

Figure 2
Chemical structures of two isomers; **(A)** 1,1-Dibutoxybutane; and **(B)** 1,1-Diisobutoxy-2-methylpropane.

The sample was further analyzed by a picoSpin 80 ^{1}H NMR spectrometer, an 82 MHz pulsed, Fourier transform ^{1}H NMR permanent magnet instrument, equipped with a capillary cartridge probe. Since the sample was a clear organic liquid, dilution in typical NMR solvents was not required. A small amount of the case sample was placed in a vial, to which a few drops of tetramethylsilane (TMS) was added to reference chemical shifts. The mixture was then directly injected into the NMR spectrometer. The resulting spectrum is shown in Figure 3. Note that the peaks attributed to impurities and TMS are manually labeled gray, whereas the unknown compound peaks are labeled blue.

The spectrum exhibits a distinct pattern of multiplicities characteristic to the isopropyl group: two strong overlapping doublets centered near 0.95 ppm, followed by a more complex series of weaker multiplets between 1 – 2 ppm. In addition, two strong doublets emerge centered at 3.34 and 4.49 ppm, respectively. The pattern of doublets suggests the presence of a single neighboring proton (CH), and the shift to high frequency indicates that the carbon center is attached to an electron withdrawing group. The NMR spectrum also implies structural symmetry of the sample. These suggested structural features, however, conflict with 1,1-dibutoxybutane suggested by the GC/MS library search.

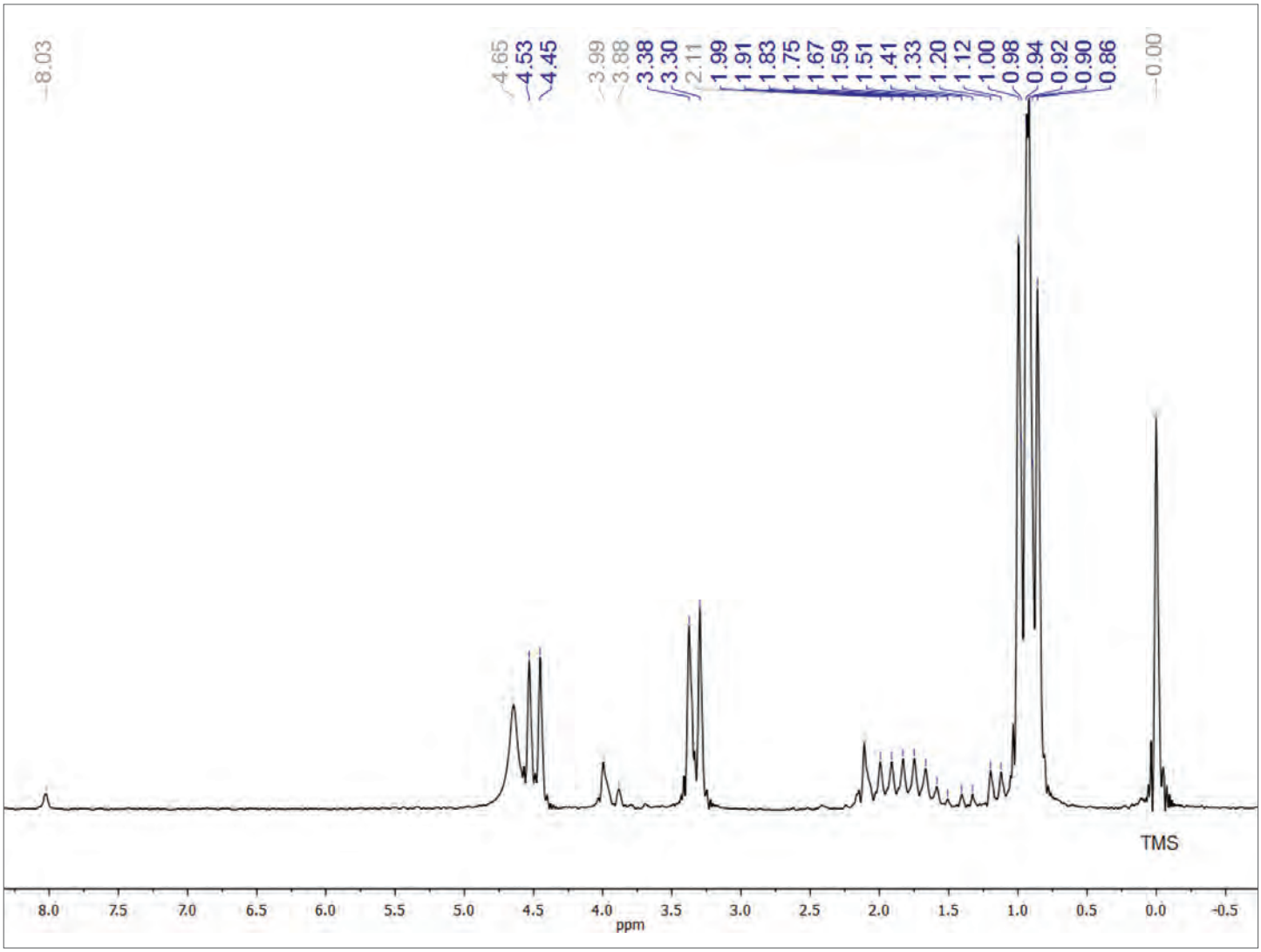

Figure 3

Experimental ^{1}H NMR 82 MHz spectrum of the seized sample. Data was acquired using a 90° pulse and 15 s recycle delay between pulses. The spectrum is an average of 5 co-added scans and processed using the Mnova NMR software suite (Mestrelab Research Inc.).

Figure 4 shows the comparison between the predicted NMR spectrum of 1,1-dibutoxybutane by Mnova software (top) and the experimental ^{1}H NMR spectrum of the seized sample (bottom). There are vast differences between the two spectra, indicating the sample under analysis is not 1,1-dibutoxybutane.

Upon further examination of the compound list from the GC/MS library search, a low probability match compound, 1,1-diisobutoxy-2-methylpropane (Figure 2B), was identified as a strong candidate. The structure possesses all key elements suggested by the experimental NMR spectrum: isopropyl groups, electron withdrawing O atoms, and high symmetry. Figure 5 shows a good agreement between the predicted NMR spectrum of 1,1-diisobutoxy-2-methylpropane (top) and the experimental NMR spectrum of the seized sample (bottom).

The key features of the NMR spectrum are assigned as follows:

- An intense, overlapping set of doublets at 0.9 ppm is due to the terminal methyl's of the isopropyl group (-CH(CH_3)$_2$);
- A broad, weak multiplet between 1 - 2 ppm is due to the methine (CH) coupling to the adjacent CH_3;
- The doublet centered at 3.3 ppm originates from the methylene groups (CH_2) of the 2-methyl propyl moiety. The doublet arises from the coupling to the adjacent CH proton of the isopropyl fragment;
- The doublet at 4.5 ppm belongs to the CH group. It shifts further due to their attachment to two electron withdrawing O atoms. The weaker signal compared to the doublet at 3.3 ppm is due to the presence of only one CH group.

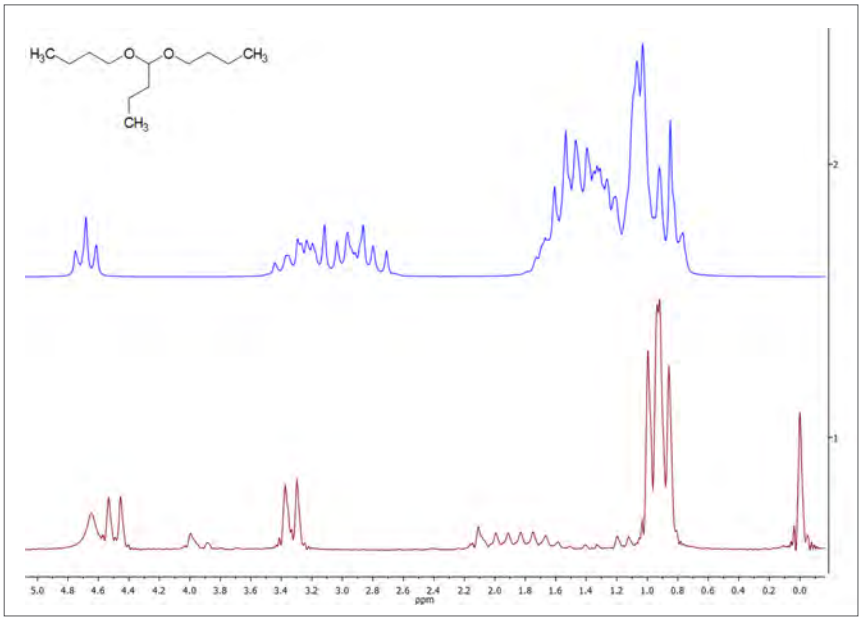

Figure 4
Predicted NMR spectrum of 1,1-dibutoxybutane (top) and experimental ^{1}H NMR 82 MHz spectrum of the seized sample (bottom). The predicted spectrum was generated by using Mnova NMRPredict plugin. Field strength was set at 82 MHz and linewidth value was set at 2.5 Hz.

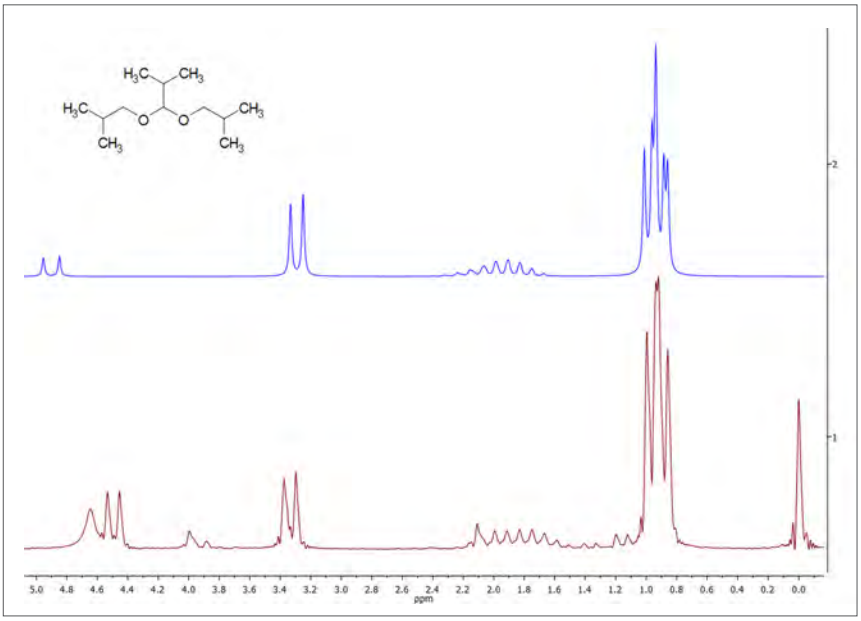

Figure 5
Experimental ^{1}H NMR 82 MHz spectrum of the seized sample and the predicted NMR spectrum of 1,1-diisobutoxy-2-methylpropane generated by Mnova software.

thermo scientific

The GC/MS data in combination with the picoSpin 80 NMR spectrum allows for the positive identification of the seized sample as 1,1-diisobutoxy-2-methylpropane. The compound is a precursor chemical and not a variant structural analogue of known illegal drugs.

Conclusions

In this note we showed how the picoSpin 80 NMR was able to provide additional information by interpreting and predicting the likely structure of a seized sample, complementing those derived from GC/MS analysis. The combination of the two techniques allows for a positive identification of an unknown compound with high confidence. The practices demonstrated in this note conform to the recommendations by SWGDRUG that multiple techniques are required to confirm seized sample identity.

The benchtop picoSpin 80 ^{1}H NMR solution offers structure selectivity and discriminating power needed to provide an additional layer of structural identification of drug analogues and precursors. This compact instrument can be conveniently placed in workspace-limited labs and testing areas, while enhancing the presumptive testing capabilities of illicit drug screening facilities.

Thermo Scientific™ picoSpin™ 80 NMR spectrometer and Thermo Scientific™ ISQ™ QD Single Quadrupole GC/MS System

References

SWGDRUG home page: http://www.swgdrug.org/ (accessed Jun 17, 2016).

In the United States:
For customer service, call 1-800-766-7000
To fax an order, use 1-800-926-1166
To order online: thermofisher.com

In Canada:
For customer service, call 1-800-234-7437
To fax an order, use 1-800-463-2996
To order online: thermofisher.ca

Find out more at **www.thermofisher.com/nmr**

ThermoFisher SCIENTIFIC

APPLICATION NOTE

No. AN52907

Determination of polymer molecular weight and composition using picoSpin NMR spectroscopy

Authors:
Katherine Paulsen and Daniel Frasco,
Thermo Fisher Scientific, Madison, WI

Key words

NMR, polymer, copolymer, number average molecular weight, compositional analysis

Abstract

Polymer molecular weight determination and copolymer compositional analysis involve the integration of the resonance signals from polymer repeating units and end groups, which are inherently broad. A Thermo Scientific™ picoSpin™ 80 NMR spectrometer is well suited for these analyses. In the example of poly (ethylene glycol) (PEG) acetyl triarm, the number average molecular weight was determined with great ease. In the case of the compositional analysis of a commercial PEG-PPG-PEG block copolymer, Pluronic® L-35, the PEG/PPG ratio determined by a picoSpin 80 NMR agrees well with the manufacturer's product specification. Furthermore, the analyses using an 82 MHz and a 300 MHz NMR yielded almost identical results.

Introduction

The control of the molecular weight and molecular weight distribution (MWD) is essential to obtain and improve certain desired physical properties in a polymer product, and is therefore of great importance in material science[1]. In addition to gel permeation chromatography (GPC) and matrix assisted laser desorption ionization mass spectrometry (MALDI MS)[2], end group analysis using nuclear magnetic resonance (NMR) spectroscopy has long been established as a viable analytical technique for determining the number average molecular weight (M_n) of polymers. For polymers with a defined end group structure, the number of repeating units can be deduced by comparing the resonance signals from repeating units to those of end groups, thereby determining the molecular weight. A similar methodology can be adapted for the compositional analysis of copolymers, so long as the resonance signals from different monomers can be clearly differentiated.

Due to poor molecular rotation and marginally different chemical environments in which the repeating units are situated, resonance signals from polymer repeating units often coalesce as a broad peak, even using high-field NMR spectrometers.[3] However, in the molecular weight analysis and compositional analysis, collective signals from polymer repeating units are used for calculation and monomeric resolution is generally not required. To that end, low-field NMR readily lends itself as a low-cost alternative to high-field instruments, with significant savings on both instrument procurement and upkeep.

In this application note, molecular weight determination of poly(ethylene glycol) (PEG) acetyl triarm and compositional analysis of a polyol using a picoSpin NMR spectrometer are presented. The results of the compositional analysis using an 82 MHz NMR were also compared with those using a high-field, 300 MHz NMR spectrometer.

Experimental

The structures of the polymers examined in this study are shown in Figure 1.

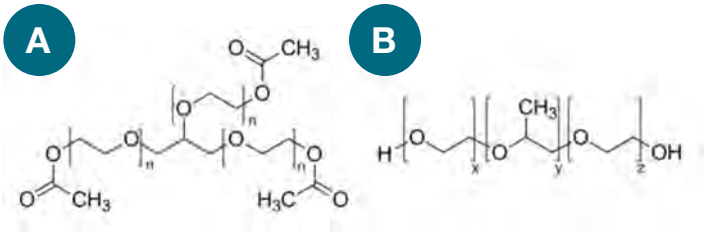

Figure 1: Chemical Structures of: **A)** poly(ethylene glycol) (PEG) acetyl triarm (PEG acetyl triarm), and **B)** poly(ethylene glycol)-block-poly(propylene glycol)-block-poly(ethylene glycol) (PEG-PPG-PEG).

A Thermo Scientific picoSpin 80 NMR spectrometer was used to acquire the spectra of the polymer materials. The spectrometer is an 82 MHz, pulsed, Fourier transform ^{1}H NMR. The instrument contains a 2 Tesla temperature controlled permanent magnet and is fitted with a 40 microliter capillary cartridge used for sample introduction into the spectrometer.

Poly(ethylene glycol) (PEG) acetyl triarm (PEG acetyl triarm) was a crude reaction mixture provided by Dr. Lei Zhu's group in the Department of Macromolecular Science and Engineering at Case Western Reserve University.

The sample was injected neat and 64 scans were acquired. Poly(ethylene glycol)-block-poly(propylene glycol)-block-poly(ethylene glycol) (PEG-PPG-PEG; Pluronic® L-35) was purchased from Sigma-Aldrich.[4] The sample was diluted in equal volume of $CHCl_3$ prior to injection. The data was collected using 16 scans. The 300 MHz NMR data of Pluronic L-35 diluted in $CDCl_3$ was acquired at Case Western Reserve University.

The liquid samples were injected into the capillary cartridge using 1 mL slip-tip polypropylene syringes and 22 gauge blunt-tipped needles. Back-to-back sample injection and data acquisition was separated by a solvent/air/solvent/air flush to thoroughly clean the capillary. Samples were either referenced to chloroform ($CHCl_3$, δ7.26 ppm) or another known signal in the spectrum.

All spectra were acquired using the following acquisition parameters: 90° excitation pulse, 750 ms acquisition time and 5 second recycle delay. Spectral data were processed using the Mnova™ NMR analysis software with a standard set of processing parameters including: Zero filling and phase correction. Apodization was not used.

Results and discussion

Number average molecular weight (M_n) determination. In ^{1}H NMR spectroscopy, the area under each resonance signal is proportional to the molar concentration of the protons being analyzed. Number average molecular weight (M_n) determination by end-group analysis using ^{1}H NMR therefore involves identifying and integrating distinguishable proton signals originating from end-groups and repeating units.

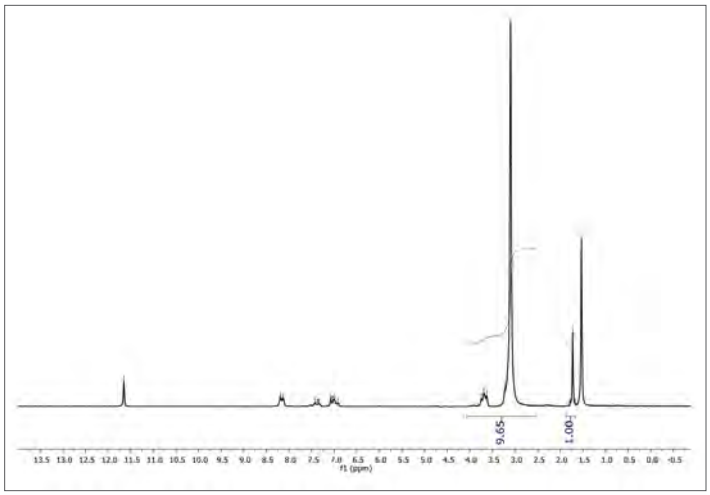

Figure 2: 82 MHz ^{1}H NMR spectrum of PEG acetyl triarm reaction mixture.

Figure 2 shows the ^{1}H NMR spectrum of PEG acetyl triarm obtained using an 82 MHz picoSpin NMR. The acetyl (-$OCOCH_3$) end-group protons resonate as a sharp singlet at δ 1.8 ppm with a normalized peak area of 1.00. The three acetyl moieties contain a total of 9 protons. The PEG repeating group (-OCH_2CH_2-) protons and the glycerol protons resonate between δ 3.1-3.8 ppm with a normalized peak area of 9.65. Each repeating group of PEG contains 4 protons, and the glycerol linkage (–CH_2CHCH_2–) contains 5 protons. Since there are three arms for the polymer, the total number of protons contributing to the signal between δ 3.1-3.8 is 12n+5.

$$\frac{\text{peak area of repeating units and glycerol linkage}}{\text{\# of protons in repeating units and glycerol linkage}} = \frac{\text{peak area of end groups}}{\text{\# of protons in end groups}}$$

$$\frac{9.65}{12n+5} = \frac{1.00}{9},\ n = 6.82 \approx 7 \text{ repeating monomer units}$$

$$M_n = FW_{\text{glycerol linkage}} + FW_{\text{end groups}} + FW_{\text{repeating units}} = 41 + 177 + (44 \times 7 \times 3) = 1142$$

Based on the end group analysis using an 82 MHz picoSpin NMR spectrometer, the number average molecular weight of the PEG acetyl triarm is 1142 g/mol.

Compositional analysis of a PEG/PPG block copolymer.

Figure 3 shows the ^{1}H NMR spectra of Pluronic L-35, a PEG-PPG-PEG copolymer, using (a) an 82 MHz picoSpin NMR spectrometer; and (b) a 300 MHz NMR spectrometer. The two spectra are very similar. In the 82 MHz spectrum, the signals at δ ~0.8 ppm with a normalized peak area of 3.0 are attributed to the methyl (-CH_3) group of PPG. The CH- and CH_2- proton signals from both PPG and PEG are located at δ ~ 3.1-3.4 ppm, with a normalized peak area of 7.65. The contributions to these signals include 3 protons from PPG (one CH- and one CH_2-) and 4 protons from PEG (2 CH_2- groups). The 300 MHz ^{1}H NMR spectrum is essentially the same: the signal from the methyl group resonates at δ 1.1 ppm with a normalized peak area of 3.0, and the CH- and CH_2-proton signals are located at δ ~ 3.3-3.7 ppm with a normalized peak area of 7.77. The minor variances in chemical shift between the two spectra are likely due to the difference in sample concentrations. Because of the higher sensitivity of a 300 MHz NMR instrument, the samples were used in a lower concentration; hence, the difference in chemical shift. The 300 MHz spectrum also offers greater resolution than the 82 MHz one. The increased resolution, however, should have little to no bearing on the results of the compositional analysis, because the collective signals are integrated for the ensuing calculations.

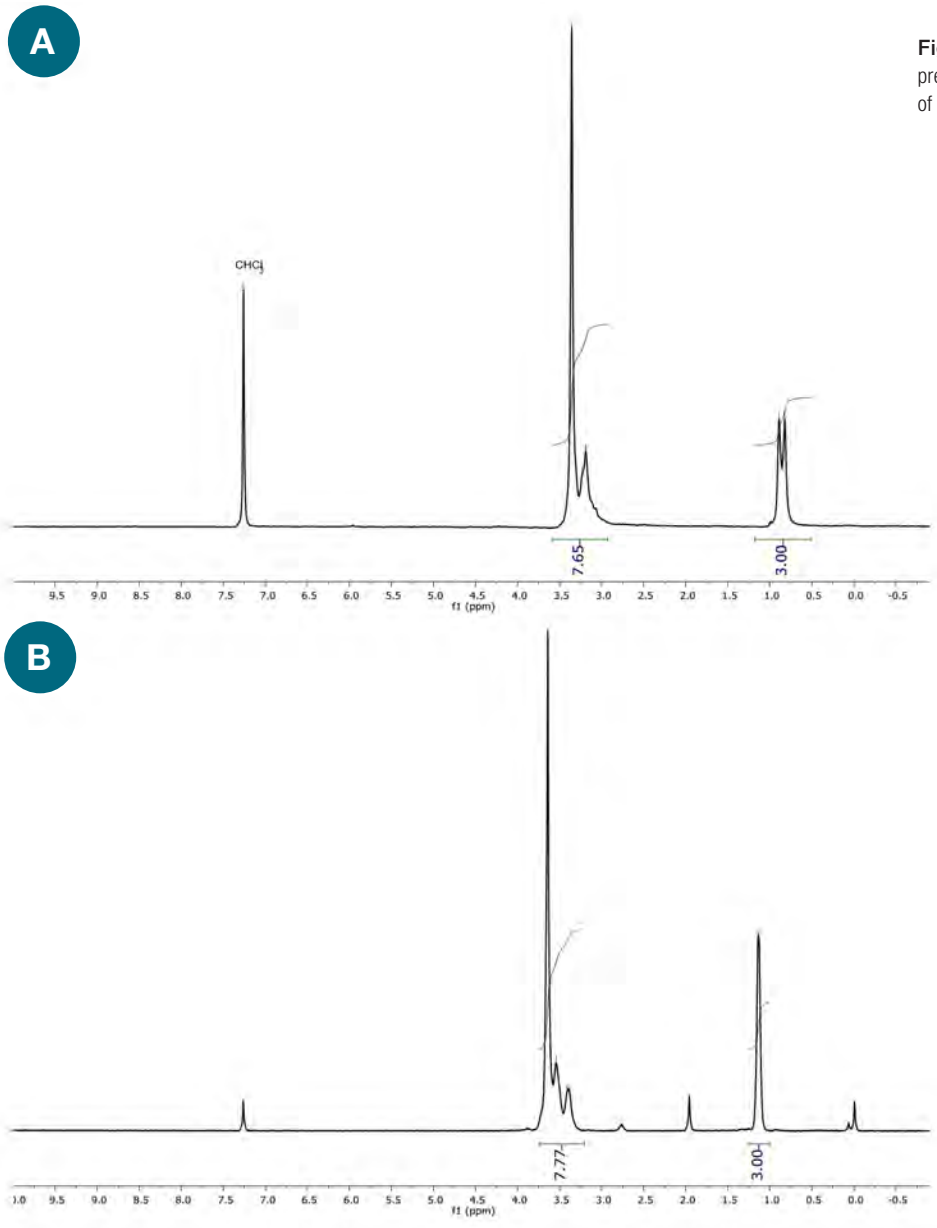

Figure 3: A) 82 MHz ^{1}H NMR spectrum of PEG-PPG-PEG prepared 50:50 (v/v) in $CHCl_3$. **B)** 300 MHz ^{1}H NMR spectrum of PEG-PPG-PEG prepared in $CDCl_3$.

thermo scientific

A detailed compositional analysis using the 82 MHz NMR spectrum is outlined below.

1. Determine the relative moles of PPG, denoted as x, using the signals at δ ~0.8.

$$x = \frac{\text{integral of methyl protons}}{\text{\# of methyl group protons}} = \frac{3.00}{3}$$

$$x = 1.0 \text{ relative moles of propylene glycol}$$

2. Determine the relative moles of PEG, denoted as y, using the signals at δ ~3.1-3,4.

$$\frac{7.65}{4y+3} = \frac{3.00}{3}$$

$$y = 1.16 \text{ relative moles of ethylene glycol}$$

3. Calculate the weight percentages of PEG and PPG.

$$\text{weight \% PEG} = \frac{\text{relative moles PEG} \times \text{MW}_{\text{PEG}}}{\text{relative moles PEG} \times \text{MW}_{\text{PEG}} + \text{relative moles PPG} \times \text{MW}_{\text{PPG}}} \times 100\%$$

$$= \frac{1.16 \times 44}{1.16 \times 44 + 1.0 \times 58} \times 100\% = 46.8\%$$

$$\text{weight \% PPG} = \frac{\text{relative moles PPG} \times \text{MW}_{\text{PPG}}}{\text{relative moles PEG} \times \text{MW}_{\text{PEG}} + \text{relative moles PPG} \times \text{MW}_{\text{PPG}}} \times 100\%$$

$$= \frac{1.0 \times 58}{1.16 \times 44 + 1.0 \times 58} \times 100\% = 53.2\%$$

Based on the 82 MHz NMR spectrum, Pluronic L-35 copolymer contains 46.8 % of PEG and 53.2 % of PPG. The results using the 300 MHz spectrum are essentially the same: 47.4 % of ethylene glycol and 52.6 % of propylene glycol. Both results are in good agreement with the product specification[4], where PEG/PPG (w/w) = 1.

Thermo Scientific picoSpin 80 NMR spectrometer

Conclusions

^{1}H NMR spectroscopy has been established as a powerful tool for polymer characterization, including molecular weight determination and copolymer compositional analysis. Both analyses involve the integration of the resonance signal from polymer repeating units, which are inherently broad. The Thermo Fisher Scientific picoSpin 80 NMR spectrometer is well suited for these investigations. In the example of poly(ethylene glycol) (PEG) acetyl triarm, the number average molecular weight was determined with great ease. In the case of the compositional analysis of a commercial PEG-PPG-PEG block copolymer, Pluronic® L-35, the PEG/PPG ratio determined by a picoSpin 80 NMR agrees well with the manufacturer's product specification. Furthermore, the analyses using an 82 MHz and a 300 MHz NMR yielded almost identical results. The Thermo Fisher Scientific picoSpin 80 NMR spectrometer has proven to be a low-cost alternative to high-field NMR spectrometers for polymer molecular weight determination and compositional analysis.

References

1. Higginbotham, C. L.; Izunobi, J.U. J. Chem. Ed. 2011, 88, 1098-1104

2. Skoog, D. A.; Holler, J. F.; Crouch, S. R. *Principles of Instrumental Analysis*, 6th ed.; Brooks Cole: Pacific Grove, 2006.

3. Bovey, F. A.; Mirua, P. A. *NMR of Polymers*, 1st ed.; Academic Press: San Diego, 1996.

4. Sigma-Aldrich. Poly(ethylene glycol)-block-poly(propylene glycol)-block-poly(ethylene glycol) (PEG-PPG-PEG; Pluronic L-35; CAS No. 9003-11-6). www.sigmaaldrich.com/catalog/product/aldrich/435414

Find out more at **www.thermofisher.com/nmr**

ThermoFisher SCIENTIFIC

APPLICATION NOTE

No. AN52948

Qualitative and quantitative analysis of the polymerization of PS-*b*-P*t*BA block copolymer using picoSpin 80 NMR

Authors:
Katherine Paulsen and Daniel Frasco,
Thermo Fisher Scientific, Madison, WI, USA

Yufeng Zhu, Department of Macromolecular Science and Engineering, Case Western Reserve University, Cleveland, OH, USA

Key words
picoSpin 80, NMR, polymerization, copolymer, number of repeating units, polystyrene

Benefit
The Thermo Scientific™ picoSpin™ 80 NMR spectrometer offers near real-time analytical capability for reaction monitoring due to its unique capillary injection design and compact footprint. The picoSpin 80 NMR has also proven to be a low-cost alternative to high-field NMR spectrometers to quantitatively assess polymerization and to determine copolymer structure.

Abstract
The use of the low-field picoSpin 80 NMR spectrometer offers a near real-time analytical capability for reaction monitoring, largely due to its unique capillary injection design and compact footprint. Despite the broad resonance signals typical for polymers, by carefully selecting the regions where signal changes manifest the involved chemical transformation, the integrated peak area provides valuable insight to the reagent conversion as well as the final product structure.

Introduction
Nuclear magnetic resonance (NMR) spectroscopy has proven to be an invaluable analytical tool for reaction monitoring and optimization by elucidating molecular structure, studying reaction kinetics, monitoring reaction progress and gauging product purity[1]. For polymers however, resonance signals from repeating units often coalesce as broad peaks, even with high-field NMR spectrometers. This is largely due to poor molecular rotation and repeating units being situated in marginally different chemical environments. Low-field NMR such as the picoSpin 80 NMR spectrometer lends itself as a low-cost alternative to high-field instruments for polymerization monitoring, resulting in significant cost savings on both instrument procurement and upkeep.

Presented herein is a case study using a picoSpin 80 NMR spectrometer to monitor the polymerization of *t*-butyl acrylate with a polystyrene reagent. The reaction scheme is shown in Figure 1. By carefully identifying and integrating the resonance signals associated with the monomer, the progress of the polymerization was successfully assessed both qualitatively and quantitatively. The number of *t*-butyl acrylate units incorporated into the final copolymer product was also deduced.

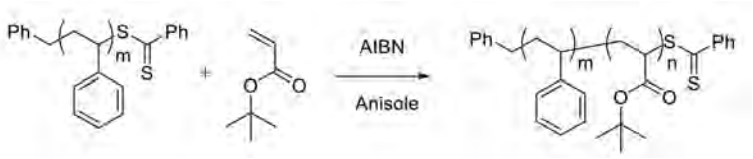

Figure 1: Polymerization of *t*-butyl acrylate with a polystyrene reagent to form PS-*b*-P*t*BA.

Experimental

Monomer *t*-butyl acrylate (*t*BA, 0.150 g, 1.170 mmol), polystyrene reagent (PS, 0.230 g, 0.120 mmol), 2,2'-azobis (2-methylpropionitrile) radical initiator (AIBN, 0.001 g, 0.006 mmol), and anisole (1.156 mL) were added together into a 10 mL flask. The number average molecular weight of PS is 1910.76 g/mol, determined by the end-group analysis using a 500 MHz NMR and confirmed by GPC. The average number of repeating units in PS is 16. This resulted in a molar ratio of 9.75/1 for *t*BA/PS. The mixture was degassed by three freeze-pump-thaw cycles. The mixture was then stirred at 75 °C for 12 h and the polymerization process was observed by ^{1}H NMR spectroscopy.

A picoSpin 80 NMR spectrometer was used to acquire spectra of the polymerization reaction. The instrument is an 82 MHz, pulsed, Fourier transform ^{1}H NMR spectrometer with superior chemical shift resolution and sensitivity. The instrument contains a 2 Tesla temperature controlled permanent magnet and is fitted with a 40 microliter capillary cartridge used for sample injection into the spectrometer.

All samples were manually injected into the capillary cartridge using disposable 1 mL slip-tip polypropylene syringes and 22 gauge blunt-tipped needles. During the reaction, aliquots were taken out and injected directly into the picoSpin capillary cartridge with no sample preparation. Back-to-back sample injection and data acquisition was separated by a solvent/air/solvent/air flush of the capillary cartridge with anisole used as the solvent. Spectra were referenced to the $-CH_3$ signal from anisole (δ3.75 ppm).

All spectra were acquired using the following acquisition parameters: 90° excitation pulse, 750 ms acquisition time and 8 s recycle delay. The spectral data was processed using the Mnova™ NMR analysis program with a standard set of processing parameters including zero filling and phase correction. Apodiation was not used.

Results and discussion

A qualitative look at the polymerization

Figure 1 depicts a narrowly dispersed polystyrene-based reversible addition-fragmentation chain transfer (RAFT) reagent reacting with *t*-butyl acrylate monomer to form a PS-*b*-P*t*BA block copolymer[2-3]. Figure 2 shows the NMR spectrum of the initial reaction mixture containing *t*-butyl acrylate (*t*BA) and polystyrene reagent (PS) in anisole. The signals between δ 1.4–2.8 ppm originate from the 3 protons of the CH_2- and CH- groups of the PS repeating unit. These overlap with the singlet from the 9 *t*-butyl methyl protons of *t*BA (δ 1.7 ppm). The singlet at δ 3.7 ppm is ascribed to the methyl group of anisole. The signals between δ 5.5 – 6.7 ppm correspond to the 3 vinyl protons of *t*BA. Finally, the multiplet in the region δ 6.8 – 7.6 ppm arises from the aromatic rings from both anisole and PS.

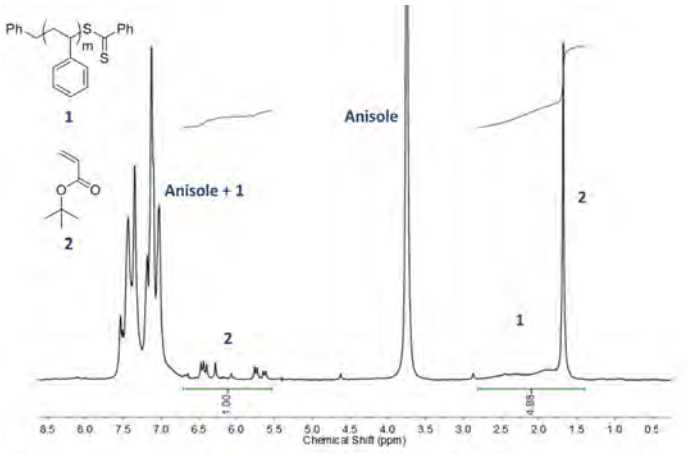

Figure 2: 82 MHz ^{1}H NMR spectrum of the initial reaction mixture containing polystyrene reagent (PS) and *t*-butyl acrylate (*t*BA) in anisole.

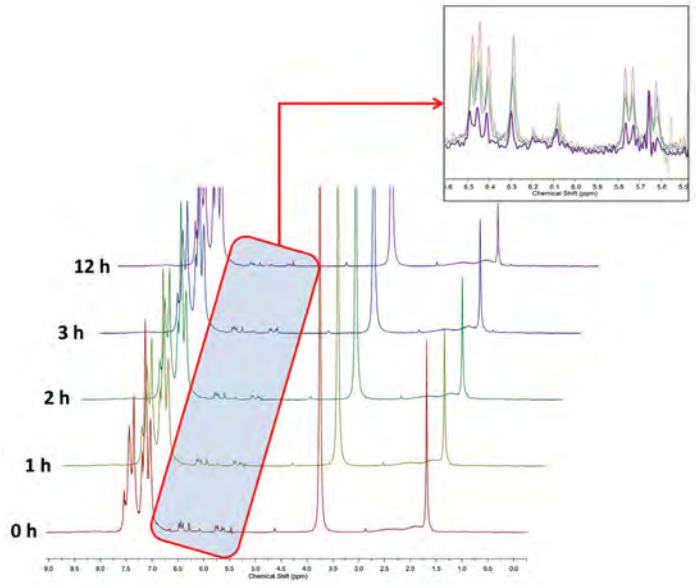

Figure 3: Overlay of the 82 MHz ^{1}H NMR spectral collected at 0, 1, 2, 3, and 12 hour time-points. The insert shows a decrease in intensity of the vinyl protons of *t*BA.

Figure 3 shows the overlaid ^{1}H NMR spectra of the reaction mixture acquired at 5 different time points over the course of the polymerization: 0, 1, 2, 3 and 12 hours, respectively. The main chemical transformation during the polymerization is the opening of the double bonds in the *t*BA monomer, as demonstrated in Figure 4. The insert in Figure 3 clearly demonstrates that the resonance signals from the vinyl protons of *t*BA (δ 5.5–6.7 ppm) decrease as the reaction progresses. A quantitative perspective of the chemical transformation is presented in the subsequent section.

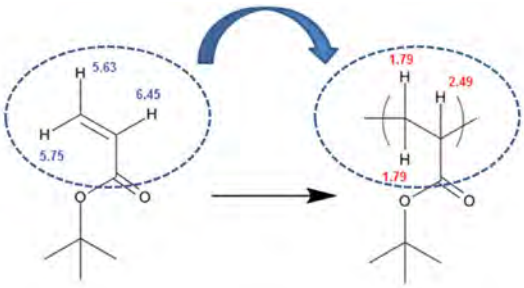

Figure 4: Schematic showing the conversion of vinyl protons to protons in the polymer backbone. The numbers denote the projected chemical shifts of the involved protons by ^{1}H NMR.

It is worth pointing out that the compact footprint of the picoSpin 80 NMR spectrometer allows the instrument to be set up in the laboratory where the chemistry takes place. Furthermore, the unique capillary injection system of the picoSpin minimizes sample workup, offering a near real-time analytical capability critical for reaction monitoring and optimization.

Quantitative Analysis of the Polymerization

Figure 5 shows the ^{1}H NMR spectra of the reaction mixture at *t*=12 hours. As the reaction progressed, the monomer *t*BA was gradually added to the polymer through the opening of the double bonds (Figure 4). Consequently, part of the protons originally contributing to the resonance signals in the region δ 5.5-6.7 ppm were converted to the protons contributing to signals between δ 1.4 – 2.8 ppm. A closer analysis reveals that the ratio $\frac{I_{1.4-2.8\ ppm}}{I_{5.5-6.7\ ppm}}$ increased from 4.88 at *t*=0 to 7.57 at *t*=12 hour.

At *t*=0, there are 9.75 moles of *t*BA for every mole of PS. At *t*=12, the signals between δ 1.4–2.8 ppm include the aliphatic protons from PS, the methyl protons from the *t*-butyl groups in *t*BA, and the protons converted from the vinyl groups in *t*BA. There are 3 aliphatic protons in each PS repeating unit, and there are 16 repeating units in every PS molecule. The total PS protons are therefore 48. The number of methyl protons in *t*BA are 9 × 9.75 = 87.75 and remains unchanged throughout the reaction.

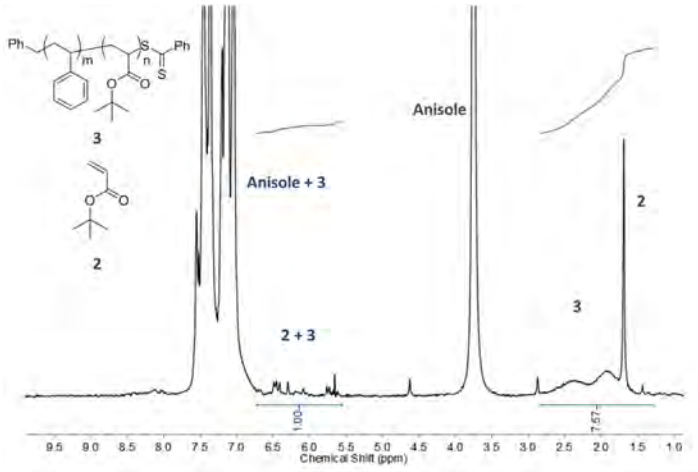

Figure 5: 82 MHz ^{1}H NMR spectrum of the polymerization process after 12 hours at 75 °C.

For the vinyl protons in *t*BA (a total of 3 × 9.75 = 29.25), assuming n% was converted to polymer, 29.25n protons is shifted to the region δ 1.4–2.8 ppm and 29.25 (1-n) protons remain in the region δ 5.5-6.7 ppm.

Based on the calculations below, it was determined that 34% of *t*BA was converted into the block copolymer, corresponding to an average of 34% of 9.75 = 3 *t*BA units in every copolymer molecule.

$$\text{t=12 hour:}\quad \frac{48+29.25n+87.75}{29.25(1-n)} = \frac{7.57}{1.00} \quad\Rightarrow\quad n = 0.34$$

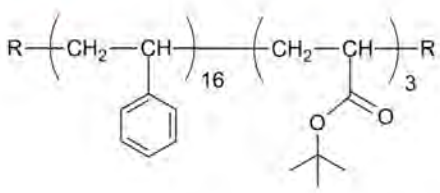

Conclusion

The use of the low-field picoSpin 80 NMR spectrometer offers a near real-time analytical capability for reaction monitoring, largely due to its compact footprint and unique capillary injection design. Despite the broad resonance signals typical for polymers, by carefully selecting the regions where signals can quantitatively manifest the involved chemical transformation, the integrated peak area provides valuable insight to the reagent conversion as well as the final product structure. In the case of the polymerization of PS-*b*-P*t*BA, the vinyl and aliphatic regions were selected for integration. By comparing the signal ratio before and after the reaction, it was determined that 34% of the *t*BA monomer was converted to the copolymer. On average, the final product contains 3 *t*BA units. The described workflow and its underlying principles should be of interest for chemists routinely performing polymer synthesis.

thermo scientific

References

1. Higginbotham, C. L.; Izunobi, J.U. *J. Chem. Ed.* **2011**, *88*, 1098-1104

2. Li, B.; Shi, Y.; Zhu, W.; Fu, Z.; Yang, W. *Polym*. J. **2006**, *38*, 387-394

3. Chiefari, J.; Chong, Y. K.; Erocle, F.; Krstina, J.; Jeffery, J.; Le, T. P. T.; Mayadunne, R.T.A.; Meijs, G. F.; Moad, C. L.; Moad, G.; Rizzardo, E.; Thang, S. H. *Macromolecules* **1998**, *31*, 5559-5562.

Find out more at **thermofisher.com/picospin**

AN52948_E 03/17M

ThermoFisher SCIENTIFIC

APPLICATION NOTE

No. AN52976

Analysis of acetanilide herbicides and their rotational isomers by picoSpin 80 NMR

Author:
Daniel Frasco, Thermo Fisher Scientific, Madison, WI, USA

Key words: NMR, agrochemical, pesticide, herbicide, isomers

Application benefit

Thermo Scientific™ picoSpin™ 80 Series II NMR is a powerful analytical tool to qualitatively and quantitatively analyze acetanilides and their isomers. Compared to the traditional methods using chromatography and high-field NMR, the NMR method using picoSpin 80 is cost-effective, time-efficient and straightforward.

Abstract

The picoSpin 80 Series II NMR spectrometer can be used as a low-cost alternative to a high-field instrument for the qualitative and quantitative analysis of acetanilide herbicides. The picoSpin offers adequate resolution to differentiate between acetanilide isomers and a facile means to determine the isomeric ratio by simply integrating the corresponding signals.

Introduction

Acetanilides are a class of preemergent herbicides that inhibit the growth of unwanted grasses and weeds associated with the production of agricultural crops like corn, soybeans, cotton and peanuts.[1] The general structure of acetanilide herbicides is shown in Figure 1.

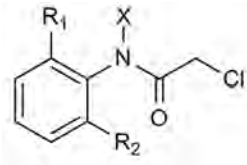

Figure 1: General Structure of Acetanilide Herbicides

Acetanilides represent some of the most widely used pesticides for both crop and non-crop use. In 2007, metolachlor and acetochlor, two representative acetanilides, were the 4th and 5th most used pesticides in the United States, with an approximated use of around 30 million pounds each.[2]

Due to the widespread use of these herbicides, it is important to understand the metabolic pathways of these molecules and identify their transformation products. Special attention has to be paid to stereoisomers, as they could have vastly different reactivity and degradation pathways.[3-4] For acetanilides, amide *cis-trans* isomerization has been well established where the rotation of the amide bond from the substituted aromatic ring is hindered.[3-6]

Quantitative determination of the isomeric ratio in a mixture presents a particular analytical challenge. Traditionally, a number of techniques including Gas Chromatography-Mass Spectrometry (GC-MS), Capillary Zone Electrophoresis (CZE), High-Performance Liquid Chromatography (HPLC) and high-field Nuclear Magnetic Resonance (NMR), have been used to analyze the acetanilide isomers.[4-5] Chromatographic techniques including GC-MS, HPLC and CZE often require time-consuming method development. The chromatography runs are generally on the order of 10-15 min, often with non-baseline resolution, giving rise to the uncertainty in isomeric ratio. High-field NMR has proven to be a powerful tool for the analysis of acetanilide isomers by integrating their signals. However, the associated intensive capital and space investment often prohibits their use in smaller facilities or in factories where pesticide production is taking place.

This work demonstrates the qualitative and quantitative analyses of a group of acetanilides with varying structural complexity using an inexpensive and portable picoSpin 80 Series II NMR spectrometer. NMR spectra were obtained in as little as a few seconds compared to the longer analysis times of other techniques. Additionally, a facile means to determine the isomeric ratio is also presented. This methodology was applied to investigate the impact of solvent polarity on the ratio of *cis-trans* rotational isomers of the acetanilide.

Experimental

A picoSpin 80 Series II NMR spectrometer was used to acquire the spectra of acetanilide herbicides. The spectrometer is an 82 MHz, pulsed, Fourier transform ^{1}H NMR. The instrument contains a 2 Tesla temperature controlled permanent magnet and is fitted with a 40 microliter capillary cartridge used for sample introduction into the spectrometer.

All samples were purchased from Sigma Aldrich and were used as received. Both solid and liquid samples were analyzed in deuterated solvent and injected into the capillary cartridge using 1 mL slip-tip polypropylene syringes and 22 gauge blunt-tipped needles. Back-to-back sample injection and data acquisition was separated by a solvent/air/solvent/air flush to thoroughly clean the capillary.

All spectra were acquired using the following acquisition parameters: Between 1 and 64 scans, 90° excitation pulse, 750 ms acquisition time and 8 second recycle delay. Spectral data was processed using the Mnova™ NMR analysis software with a standard set of processing parameters.

Results and discussion

Figure 2 depicts the ^{1}H NMR spectrum of propachlor as a 1.8M solution in deuterated DMSO. The signals corresponding to each proton can be readily assigned. The doublet resonating at δ 1.0 ppm corresponds to the two methyl groups of six protons, the singlet at δ 3.8 ppm originates from the two methylene protons alpha to the carbonyl, the septet at δ 4.8 ppm is from the one isopropyl methine proton, and the five protons from the aromatic ring are located between δ 7.1-7.6 ppm.

Substitutions adjacent to the amide bond on the aromatic ring could hinder the rotation of the amide bond, resulting in rotational isomers (*cis-trans* isomers). This phenomenon has been extensively studied using high-field NMR spectrometers; although the ^{1}H NMR spectrum of alachlor

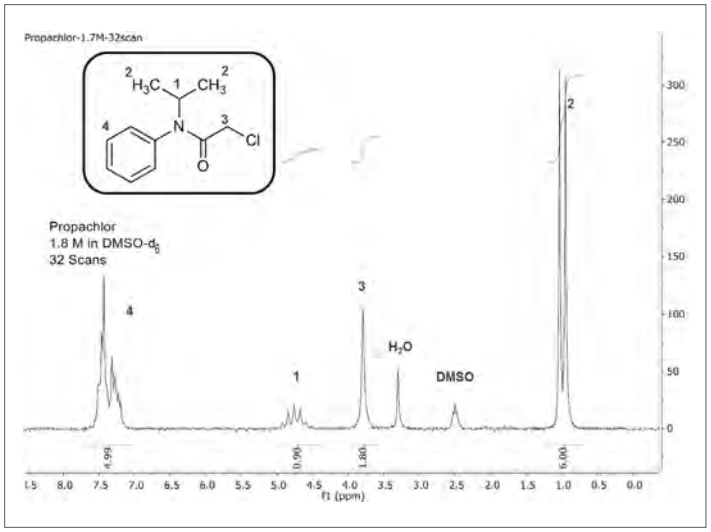

Figure 2: ^{1}H NMR spectrum of a 1.8M solution of propachlor in DMSO-d_6 acquired in 5 minutes using 32 scans. The residual DMSO signal and water present in the deuterated solvent are identified.

in Figure 3 clearly indicates that the resolution of the picoSpin 80 Series II is sufficient to resolve the signals corresponding to each isomer. In the case of alachlor, ethyl groups are located at the 2 and 6 position of the aromatic ring. The orientation of the carbonyl group away from the aromatic ring corresponds to the *trans-* isomer, and the one aligning toward the aromatic ring corresponds to the *cis-* isomer. In Figure 3, the three methoxy protons from the two isomers can be seen as two singlets at δ 3.3 and 3.4 ppm. The two methylene protons next to the carbonyl show a significant difference in chemical shift due to their change in proximity to the aromatic ring in the two isomers. They are present as singlets at δ 3.8 ppm (*trans-*) and δ 4.7 ppm (*cis-*). The two methylene protons located between the amide nitrogen and the methoxy oxygen resonate at δ 4.9 ppm for both isomers, although a small shoulder ascribed to the minor *cis-* isomer can be observed, indicating a subtle difference caused by the isomerism.

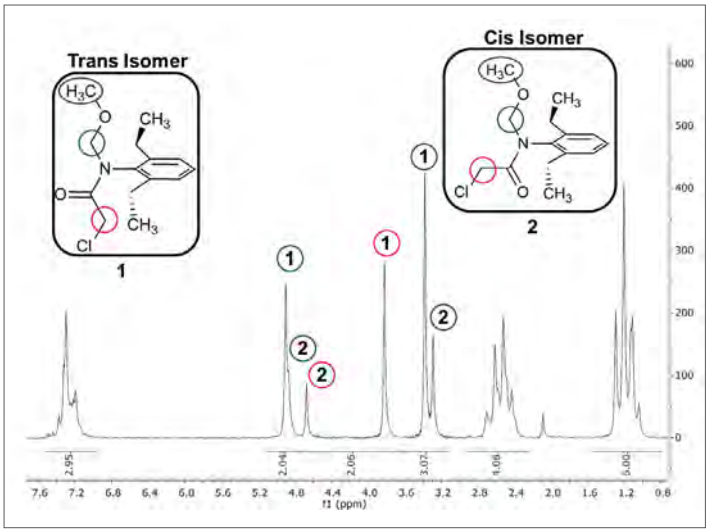

Figure 3: ^{1}H NMR spectrum of a 3.7M solution of alachlor in DMSO-d_6 acquired using 32 scans. Signals labeled as **1** correspond to the trans isomer and **2** correspond to the cis isomer. Unlabeled multiplets represent an overlap of *trans* and *cis* signals.

The protons corresponding to the ethyl functional groups resonating between δ 1.0-1.3 ppm and δ 2.4-2.7 ppm and the aromatic signals located at δ 7.1-7.5 ppm cannot be differentiated between the two isomers.

Figure 4 shows the NMR spectra of three acetanilides: butachlor, alachlor and acetochlor. All three structures have substitution at the 2- and 6- position of the aromatic ring, leading to *cis-/trans* isomerism. Compared to alachlor, both butachlor and acetochlor have longer alkyl side chains attached to the oxygen. In addition, acetochlor has unsymmetrical ring substituents. These structural differences in butachlor and acetochlor compared to alachlor are annotated in their respective ^{1}H NMR spectra (Figure 4.)

Figure 5 shows the NMR spectra of alachlor in three different solvents. As the solvent polarity decreases from DMSO-d_6 to $CDCl_3$, the isomeric ratio (*trans/cis*) increases. The results are also summarized in Table 1. Using the most nonpolar solvent $CDCl_3$, the trans to cis ratio was 92.2% to 7.8%, which was similar to previously reported data in $CDCl_3$.[4]

The dependence of alachlor isomer distribution on solvent polarity has been studied previously using high-field NMR instruments, and similar trends have been reported.[3-4] For alachlor and other similar molecules with amide *cis-trans* isomerization, the transition state between the two isomers is characterized by a partial C-N bond rotation. This transition state for amide bond rotation is less polar compared to its cis and trans isomers. In more non-polar solvents, the energy of the transition state decreases; thus, promoting the isomerization. Since the trans isomer is more stable than the cis isomer,[3, 6] the *trans/cis* ratio increases as solvent polarity decreases.

This data confirms that the choice of solvent is critical to the isomer distribution of acetanilide herbicides in solution, and that the picoSpin 80 Series II NMR spectrometer can easily examine this ratio quantitatively.

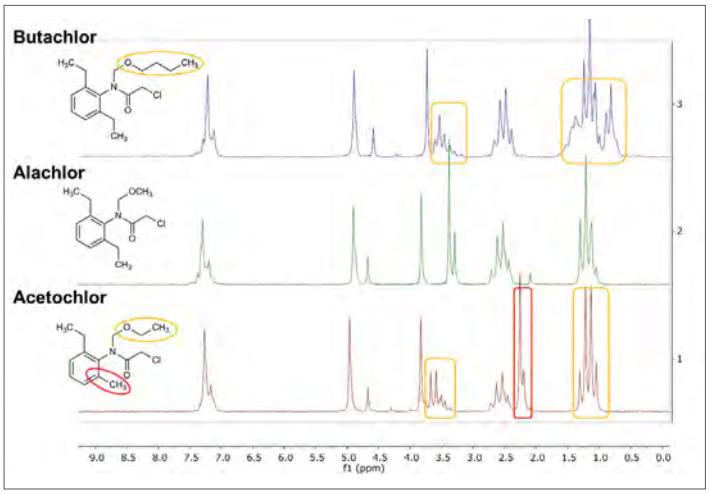

Figure 4: Stacked ^{1}H NMR spectra of butachlor, alachlor and acetochlor in DMSO-d_6. The structural changes of butachlor and acetochlor compared to alachlor are highlighted.

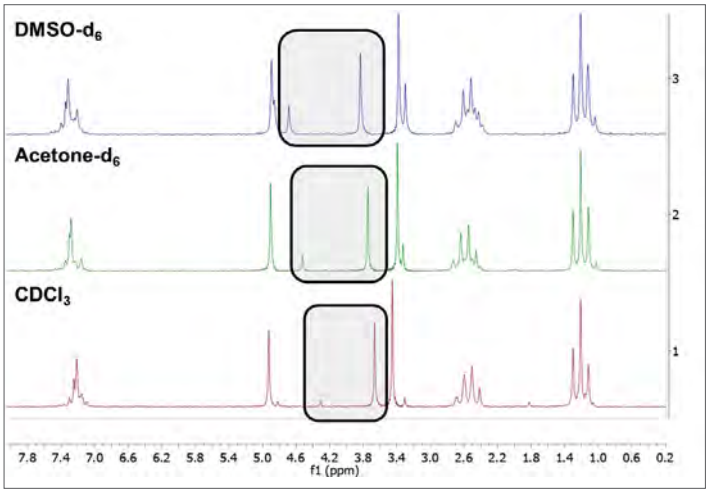

Figure 5: ^{1}H NMR spectra of a 1M solution of alachlor using three different deuterated solvents.

Solvent	Relative Polarity	% Trans Isomer	% Cis Isomer
DMSO-d_6	0.444	73.7	26.3
Acetone-d_6	0.355	83.6	16.4
$CDCl_6$	0.259	92.2	7.8

Table 1: The effect of solvent polarity on isomer distribution in alachlor. **All samples were analyzed in triplicate and the average values are reported.**

Conclusions

The picoSpin 80 Series II NMR spectrometer can be used as a low-cost alternative to a high-field instrument for the qualitative and quantitative analysis of acetanilide herbicides. Some acetanilide molecules are present as rotational isomers due to hindered rotation of the amide bond.

thermo scientific

The picoSpin offers adequate resolution to differentiate the isomers and a facile means to determine the isomeric ratio by simply integrating the corresponding signals. The results clearly suggest that solvent polarity has a profound impact on the isomeric distribution in solution, and great caution should therefore be exercised when analyzing and interpreting the isomeric ratio.

picoSpin 80 Series II NMR spectrometer

References

1. Morton, M. D.; Walters, F. H.; Aga, D. S.; Thurman, E. M.; Larive, C. K. *J. Agric. Food Chem.* **1997**, *45*, 1240-1243

2. *Pesticides Industry Sales and Usage: 2006 and 2007 Market Estimates.* United States Environmental Protection Agency, **2011**, https://www.epa.gov/sites/production/files/2015-10/documents/market_estimates2007.pdf. Accessed 3 January 2017.

3. Schmidt, W. F.; Hapeman, C. J.; Waters, R. M.; Johnson, W. E. *J. Agric. Food Chem.* **1995**, *43*, 1724-1729

4. Aga, D. S.; Heberle, S.; Rentsch, D.; Hany, R.; Muller, S. R. *Environ. Sci. Technol.* **1999**, *33*, 3462-3468

5. Cardoza, L. A.; Cutak, B. J.; Ketter, J.; Larive, C.K. *J. Chromatogr.* A **2004**, *1022*, 131-137

6. Harrison, R. K.; Stein, R. L. *J. Am. Chem. Soc.* **1992**, *114*, 3464-3471

Find out more at **thermofisher.com/nmr**

ThermoFisher SCIENTIFIC

AN52976 0517

thermo scientific

APPLICATION NOTE AN52979

Hydrogen content determination by picoSpin NMR

Author

Daniel Frasco
Thermo Fisher Scientific
Madison, WI, USA

Application benefit

The picoSpin 80 Series II NMR spectrometer serves as a cost-effective analytical tool for hydrogen content determination. The picoSpin NMR spectrometer has the advantage of increased functionality compared to time-domain instruments and a low cost of ownership compared to high-field NMR spectrometers.

Keywords

NMR, fuels, petroleum, hydrogen content

The Thermo Scientific picoSpin 80 Series II spectrometer.

Abstract

Nuclear Magnetic Resonance (NMR) is an important tool for measuring hydrogen content in fuel. However, time domain NMR instruments (described below) offer little flexibility, and high-field frequency domain NMR instruments (described below) can be prohibitively expensive. The Thermo Scientific™ picoSpin™ 80 Series II NMR spectrometer can serve as a flexible and economical alternative to time-domain and high-field NMR for this application. In this note, a range of reference compounds and fuel standards were analyzed using a picoSpin 80 Series II NMR spectrometer and the results were compared to their theoretical values as well as to those obtained experimentally using a high-field NMR. For hydrogen content determination, the picoSpin 80 Series II NMR spectrometer offers accuracy and precision comparable to the high-field NMR measurements described in the literature.

Introduction

The combustion of hydrocarbon containing fossil fuels currently serves as the largest source of energy worldwide. The more hydrogen attached to each carbon in the hydrocarbon, the lower the oxidation state of that carbon and the greater the energy released during combustion. Because of this, the hydrogen content is an important parameter of petroleum distillate products.[1]

A number of methods have been developed to determine the hydrogen content in petroleum products. ASTM D5291, a combustion method for determining the hydrogen content of petroleum fuels is limited in that it is not suitable for samples with a low boiling range and is also a destructive technique which restricts repeatability studies.[2] Nuclear Magnetic Resonance (NMR) has long been used for the determination of hydrogen content in petroleum hydrocarbons and various ASTM methods have been published. Earlier NMR methods (ASTM D3701 and ASTM D4808) made use of obsolete continuous-wave spectrometers.[3-4] Subsequently, an updated method ASTM D7171 was published for determining the hydrogen content of middle distillates using a pulsed time-domain (TD) NMR spectrometer.[5] TD-NMR quantifies materials using their different relaxation properties and is found in quality control labs in a variety of industries. However, it is inadequate for obtaining frequency spectra, thus is not capable of structural analysis like frequency-domain NMR spectrometers. Methods for determining hydrogen content in petroleum products have been developed for high-field NMR spectrometers as well, but these instruments are expensive to purchase and maintain, and require a specific NMR facility apart from the factory or testing laboratory.[1,6]

ThermoFisher SCIENTIFIC

In this application note, the picoSpin 80 Series II NMR spectrometer was used to determine the hydrogen content in a range of reference materials and petroleum fuel standards. The data shows that the picoSpin NMR spectrometer can serve as an effective, low-cost alternative to high-field NMR for hydrogen content determination.

Experimental

A picoSpin 80 Series II benchtop NMR spectrometer was used to acquire spectra for hydrogen content determination. The spectrometer is an 82 MHz, pulsed, Fourier transform ^{1}H NMR. The instrument contains a 2 Tesla temperature controlled permanent magnet heated to a temperature of 36 °C and is fitted with a 40 microliter capillary cartridge used for sample introduction into the spectrometer. All samples were purchased from Sigma Aldrich® and were used as received.

For hydrogen content determination, a vial was placed on an analytical balance and ~45mg of hexamethyldisiloxane (HMDSO) was added. The mass was recorded and the balance was tared. Then ~300mg of the sample was added to the same vial and the mass was recorded. The vial was capped and shaken until adequately mixed. Five runs were prepared for each sample. The samples were injected into the capillary cartridge using 1 mL slip-tip polypropylene syringes and 22 gauge blunt-tipped needles. All spectra were acquired using 16 scans, 4000 acquisition points and a recycle delay of 40 seconds.

Results and discussion

To determine hydrogen content using the pulsed picoSpin 80 NMR spectrometer, an appropriate internal standard was first selected. Hexamethyldisiloxane (HMDSO) was chosen for this application because it is chemically inert, has a high boiling point, has similar hydrogen content to relevant petroleum samples, and its ^{1}H NMR signal resonates in a region that does not overlap with the samples of interest.[1] Once the spectrum of the mixture containing the internal standard HMDSO and the sample of interest was obtained, the following equation was used to determine the hydrogen content of the sample.

$$H\ (wt\%) = \frac{I\ (Sample)}{I\ (HMDSO)} \times \frac{W\ (HMDSO)}{W\ (Sample)} \times H\ (wt\%)\ (HMDSO)$$

In this equation, the percent hydrogen by weight was determined using the recorded weight of the HMDSO and sample as well as the integration of the peak area of the HMDSO singlet and the combined peak areas of the sample signals. The percent hydrogen of HMSDO has a known value of 11.17% and was used in the equation. An example of a ^{1}H NMR spectrum used for calculating percent hydrogen content in this study is shown with the integrations labeled in Figure 1.

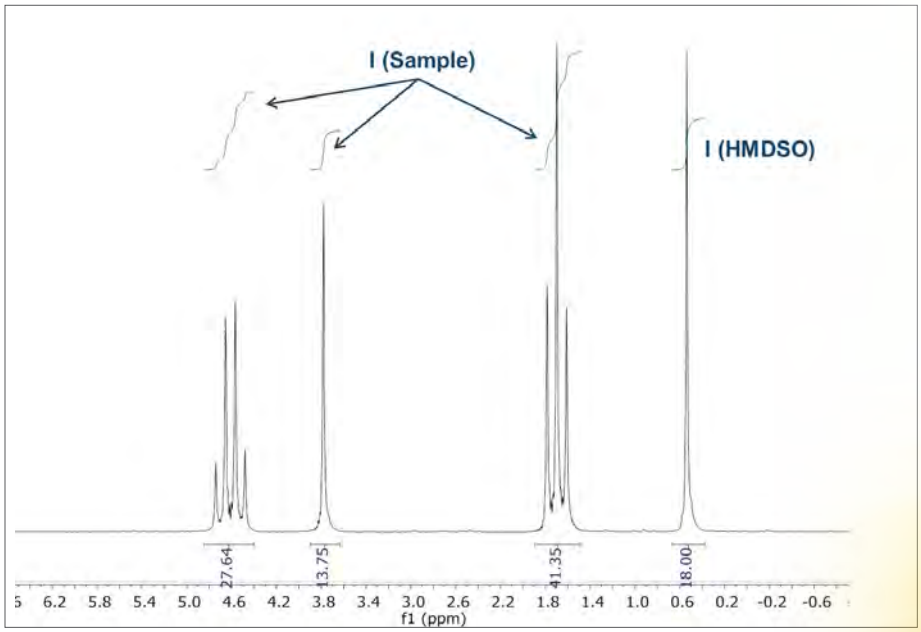

Figure 1: ^{1}H NMR spectrum of diethyl malonate with HMDSO internal standard

To examine the applicability of the picoSpin 80 NMR spectrometer for determining hydrogen content over a range of samples, several reference compounds with known hydrogen content, and published results from other NMR instruments were analyzed.[1,5,6] The reference compounds were first used to examine the precision of the hydrogen content measurement method. The six reference compounds selected represent a hydrogen content range from ~7-15 percent (Table 1). The reported "Ave %H" is an average of 5 runs and the percent relative standard deviation (%RSD) for each compound is shown. In all cases, the %RSD was below 1%. The average %RSD of the six compounds analyzed in this work was 0.44%, on par with the reported results using a high-field instrument.[1]

The accuracy of this method for determining hydrogen content was also examined by using the theoretical % hydrogen content to calculate the relative percent error for each sample. The 6 reference samples examined with the picoSpin spectrometer gave a range of relative error between 0.56% and 2.59%.

These relative error values generally track those reported using a high-field NMR spectrometer, which examined 25 reference samples and reported a range of relative error between -10.58% and 2.65%.[1] On average, the picoSpin method gave an average of 1.58% compared to the high-field instrument which reported 2.75% relative error. The results indicate the low-field picoSpin NMR spectrometer was able to measure hydrogen content of selected reference compounds with similar accuracy to a high-field instrument.[1]

Three ASTM fuel standards were then analyzed and results are summarized in Table 3.

Sample	Ave %H	%RSD
Diethyl Malonate	7.72	0.36
Toluene	8.80	0.32
Mesitylene	10.23	0.19
Cyclohexanone	10.44	0.44
2-Nonanone	13.09	0.41
Dodecane	15.51	0.89

Table 1: Average hydrogen content and % relative standard deviation of five runs per reference sample determined using picoSpin 80 NMR.

Sample	Ave %H	%H theoretical	%Relative error
Diethyl Malonate	7.72	7.55	2.22
Toluene	8.80	8.75	0.56
Mesitylene	10.23	10.06	1.68
Cyclohexanone	10.44	10.27	1.63
2-Nonanone	13.09	12.76	2.59
Dodecane	15.51	15.39	0.77

Table 2: Accuracy of picoSpin 80 NMR spectrometer for determining hydrogen content using five runs per reference sample.

Standard D5307	%H by NMR	Standard D5580	%H by NMR	Standard D5134	%H by NMR
Test 1	15.38	Test 1	14.36	Test 1	14.33
Test 2	15.31	Test 2	14.37	Test 2	14.38
Test 3	15.32	Test 3	14.60	Test 3	14.27
Test 4	15.23	Test 4	14.30	Test 4	14.14
Test 5	15.41	Test 5	14.38	Test 5	14.50
Average	15.33	**Average**	14.40	**Average**	14.32
Theoretical	15.18	**Theoretical**	14.61	**Theoretical**	14.38
%Relative Error	0.98	**%Relative Error**	-1.43	**%Relative Error**	-0.39
%RSD	0.41	**%RSD**	0.71	**%RSD**	0.83

Table 3: . Hydrogen content determination using fuel standards.

ASTM D5307 Crude Oil Internal Standard has a calculated theoretical hydrogen content of 15.18% and is made up of a mixture of C14-C17 hydrocarbons. This is comparable to diesel fuel which typically contains a mixture of C10-C19 hydrocarbons. The average percent hydrogen using the picoSpin spectrometer was determined to be 15.33% which gave a relative error of 0.98% when compared to the theoretical value. The ASTM D5580 Calibration Mix 4 is composed primarily of 2,2,4-trimethylpentane, an important component in gasoline. The picoSpin method yielded a hydrogen content of 14.40%, which gave a relative error of -1.43%. The final standard analyzed was ASTM D5134 Splitter Linearity Check Mix. The obtained hydrogen content of 14.32% also matched closely with its theoretical value of 14.38% with a relative error of -0.39%. ASTM D5580 contained a mixture of C6-C8 hydrocarbons, and ASTM 5134 contains a mixture of C6-C9 hydrocarbons, both of which are within the typical C4-C12 hydrocarbon range of gasoline.

Conclusions

Although there are existing ASTM methods for determining the hydrogen content of fuel and petroleum using NMR spectroscopy, the instruments involved are either obsolete, or limited in their applications. It has been previously shown that high-field NMR is capable of determining the hydrogen content of fuel samples.[1,6] In this work, six reference compounds representing a range of hydrogen contents were analyzed by the picoSpin 80 benchtop NMR spectrometer. The accuracy and precision of the measurement were found to be similar to those obtained with high field instruments.

Three fuel standards mimicking actual fuels were also analyzed, and the hydrogen content agree well with the theoretical and high-field NMR measurements. These results indicate that the picoSpin 80 spectrometer is capable of providing hydrogen content information with similar accuracy and precision to high-field instruments NMR at a significantly reduced cost of ownership.

References

1. Mondal, S.; Kumar, R.; Bansal, V.; et al. *J. Anal. Sci. Technol*. **2015**, 6: 24

2. ASTM-D5291, *Standard Test Methods for Instrumental Determination of Carbon, Hydrogen, and Nitrogen in Petroleum Products and Lubricants*. ASTM: West Conshohocken, PA, 1992

3. ASTM-D3701, *Standard Test Method for Hydrogen Content of Aviation Fuels by Low Resolution Nuclear Magnetic Resonance Spectroscopy*. ASTM: West Conshohocken, PA, 1992

4. ASTM-D4808, *Standard Test Methods for Hydrogen Content of Light Distillates, Middle Distillates, Gas Oils, and Residua by Low Resolution Nuclear Magnetic Resonance Spectroscopy*. ASTM: West Conshohocken, PA, 1992

5. ASTM-D7171, *Standard Test Method for Hydrogen Content of Middle Distillate Petroleum Products Low-Resolution Pulsed Nuclear Magnetic Resonance Spectroscopy*. ASTM: West Conshohocken, PA, 2011

6. Khadim, M. A.; Wolny, R. A., Al-Dhuwaihi, A. S.; et. al. Arab. J. Sci. Eng. **2003**, 28(2A) 147-162

Find out more at **thermofisher.com/nmr**

ThermoFisher SCIENTIFIC

thermo scientific

APPLICATION NOTE AN52995

Evaluation of fluoroorganic compounds with benchtop ^{19}F NMR

Author

Dean Antic, Ph.D.,
Thermo Fisher Scientific
Boulder, CO, USA

Application benefits

With a dedicated Thermo Scientific™ picoSpin™ 80 ^{19}F nuclear magnetic resonance (NMR) spectrometer, spectral acquisition is as easy as proton NMR. Due to the unique attributes of fluorine nuclei, the ^{19}F NMR spectra are easy to interpret, and provide a wealth of molecular structure information as well as its associated chemical environment.

Keywords

Fluoroorganic compounds, ^{19}F NMR, fluorotelomer, hydrofluorocarbon, *J* coupling, multiplicity

Abstract

Fluorine-19 NMR adds a new dimension in the analysis portfolio of fluorine containing compounds. The broader chemical shift range in ^{19}F NMR helps resolve individual fluorine containing functional groups, while the often large variable magnitude of ^{19}F-^{19}F and ^{1}H-^{19}F coupling provides additional insight into structural effects. Furthermore, first-order coupling and highly resolved resonance lines simplify analysis.

Introduction

Fluorine (^{19}F) plays an important role in pharmaceutical, agrochemical, and medicinal chemistry because the judicious placement of fluorine atoms in a molecule can have a significant influence on its chemical and physical properties. While the steric impact of replacing a hydrogen (^{1}H) atom with fluorine is minimal, the electron withdrawing and inductive field effects from a single fluorine nucleus are profound, affecting such properties as acidity, lipophilicity, and polarity. Examples of fluoroorganic compounds, with varying degree of structural complexity and fluorination, are shown in Figure 1. Biologically active pharmaceutical and agrochemical compounds incorporating fluorine are typically “lightly” fluorinated, containing one or only a few fluorine-containing substituents. Electronic liquids, on the other hand, are oligo perfluorocarbon compounds. They are chemically inert and are often used as lubricants and in low temperature heat transfer applications.

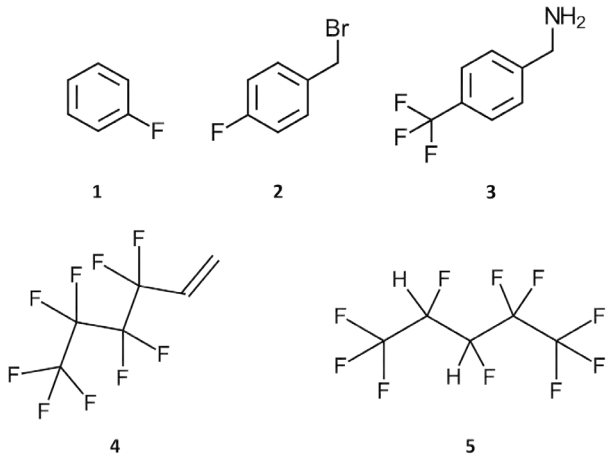

Figure 1: Chemical structures of the fluoroorganic compounds used in this study. (1) Fluorobenzene; (2) 4-fluorobenzyl bromide; (3) [4-(trifluoromethyl)phenyl]methanamine; (4) perfluoro-n-butyl ethylene, trade name Zonyl® PFBE; and (5) 2H,3H-decafluoropentane, trade name Vertrel® XF.

ThermoFisher SCIENTIFIC

^{19}F is one of the most studied nuclides after ^{1}H and ^{13}C in NMR spectroscopy. The advantages of ^{19}F NMR are multifold:

1. For lightly fluorinated bioactive molecules, the relatively small number of fluorine atoms yield fewer signals for easy spectral interpretation.

2. Fluorine couples strongly to other ^{19}F nuclides as far as six bonds away, while also coupling to proximate ^{1}H nuclei and carbon atoms. The resulting ^{19}F NMR spectrum is therefore information-rich in molecular structure as well as associated chemical environment.

3. The ^{19}F NMR spectra are typically first-order in nature in that spin-spin coupling follows the n+1 rule for multiplicity.

4. Being the most electronegative element on the periodic table, ^{19}F displays large shift dispersion (from -300 ppm to 400 ppm), resulting in far larger chemical shifts in ^{19}F spectra than in ^{1}H, and a much smaller probability of peak overlapping.

To demonstrate the wealth of ^{19}F spectral information, in this application note, we present the ^{19}F NMR spectra of a series of commercially available fluoroorganic compounds, obtained using a Thermo Fisher Scientific picoSpin 80 ^{19}F NMR spectrometer.

Experimental

Spectra were acquired using a picoSpin 80 NMR spectrometer. The spectrometer is a pulsed, Fourier transform ^{19}F NMR permanent magnet instrument equipped with a capillary cartridge probe. To ensure the highest sensitivity, the spectrometer was tuned to the fluorine Larmor frequency of 77 MHz. The spectrometer's capillary cartridge was fitted with micro-fluidic inlet and outlet connectors that allow liquid sample injection into the spectrometer's RF coil. The fluid path was Teflon/Quartz capillary tubing with a total flowpath volume of 40 microliters (µL). Liquid samples were introduced by manual injection using a disposable 1 mL syringe and a 22-gauge blunt tip needle. Hexafluorobenzene (HFB, C_6F_6) was added to fluorinated samples at approximately 1% (v/v) concentration as an internal shift reference. Hexafluorobenzene is a high fluorine density compound providing a strong fluorine signal, and is assigned a chemical shift value of -164 ppm. Due to large shift dispersion and solubility requirements of fluorine compounds, other reference compounds, such as fluorotrichloromethane (0 ppm), trifluoromethylbenzene (-63.2 ppm), trifluoroacetic acid (-76.2 ppm), and ethyl trifluoroacetate (-75.8 ppm), are also used to capture the full range of possible chemical shifts.

Spectra were acquired using the following acquisition parameters: a 90° RF excitation pulse, a 1000 ms acquisition time, and a 10 second recycle delay. The spectral width was adjusted to capture the large chemical shift dispersion of the ^{19}F spectrum. All spectra were acquired with signal averaging. Spectral data were stored in a JCAMP-DX file format and imported into MestreLab Research's Mnova™ NMR analysis program for processing. Standardized data processing was applied across all spectra, specifically, by applying zero filling, applying phase correction, and filtering using exponential Apodization.

Results and discussion

Examples of lightly fluorinated compounds

The ^{19}F NMR spectra of two mono-substituted aromatic fluoroorganic compounds, and one trifluoromethyl-substituted phenylmethylamine are presented in Figure 2. Fluorine substituents on the aromatic ring generally absorb in the same region (from -200 ppm to -100 ppm) because shielding zones due to the ring currents in the benzene ring have little influence on fluorine atoms. The mono-fluorine substituted aromatic experiences $^{3}J_{FH}$ and $^{4}J_{FH}$ coupling to ring protons, resulting in complicated but well-defined multiplets. The trifluoromethyl group (CF_3) in compound 3, on the other hand, appears as a singlet.

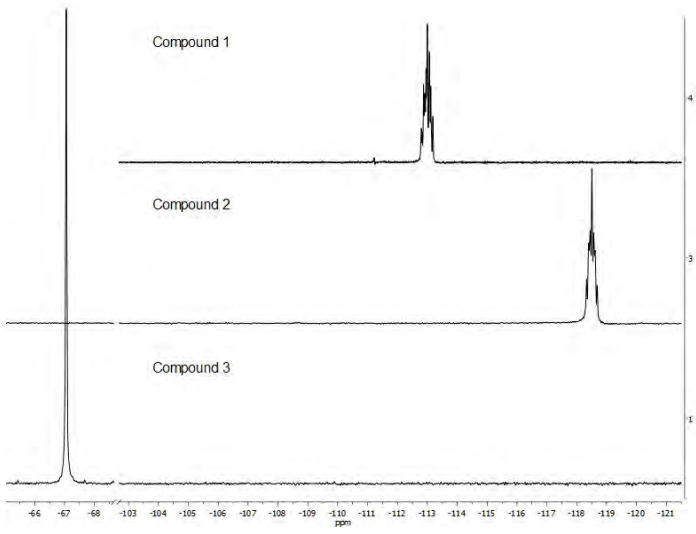

Figure 2: Full ^{19}F NMR spectra of, from top down, fluorobenzene (compound 1), 4-fluorobenzyl bromide (compound 2), and [4-(trifluoromethyl)phenyl]methanamine (compound 3).

Note that *J* coupling is indirect, through-bond scalar coupling between nuclei of like spin. The superscripts preceding the *J* term, e.g., ^{2}J, ^{3}J, or ^{4}J, indicate the number of bonds separating the coupled nuclei. ^{3}J coupling is most commonly observed in ^{1}H NMR, whereas with ^{19}F NMR, coupling 2-6 bonds away is routinely observed. The subscripts, e.g., J_{HH}, J_{FH}, or J_{FF}, indicate which nuclei are coupled. Coupling constants provide valuable information on which nuclei are close to one another. Coupled nuclei split the signal intensity of an otherwise uncoupled nuclei, resulting in a multiplet signal. The multiplicity, following the n+1 rule for first-order coupling, signifies the number of adjacent coupled nuclei, n.

An example of a fluorotelomer

Fluorotelomers are fluorocarbon-based oligomers synthesized by radical polymerization. They are used in a variety of manufacturing processes as flame retardants, and as non-conductive coatings due to their lipophobicity. Fluorotelomers are also the basis of many environmentally persistent perfluorinated carboxylic acids because of their use as surfactants.

The compound perfluoro-n-butyl ethylene is a fluorotelomer intermediate sold under the trade name Zonyl® PFBE. It has an ethylene functional group and fluorocarbon backbone. The higher spectral resolution of the fluorine peaks makes multiplet analysis and structural determination facile (Figure 3).

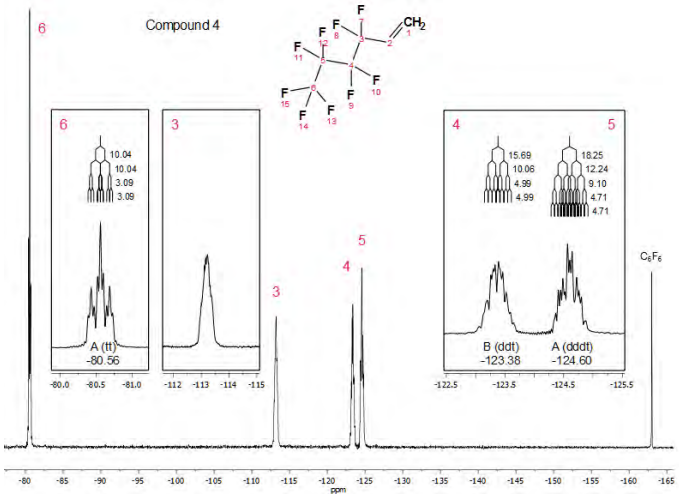

Figure 3: Full ^{19}F NMR spectrum of perfluoro-n-butyl ethylene. Inset: Multiplet analysis of the splitting pattern of individual peaks, with a *J*-coupling tree and coupling constants overlaid on the spectrum.

The insets show the *J*-coupling trees for the peaks of well-defined multiplicity (peaks 4, 5, and 6). The magnitude of the $^{3}J_{FF}$ coupling constants are of the expected size for linear, symmetric primary and secondary fluoroalkyl groups. For peak 3, the coupling of fluorine atoms to adjacent protons ($^{3}J_{FH}$) at position C_3 disrupts the symmetry at this position, causing the loss of a well-defined multiplet.

An example of a hydrofluorocarbon

Hydrofluorocarbon (HFC) electronic fluids are used in a variety of applications, such as heat transfer fluids, lubricants, and in precision and optics cleaning. Figures 4 and 5 are the ^{1}H and ^{19}F spectra, respectively of 2H,3H-decafluoropentane, a specialty fluid sold by DuPont™ under the trade name Vertrel® XF.

In the ^{1}H spectrum (Figure 4), in addition to the H-H coupling $^{3}J_{HH}$, both protons experience strong ^{1}H-^{19}F geminal coupling ($^{2}J_{FH}$; coupling of spin ½ nuclei attached to the same carbon center) to fluorine, and vicinal coupling ($^{3}J_{FH}$; coupling of spin ½ nuclei on adjacent carbon centers) to adjacent fluorine atoms, yielding a complex multiplet splitting pattern. The complexity is further compounded by the asymmetry of proton substitution at the C_2 and C_3 positions and slightly different chemical shifts for the two protons. Multiplet analysis of the splitting pattern suggests a *dddd* class, with a $^{2}J_{FH}$ coupling constant of 43.4 Hz.

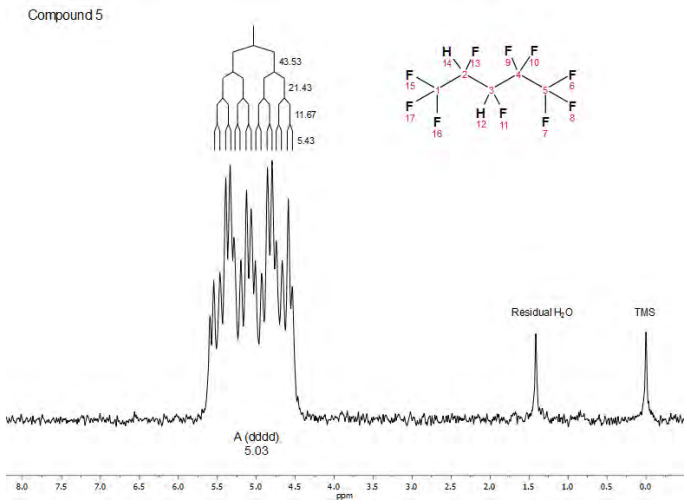

Figure 4: Full ^{1}H NMR spectrum of 2H,3H-decafluoropentane ($C_5H_2F_{10}$; neat) with TMS added as a chemical shift reference. Multiplet analysis of the splitting pattern reveals a *dddd* class; a *J*-coupling tree and coupling constants are overlaid on the spectrum.

In the ^{19}F spectrum (Figure 5), primary and secondary alkyl fluorides experience vastly different shielding along the carbon backbone, spanning a range from -220 ppm to -75 ppm, allowing for the analysis of individual fluorine groups separately. Confirmation of the strong geminal $^{2}J_{FH}$ coupling observed in the ^{1}H spectrum is in the multiplet analysis of the splitting pattern of fluorine atoms at positions C_2 and C_3 (inset for peaks 2 and 3).

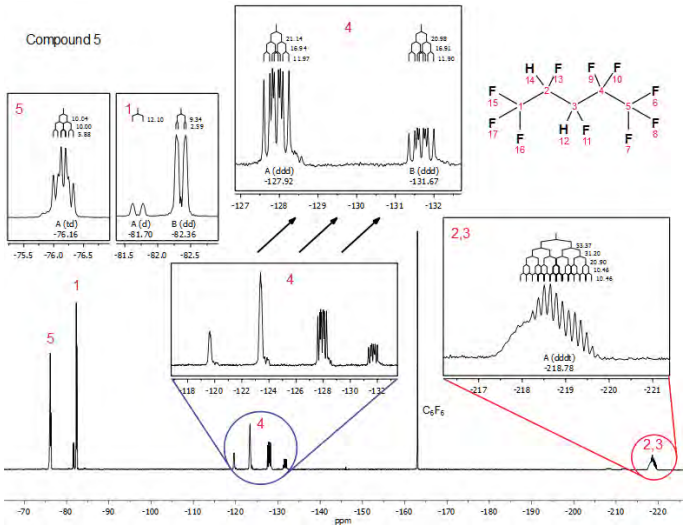

Figure 5: Full ^{19}F NMR spectrum of 2H,3H-decafluoropentane ($C_5H_2F_{10}$; neat) with C_6F_6 added as a chemical shift reference. Inset: Expanded view of chemical shift regions showing complex, multiplet splitting patterns arising from $^{2}J_{FH}$ and $^{3}J_{FH}$ coupling, and molecular asymmetry. *J*-coupling trees and coupling constants are overlaid on the spectrum.

Conclusions

Fluorine-19 NMR compliments ^{1}H and ^{13}C NMR in structure determination. The broader chemical shift range in ^{19}F NMR helps resolve individual fluorine containing functional groups, while the often-large variable magnitude of ^{19}F-^{19}F and ^{1}H-^{19}F coupling provides additional insight into structural effects. First-order coupling and highly resolved resonance lines also simplify analysis. Overall, ^{19}F NMR adds a new dimension in the analysis portfolio of fluorine containing compounds.

Find out more at **www.thermofisher.com/NMR**

ThermoFisher SCIENTIFIC

AN52995_E 10/17M

thermo scientific

APPLICATION NOTE AN52301

Classification of polyethylene by Raman spectroscopy

Author

Mohammed Ibrahim, Ph.D.,
Herman He, Ph.D.,
Thermo Fisher Scientific, USA

Keywords

Polyethylene (PE), density, Raman Spectroscopy, Raman Microscopy, classification, Discriminant Analysis

Application benefits

Raman spectroscopy provides molecular level structural information, and is advantageous in classifying polyethylene (PE). Sample preparation is minimal. The method is non-destructive, and the analysis is fast (once the TQ methods are established).

Introduction

Polyethylene (PE) is one of the most common plastics in the world with annual global production of around 80 million tons.[1] Based on density, polyethylene is generally classified as high-density polyethylene (HDPE, > 0.940 g/cm^3) or low-density polyethylene (LDPE, < 0.930 g/cm^3).[2] These different density polyethylene's have vastly different physical, chemical, and mechanical properties, and hence are used in different applications. For example, HDPE is primarily used for milk jugs, detergent bottles, garbage containers, and water pipes, due to its high tensile strength; LDPE, on the other hand, has a lower tensile strength and is used mainly for plastic bags and wraps. Therefore, density is one the most important properties of polyethylene, and classifying them according to their density is essential for proper PE specification.

Bulk PEs are manufactured as pellets (resins, granules), and later converted to other forms (such as films and pipes) using extrusion or molding processes. They are also made into multilayer films for a wide range of industrial applications like food and consumer product packaging. The density of bulk PE pellets and single-layer PE films can be measured and classified with relative ease using several standard techniques: ISO 1183-1/ASTM D792 (immersion method),[3] ISO 1183-2/ASTM D1505 (density gradient method),[4] and ASTM D4883 (ultrasound method).[5] However, all these techniques require the PE in its "pure" form, which can be challenging in the case of PE in multilayer films. Extensive sample preparations (microtoming, separation of layers by dissolving in solvents) are often required[6] to isolate the PE layer before analysis, which can be labor-intensive and time-consuming.

ThermoFisher SCIENTIFIC

Raman spectroscopy is sensitive to changes in the molecular structure level of PE, such as the degree of crystallinity, which is the key determining factor of PE density.[7,8] More importantly, the confocal capability of Raman microscopy allows for facile *in situ* analysis of individual PE layers in multilayer films without the need to isolate the PE layer. To our best knowledge, PE density measurement using Raman has been limited to PE pellets.[7,8] In this work, we want to systematically explore the feasibility of using confocal Raman microscopy for PE film density analysis, both qualitatively and quantitatively. We demonstrate that Raman microscopy in combination with the discriminant analysis method can be successfully applied to distinguish HDPE and LDPE in both pellet and film forms. In a subsequent application note, we will detail the quantitative determination of PE density using a confocal Raman microscope.

Experimental

Sample description

A total of 16 PE samples (10 pellets and 6 films) with known densities were used for the classification studies. All samples were used as received.

Method conditions

A Thermo Scientific™ DXR2™ Raman Microscope was used for the collection of Raman data. For each type/class of the pellet samples, Raman spectra were collected from 3 different pellets and averaged. For each film sample, Raman spectra were collected from 3-4 locations across the surface of the sample. An averaged spectrum was then used for final analysis.

A 532 nm laser was used with a 2 mW laser power at the sample. A 10x objective and a 50 µm slit aperture were used to obtain more representative spectra from the samples. Total acquisition time for each spectrum was 30 seconds (3 second exposure x 10 exposures). Thermo Scientific™ OMNIC™ software was used for operation of the DXR2 Raman Microscope, and collection of Raman spectra; Thermo Scientific™ TQ Analyst™ software was used for chemometric analysis of the Raman data.

Results and discussion

Raman spectra

Representative Raman spectra of HDPE and LDPE samples, in both pellet and film forms, are shown in Figure 1. There are noticeable differences between HDPE and LDPE spectra, for both pellets and films. In the CH_2 bending and the CH_2 twisting region, the intensity of the CH_2 bending mode at 1416 cm^{-1} (relative to the CH_2 bending mode at 1440 cm^{-1}) is higher for HDPE than for LDPE. This observation agrees with the previous reports that the 1416 cm^{-1} and 1440 cm^{-1} peaks are indicators of crystalline and amorphous PE phases, respectively.[7-10] The higher the degree of crystallinity, the higher the density. The differences between HDPE and LDPE are also pronounced in the C-H stretching region. The intensity of the symmetric CH_2 stretching mode at 2848 cm^{-1} (relative to the asymmetric CH_2 stretching mode at 2882 cm^{-1}) appears to be higher for LDPE compared to HDPE. Since the C-H stretching (2825-2970 cm^{-1}) and the CH_2 bending regions (1398-1470 cm^{-1}) are sensitive to the density of PE, these regions were selected for subsequent discriminant analysis.

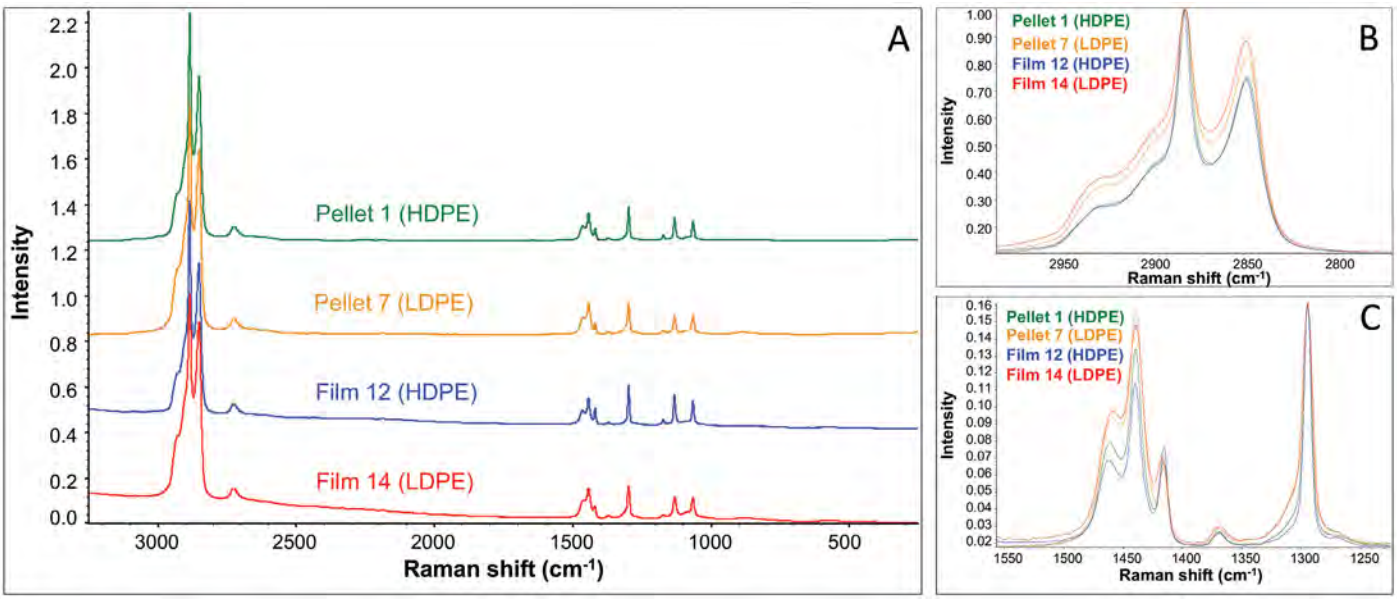

Figure 1: Representative Raman spectra of HDPE and LDPE pellets and films. (A) Full spectral range. (B) C-H stretching region. (C) CH_2 bending and CH_2 twisting region.

Data processing

The raw Raman spectra were processed using Norris 2nd derivative, and the resulting spectra were further processed by standard normal variate (SNV). Examples of the data processing are shown in Figure 2.

Norris derivative is effective in removing background drift in Raman spectra caused by fluorescence, whereas SNV is effective in compensating such variations as sample surfaces and laser penetration depths.[11-12]

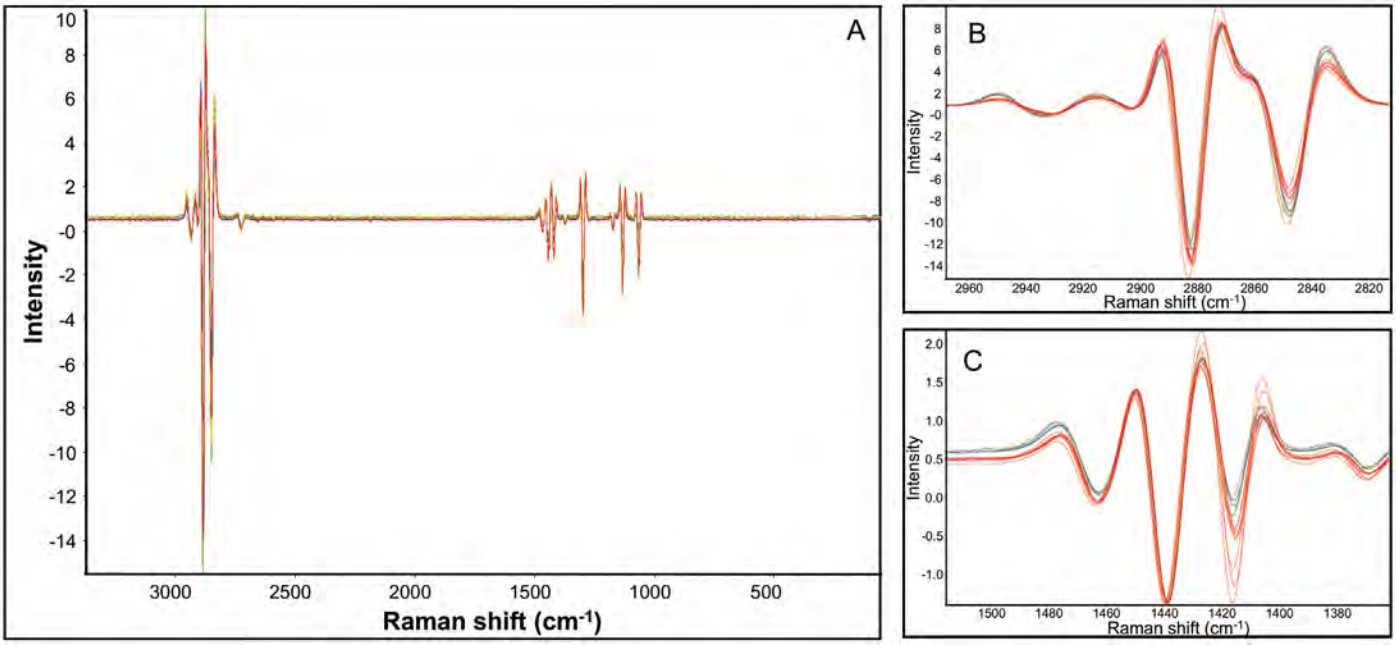

Figure 2: Norris 2nd Derivative and SNV processed sample spectra. (A) Full spectral range. (B) C-H stretching region. (C) CH_2 bending region. HDPE spectra are in red in both B and C Plots.

Classification of PE by discriminant analysis

				Calibration results		
	PE sample	Actual class	Usage	Calculated class	Distance to HDPE	Distance to LDPE
Pellets	1	HDPE	Calibration	HDPE	0.89	4.23
	2	HDPE	Calibration	HDPE	0.77	4.97
	3	HDPE	Calibration	HDPE	0.67	4.05
	4	HDPE	Validation	HDPE	1.33	3.69
	5	HDPE	Calibration	HDPE	0.68	5.14
	6	HDPE	Calibration	HDPE	0.76	4.91
	7	LDPE	Calibration	LDPE	4.01	0.99
	8	LDPE	Calibration	LDPE	5.32	0.78
	9	LDPE	Validation	LDPE	3.79	0.94
	10	LDPE	Calibration	LDPE	4.71	0.77
Films	11	HDPE	Validation	HDPE	1.23	4.79
	12	HDPE	Calibration	HDPE	1.24	4.66
	13	HDPE	Calibration	HDPE	1.30	4.93
	14	LDPE	Validation	LDPE	4.97	0.84
	15	LDPE	Calibration	LDPE	4.84	0.57
	16	LDPE	Calibration	LDPE	4.54	1.19

Table 1: PE sample class types and calibration results

The discriminant analysis classification method with principal component analysis (PCA) algorithm[13] from the TQ Analyst software package was applied to distinguish HDPE vs. LDPE. A total of 12 samples, a mix of pellets and films, were used as the calibration standards. Four additional samples (one HDPE pellet, one HDPE film, one LDPE pellet, and one LDPE film) were selected as the validation standards (Table 1).

PCA derives the principal components (PC) or the significant spectral information from the spectral variance of the calibration sample set. The number of significant PCs represents the number of independent variables affecting spectral responses, including but not limited to: concentration, impurities, opaqueness, and sample color. Scores of PCs depict the projected sample spectrum in the principal component domain. The PCA-based classification method then calculates the Mahalanobis (M) distance, defined by the distance between the sample and the center of each cluster in the PC domain. The sample is classified as belonging to a class if $M < 3$, and rejected from a class if $M > 3$.

Number of PCs	Cumulative Variance%
0	0
1	80.96
2	98.03
3	98.83
4	99.46
5	99.74

Table 2: Impact of number of PCs on variance coverage

The number of PCs has a direct impact on the robustness of the discriminant analysis. As shown in Table 2, the first several principal components represent the majority of the spectral variation. Five PCA factors, accounting for 99.7% of the total spectral variance, were used in this classification model.

Figure 3 is a 3-D plot of PCA Clusters of HDPE and LDPE. The HDPE samples (red) and LDPE (blue) samples are located on the opposite ends of the cube. Notwithstanding PC1 accounting for ~81% of the total spectral variation in the data set, the separation between HDPE and LDPE is mainly in the PC2 dimension. In the current case, the PC2 dimension seems to be closely correlated to the PE density. Figure 4 shows the cross-validation results of the 16 samples, the M distance to its own class vs. the M distance to the other class. The average M distance for each sample to its own class was about 1, but the average distance to the other class is over 4, as listed in Table 1. For both sample classes (HDPE and LDPE), there is no separation between pellets and films, suggesting the sample form (pellet vs. film) has little, if any, impact on the methodology.

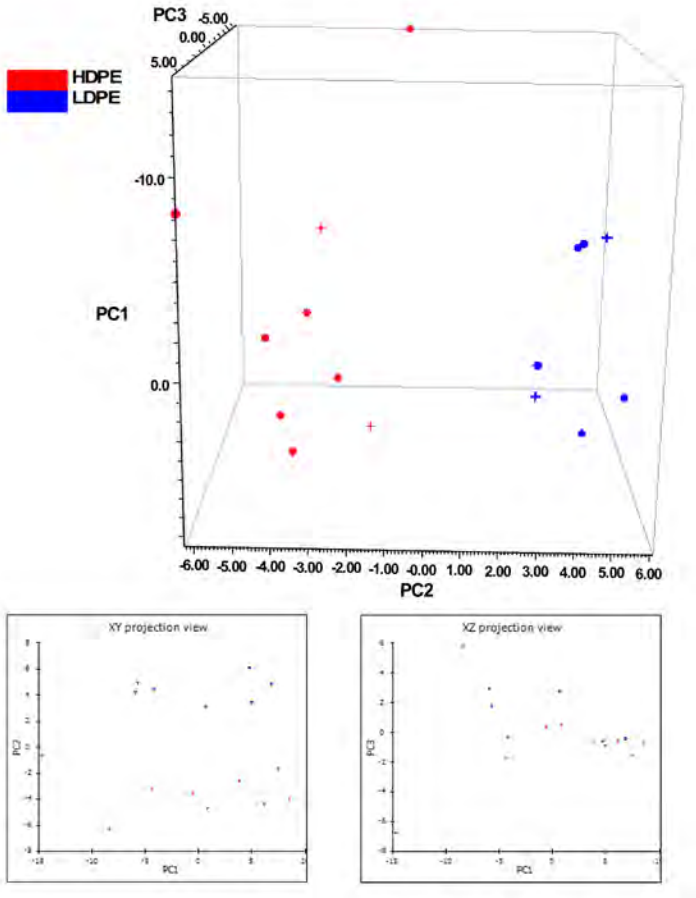

Figure 3: 3-D cluster plot of HDPE and LDPE samples. The • are the calibration samples, and the + are the validation samples.

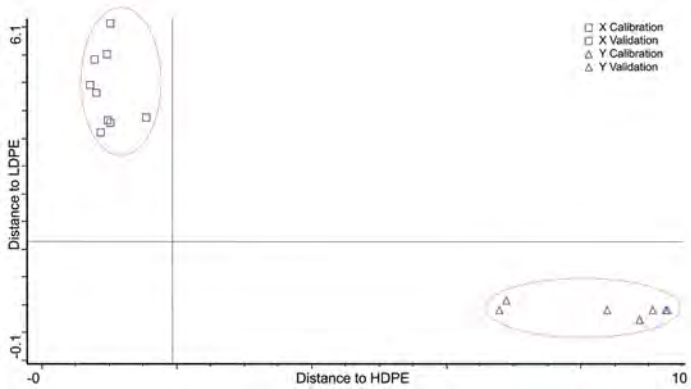

Figure 4: TQ Analyst software discriminant analysis calibration output for PEs with different densities. The two different types of PEs: HDPE and LDPE are clearly separated, and correctly classified. The calibration results are also shown in Table 1.

The Raman spectrum of a previously unused pellet sample with known density was used to test the established discriminant method, and the result is shown in Figure 5. The sample was successfully classified as HDPE with an M value of 0.68.

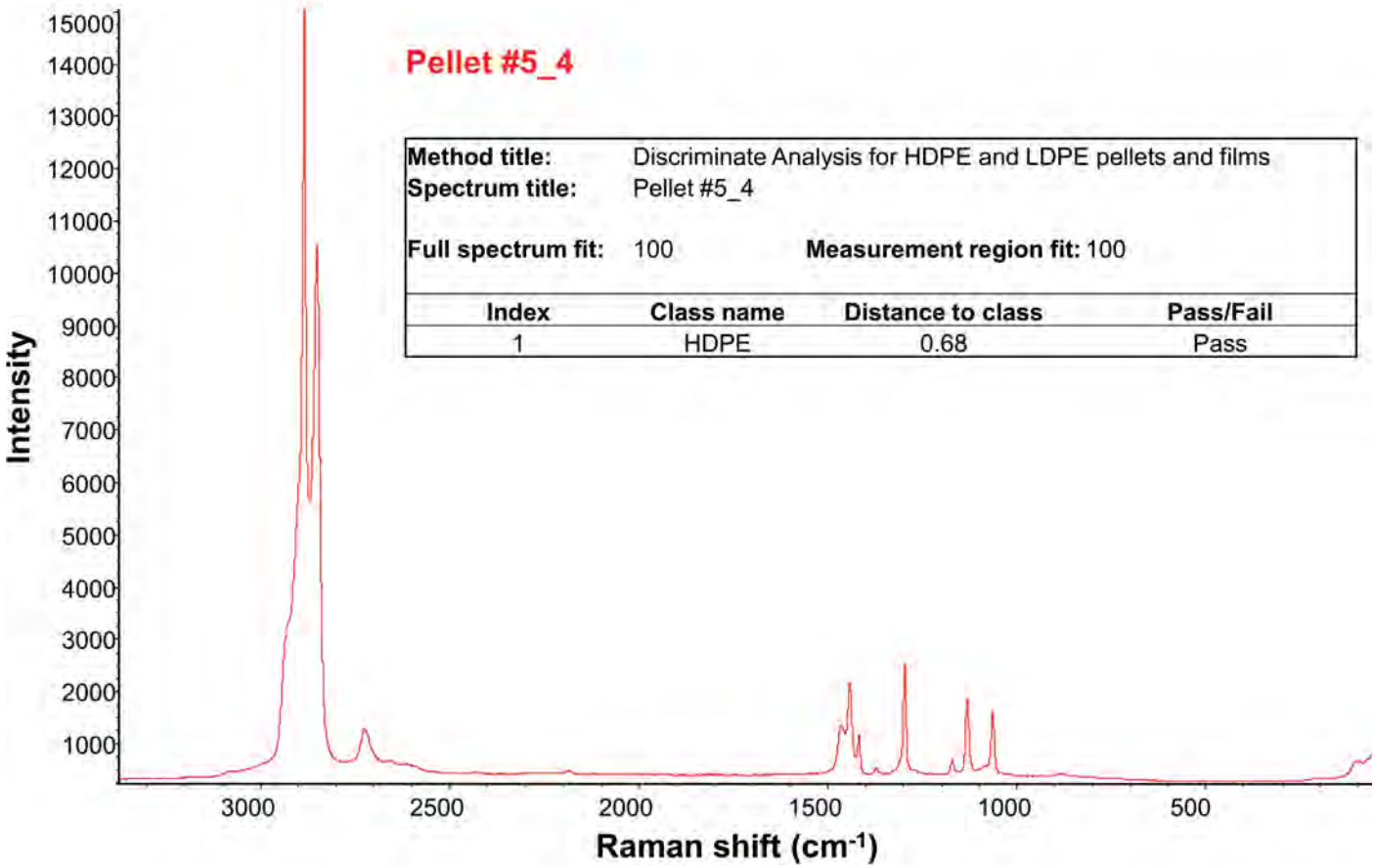

Figure 5: Classification of a PE sample by using its Raman spectrum and the discriminant method created by the TQ Analyst software.

Conclusions

In this application note, we have successfully demonstrated the use of a Thermo Scientific DXR2 Raman Microscope, in combination with the TQ Analyst software, to classify polyethylene's of different density classes in both pellet and film forms. Raman spectroscopy is non-destructive and requires minimal sample preparation. The classification method was created solely based on the Raman spectral features of LDPE and HDPE and was indifferent to the sample forms. Once the method is established, PE samples, pellets or films, can be correctly classified within minutes. Moreover, this work expands the scope of the previously reported study on PE pellets to include PE films, which broadens its applicability in the plastic/polymer industry as well as many downstream industries. The described methodology should be applicable for *in situ* classification of thin PE layer(s) in multilayer films.

Thermo Scientific DXR2 Raman Microscope

References

1. Piringer O.G. and Baner A.L., *ed. Plastic Packaging: Interactions with Food and Pharmaceuticals.* 2nd ed. Weinheim: Wiley-VCH; 2008.
2. Polyethylene, The Essential Chemical Industry - online, http://www.essentialchemicalindustry.org/polymers/polyethene.html, retrieved on 9/10/2017.
3. (a) ISO 1183-1:2012, *Plastics – Methods for determining the density of non-cellular plastics – Part 1: Immersion method, liquid pyknometer method and titration method*; ANSI New York, NY. (b) ASTM D792-13, *Standard test methods for density and specific gravity (relative density) of plastics by displacement*; ASTM International, West Conshohocken, PA, 2013.
4. (a) ISO 1183-2:2004, Plastics — *Methods for determining the density of non-cellular plastics — Part 2: Density gradient column method.* (b)ASTM D1505-10, *Standard test method for density of plastics by the density-gradient technique*; ASTM International, West Conshohocken, PA, 2010.
5. ASTM D4883-08, *Standard test method for density of polyethylene by the ultrasound technique;* ASTM International, West Conshohocken, PA, 2008.
6. Mieth A., Hoekstra E., and Simoneau C. *Guidance for the identification of polymers in multilayer films used in food contact materials: User guide of selected practices to determine the nature of layers,* EUR 27816 EN, 2016; doi: 10.2788/10593.
7. Strobl G.R. and Hagedorn W. *Raman spectroscopic method for determining the crystallinity of polyethylene,* J. Polym. Sci. B Polym. Phys., 1978, 16, 1181-1193.
8. Sato H., Shimoyama M., Kamiya T., Amari T., Sasic S., Ninomiya T., Siesler H.W., and Ozaki Y. *Raman spectra of high-density, low-density, and linear low-density polyethylene pellets and prediction of their physical properties by multivariate data analysis,* J. Appl. Polym. Sci., 2002, 86, 443–448.
9. Migler K.B., Kotula A.P., Hight Walker A.R. *Trans-rich structures in early stage crystallization of polyethylene,* Macromolecules, 2015, 48, 4555–4561.
10. Kida T., Hiejima Y., and Nitta K-H. *Raman spectroscopic study of high-density polyethylene during tensile deformation*, Int. J. Exp. Spectroscopic Tech., 2016, 1:001.
11. Simone, E., Saleemi A.N., and Nagy Z.K. *Application of quantitative Raman spectroscopy for the monitoring of polymorphic transformation in crystallization processes using a good calibration practice procedure,* Chem. Eng. Res. Des. 2014, 92, 594–611.
12. Huang J., Romero-Torres S., and Moshgbar M. *Practical considerations in data pre-treatment for NIR and Raman spectroscopy,* Am. Pharm. Rev. 2010, 13 (6).
13. Thermo Scientific Product Overview. *TQ Analyst Software Chemometric Algorithms,* 2009.

Find out more at **www.thermofisher.com/Raman**

ThermoFisher SCIENTIFIC

thermo scientific

APPLICATION NOTE AN52304

FT-Raman: an invaluable addition to the forensic arsenal to combat the opioid epidemic

Authors

Suja Sukumaran, Ph.D.[1]
Rui Chen, Ph.D.[1]
Shea A Schleman[2]
Laura J Bell[2]
[1]Thermo Fisher Scientific, USA
[2]Albuquerque Police Department, Albuquerque, New Mexico

Introduction

Illicitly manufactured fentanyl is becoming a major driver of opioid overdose. According to the Centers for Disease Control and Prevention (CDC), illegal, lab-made fentanyl was involved in more than 50% of opioid overdose deaths in 2016.[1] The growing opioid epidemic presents multifaceted challenges for law enforcement, first responders, and forensic lab personnel. In particular, the high potency of fentanyl and fentanyl analogues makes accidental exposure life-threatening, with ingestion, inhalation, and absorption through the skin as possible exposure routes. With a lethal dose of only a few milligrams, fentanyl is considered 50-100 times more potent than morphine. Carfentanil, a fentanyl analogue, is approximately 100 times more potent than fentanyl. Consequently, the CDC has issued a health alert on the rise of unintentional overdoses of clandestinely produced and trafficked fentanyl in the form of counterfeit pills and heroin adulterants.[1-2] The situation is further exacerbated by the waves of new synthetic opiates. Through chemical modification, new potent fentanyl analogues are created at a fast pace in underground labs, keeping authorities constantly on their toes to identify these emerging chemical entities and to understand their pharmacology and toxicology.

The challenges in the detection, identification, and screening of synthetic opioids mandate the use of multiple analytical techniques and instrumentation, both field-deployable and laboratory-based, in a concerted and holistic manner. For example, The CDC advises two-tiered testing, an enzyme-linked immunosorbent assay (ELISA) screen followed by gas chromatography/mass spectrometry (GC/MS) to identify the fentanyl compound in blood and urine in the cases of suspected overdose. In the meantime, liquid chromatography / mass spectrometry (LC/MS), LC/MS/MS, ion mobility spectrometry (IMS), and thermal desorption direct analysis in real time mass spectrometry (TD-DART-MS) are being explored to meet the demand on low detection limit for many case samples where fentanyl is present with other drugs and cutting agents at low concentration.[2]

ThermoFisher SCIENTIFIC

Raman spectroscopy has long been used for the detection and identification of illicit drugs and adulterants, and offers a valuable addition to the forensic toolbox for the analysis of fentanyl and fentanyl analogues. FT-Raman utilizes a long-wavelength laser (1064 nm) which greatly reduces fluorescence and produces high signal-to-noise spectra, making it well suited for many narcotic samples that fluoresce. It also enables sampling through glass vials, polymer blister packs, and plastic evidence bags; hence, often requires little to no sample preparation. It is nondestructive and allows the custody chain to be maintained, given the possibility of qualitative and quantitative evaluation of the sample to confirm its integrity from its seizure until the sample is placed in the evidence file.[3]

In this application note, analyses of fentanyl as well as other illicit drugs using FT-Raman spectroscopy are presented. The advantages of FT-Raman for the detection and identification of illicit drugs are also discussed.

Materials and methods

All samples analyzed in this study were prepared at Albuquerque Police department. Samples were analyzed in double bags, blister packs or glass vials, and handled in compliance with Schedule I controlled substance handling protocols. A Thermo Scientific™ Nicolet™ iS50 FT-IR spectrometer equipped with a calcium fluoride beam splitter and an FT-Raman module with a 1064 nm laser was used for all analyses (Figure 1). A total of 64 scans were co-added for each spectrum at 8 cm-1 resolution, with a total acquisition time of ~75s. The laser power was set at 0.5 mW. The spectra were searched against Thermo Scientific Law Enforcement and Security (LEnS) Raman and DEA Raman libraries using OMNIC library search and Specta multicomponent search options.

Figure 1: An iS50 Raman module for the Thermo Scientific Nicolet iS50 FT-IR spectrometer.

Results and discussion

Figure 2A shows the Raman spectrum of bulk fentanyl in a double bag, directly acquired without any sample manipulation. Since the laser spot size is approximately 60 µm, small quantity of samples, such as a few granules, can be analyzed with ease. An example is shown in Figure 2B. While Figure 2B exhibits a slightly higher noise level compared to Figure 2A, both samples were nonetheless positively identified as fentanyl citrate through library search.

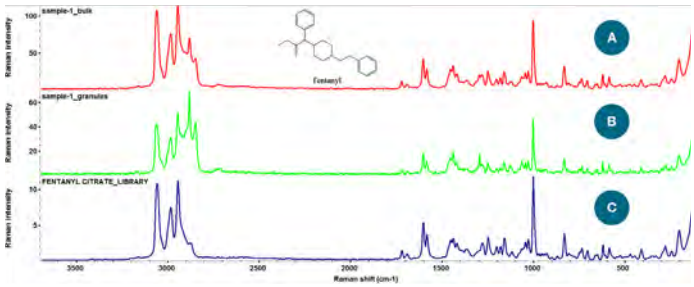

Figure 2: Raman spectra of (A) seized bulk fentanyl in a double-bag; (B) a few fentanyl granules in a double-bag; and (C) fentanyl citrate from DEA Raman library.

Raman spectroscopy is sensitive to both chemical and physical properties. Its unique selection rules generate a molecular fingerprint that is well suited to the differentiation between many illicit drug compounds and their analogues. Figure 3 shows the Raman spectra of a tablet as well as the 3,4-methylenedioxyamphetamine (MDA) and 3,4-methylenedioxymethamphetamine (MDMA) standards from the library. Despite the minute structural difference between MDA and MDMA (inset of Figure 3), Raman spectroscopy can unambiguously distinguish the two. In this case, the tablet was identified as MDA with a match score of 83, as opposed to a match score of 66 for MDMA.

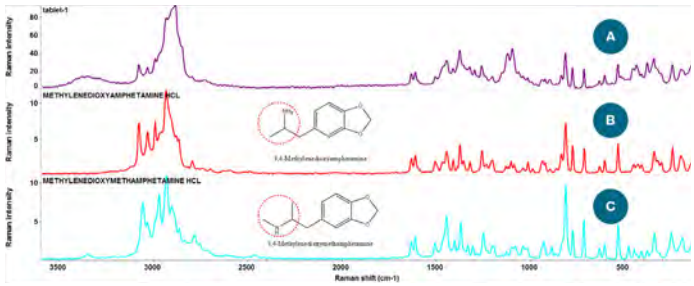

Figure 3: Raman spectra of (A) a tablet; (B) 3,4-methylenedioxyamphetamine (MDA) standard from the library; and (C) 3,4-methylenedioxymethamphetamine (MDMA) standard from the library.

Seized street drugs are often present in the form of mixtures. Figure 4 shows the Raman spectrum of an off-white powder sample in an evidence bag. Initial library search showed similar match score for lactose and cocaine, suggesting that the sample contains multiple components. The spectrum was then subjected to the OMNIC Specta multi-component search, and the sample was identified as a mixture of cocaine and β-D-lactose, a commonly used cutting agent.

Conclusions

The Nicolet iS50 FT-IR spectrometer equipped with the iS50 Raman module offers an invaluable tool for the forensics labs to combat the growing opioid epidemic. Raman analysis requires little to no sample preparation and allows for direct measurements through glass vials and evidence bags, greatly reducing the risk of lab personnel's accidental exposure to high potency drugs such as fentanyl and fentanyl analogues. While the measurement of bulk narcotic samples is fast and straightforward, with a laser spot size of 60 µm, acquisition of high quality Raman spectra from as little as few granules is also possible. Combined with DEA and LEnS Raman libraries, OMNIC Specta enables identification of multi-component illicit drugs with confidence. Raman spectroscopy using the iS50 Raman module is a safe, fast, and complementary technique for the screening, detection and identification of illicit drugs.

References

1. https://www.cdc.gov/drugoverdose/opioids/fentanyl.html
2. Edward Sisco, Jennifer Verkouteren, Jessica Staymates, Jeffrey Lawrence, Forensic Chemistry, Volume 4, June 2017, Pages 108-115,
3. Ciro Augusto Fernandes de Oliveira Penido, Marcos Tadeu Tavares Pacheco, Igor K. Lednev, Landulfo Silveira Jr., Journal of Raman Spectoscopy, 47 (1), January 2016, Pages 28–38.

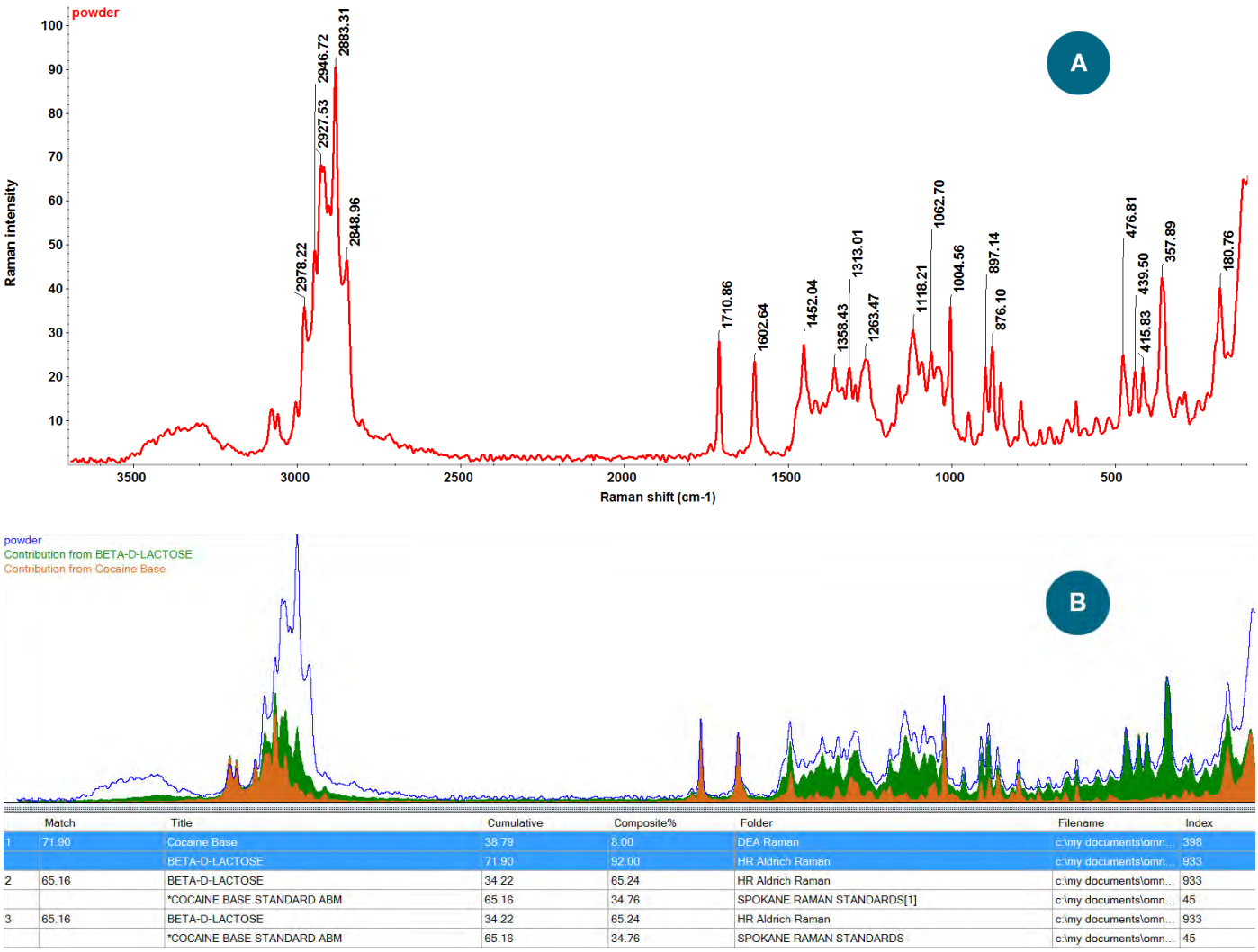

	Match	Title	Cumulative	Composite%	Folder	Filename	Index
1	71.90	Cocaine Base	38.79	8.00	DEA Raman	c:\my documents\omn...	398
		BETA-D-LACTOSE	71.90	92.00	HR Aldrich Raman	c:\my documents\omn...	933
2	65.16	BETA-D-LACTOSE	34.22	65.24	HR Aldrich Raman	c:\my documents\omn...	933
		*COCAINE BASE STANDARD ABM	65.16	34.76	SPOKANE RAMAN STANDARDS[1]	c:\my documents\omn...	45
3	65.16	BETA-D-LACTOSE	34.22	65.24	HR Aldrich Raman	c:\my documents\omn...	933
		*COCAINE BASE STANDARD ABM	65.16	34.76	SPOKANE RAMAN STANDARDS	c:\my documents\omn...	45

Figure 4: Raman spectra of a seized street drug sample containing cocaine and β-D-lactose.

Find out more at **thermofisher.com/is50**

thermo scientific

APPLICATION NOTE AN52326

Leveraging the lateral spatial resolution of a confocal Raman microscope to resolve micron to sub-micron layers in polymer laminates

Author

Mohammed Ibrahim, Ph.D. and Rui Chen, Ph.D.
Thermo Fisher Scientific, Madison, WI

Keywords

laminates, polymer, confocal Raman microscope, spatial resolution

Application benefits

With a properly configured Thermo Scientific™ DXR™2 Raman microscope, it was possible to resolve a thin polymer layer with a thickness (≈0.4 µm) that's very close to the theoretical spatial resolution limit.

Thermo Fisher Scientific solutions

- DXR2 Raman microscope
- Thermo Scientific™ OMNIC™ for Dispersive Raman software suite

Introduction

Polymer laminates are used in a wide range of industries from food to pharmaceuticals. By adhering together multiple polymeric layers of different chemistry, physical properties, and thickness, desired chemical, mechanical and barrier properties can be achieved to suit different packaging applications. As the technological advancement and manufacturing sophistication continue to drive the production of more complex and thinner laminate structures, there is an ever-increasing demand on laminate analysis for product quality control, failure analysis, and competitive reverse engineering.

The analytical tools for laminate analysis include optical microscopy, differential scanning calorimetry (DSC), Fourier Transform infrared spectroscopy (FT-IR), and Raman spectroscopy. Confocal Raman microscopy, in particular, offers many advantages. Raman spectroscopy is sensitive to both chemical and physical properties. Its unique selection rules generate a molecular fingerprint that is well suited to material identification. Confocal Raman microscopy often utilizes short-wavelength visible and NIR (400 – 785 nm) lasers for sample excitation, which renders increased sensitivity because Raman signal intensity is inversely proportional to the 4th power of the laser wavelength. Furthermore, the spatial resolution is also inversely proportional to the laser wavelength. The shorter the wavelength, the higher the resolution.[1,2]

In this application note, two cases of polymer laminate analysis using a Thermo Scientific DXR2 Raman Microscope are presented. The implications of instrument configurations, including laser wavelength, magnification objective, and pinhole size, on lateral spatial resolution are discussed in details.

ThermoFisher SCIENTIFIC

Materials and methods

Two polymer laminate samples, A and B, were microtomed and cut into films. The microfilms were placed onto glass slides and pentane was added to flatten the microfilms. The glass slide was then placed on the microscope stage insert for Raman mapping. A Thermo Scientific DXR2 Raman Microscope was used for all analyses. A 532 nm laser was used and the laser power was set at 5 mW. A 100× objective and a 25 µm confocal pinhole were used. The Raman line map (27.4 µm) was collected with a 0.2-µm step size and contains 138 spectra. The Raman area map (3 µm [X] x 20 µm [Y]) was collected with 1 µm (X) and 0.2 µm (Y) step sizes and contains 584 spectra. Data acquisition and processing were done by Thermo Scientific OMNIC for Dispersive Raman software suite.

Results and discussion

Identification of the layers of polymer laminates using Raman microscopy can be done by confocal depth profiling and cross-section analysis. While depth profiling is advantageous in that it requires little to no sample preparation, cross-section analysis via line/area mapping offers superior spatial resolution, which lends itself to the identification of micron to sub-micron layers in polymer laminates.

Figure 1A shows the video image of microfilm A and the location where the Raman line mapping was performed (red line). The corresponding Raman line map is shown in Figure 1B. The Raman line map is displayed in a 2-D contour plot and reveals the compositional changes across different layers (*y*-direction). The rainbow color scheme of the contour plot reflects the intensity of the Raman peaks, with red indicating the highest intensity and blue the lowest. Based on the Raman spectral changes in the vertical direction, seven distinct layers were identified by library search: the layers 1, 3, 5 and 7 are polyethylene (PE), the layers 2 and 6 are polypropylene (PP), and the layer 4 is polyvinyl alcohol (PVA). The representative Raman spectra for those layers are shown in Figure 1C. No cross-contamination between the adjacent layers was observed, demonstrating an adequate spatial resolution to distinguish adjacent layers. The thickness of the thinnest layer (Layer 4) was estimated to be 1.2 µm based on the full width at half maximum (FWHM) method (Figure 1D).[3]

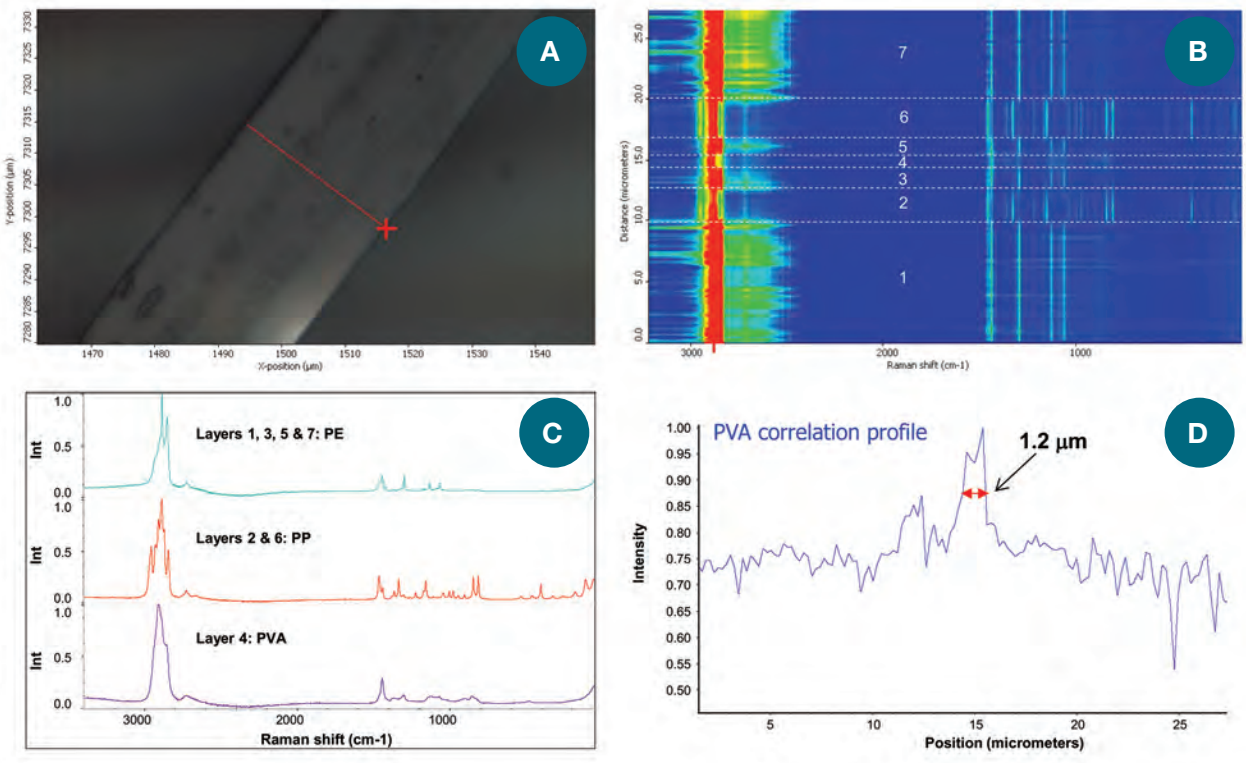

Figure 1. (A) Video image of microfilm A showing the region where Raman line mapping was performed (red line); (B) Raman line map of microfilm A; (C) representative Raman spectra of each layer. PE = polyethylene, PP = polypropylene, PVA = poly vinyl alcohol; and (D) Raman correlation profile obtained using a PVA reference spectrum.

Figure 2A-2C shows the 3-D Raman area images of microfilm B. PE, PP and PVA spectra were carefully selected from the map as the references to construct the Raman area images with correlation profiling. The red color indicates a high correlation with the reference material and the blue color indicates low correlation. Similar to microfilm A, seven layers are clearly identified: the layers 1, 3, 5 and 7 are PE, the layers 2 and 6 are PP, and the layer 4 at the center is PVA. In order to estimate the layer 4 thickness, a line map was first extracted from the area map, delineated by the white, dashed line in Figure 2C. The extracted line was then subject to correlation profiling using a PVA spectrum from the map as the reference, and the result is shown in Figure 2D. The sharp peak at ~ 14.5 µm corresponds to the layer 4, with an estimated thickness of ~ 0.4 µm based on the FWHM of the profile peak.[3] It's important to note that the methodology described above relies heavily on the quality of the spectra as well as the spectral differences between adjacent layers. The layer thickness derived from the correlation profile should therefore be considered an estimate. Precise measurement of layer thickness requires such technique as scanning electron microscopy (SEM).

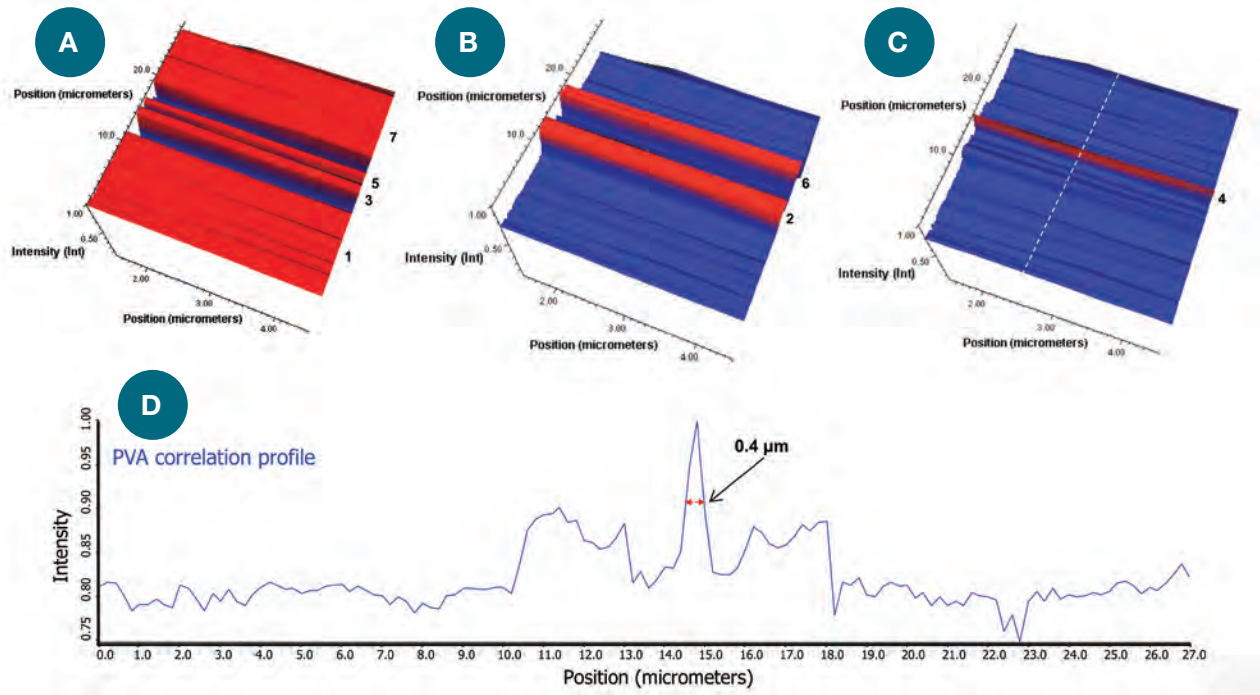

Figure 2. 3-D Raman correlation images for microfilm B. (A)-(C): Raman correlation images for PE, PP, and PVA, respectively. (D) Raman correlation profile obtained using a PVA reference spectrum on a line extracted from the area map (white dashed line on C).

Diffraction-limited resolution in optical microscopy is often empirically assessed by the Rayleigh criterion shown below, where *d* denotes the Rayleigh criterion, λ is the laser wavelength, η is the refractive index of the immersion/mounting media, and *N.A.* is the microscope objective numerical aperture.

Rayleigh Criterion

x, y plane (lateral): $d = 0.61\frac{\lambda}{N.A.}$

z-axis (axial): $d = \frac{2\lambda\eta}{(N.A.)^2}$

As indicated in the equations, both lateral and axial Rayleigh criteria are directly proportional to the wavelength, but inversely proportional to the objective numerical aperture. In addition, the axial Rayleigh criterion is proportional to the refractive index of the material under investigation. For any sample that is optically denser than air, the axial resolution is usually 4-6 times lower the lateral one. For a 532 nm laser and a 100× objective (*N.A.* = 0.90), assuming the refraction index 1.5 for the laminates, the theoretical lateral spatial resolution and axial resolution are approximately 0.4 µm and 2 µm, respectively. However, many factors such as scattering of the laser/Raman photons and interaction with interfaces in the sample can reduce this resolution. Another important consideration in instrument configuration is the pinhole size. The confocal pinhole acts as a spatial filter, by allowing the Raman spectrometer to look into a smaller spatial domain than with a conventional configuration without the pinhole, attenuating the out-of-focus regions of the sample.[2] In the current study, the combination of a 532 nm laser, a 100× objective with an N.A. of 0.9, and a 25 µm confocal pinhole enabled the resolution of a 0.4 µm-thick PVA layer, approaching the theoretical limit of the lateral spatial resolution.

thermo scientific

Conclusions

In this communication, we have demonstrated the analysis of polymer laminates using Raman line and area mapping. In both cases, seven layers were identified. With a properly configured Raman microscope, it was possible to resolve a thin polymer layer with a thickness (≈0.4 µm) that's very close to the theoretical spatial resolution limit.

References

1. Guillory P., Deschaines T. Henson P, *Materials Today*, **2009**, *12(4)*, 38-39.

2. Rzhevskii A, Ibrahim M, Ramirez J, Macisaac C., *Considerations and Techniques for Optimizing Raman Spectral and Spatial Information*, Thermo Scientific White Paper 52699, **2015**.

3. Guillory P., Deschaines T., Henson P. *Confocal Raman microscopy analysis of multilayer polymer films*, Thermo Scientific Application Note 51718, **2008**.

Find out more at **www.thermofisher.com/Raman**

ThermoFisher SCIENTIFIC

APPLICATION NOTE AN52818

FT-Raman mapping of multicomponent solid dosage forms

Author
Ron Rubinovitz, Ph.D., Thermo Fisher Scientific, USA

Keywords
FT-Raman, microscopy, mapping, PCA

Thermo Fisher Scientific solutions
Thermo Scientific™ Nicolet™ iS™50 FTIR, FT-Raman module, Thermo Scientific™ OMNIC™, Atlμs™ and Specta™ software

Introduction

FT-Raman spectroscopy is a complimentary technique to mid-IR for material analysis. Compared to FTIR, FT-Raman is compatible with glass and requires minimal sample preparation. The use of a 1064 nm laser in FT-Raman effectively alleviates the fluorescence often observed when visible laser excitation is used. The combination of FT-Raman spectroscopy with mapping lends itself well for mixture analysis by providing both chemical and spatial information within a sample. However, even a moderately sized map typically contains hundreds of spectra, making the use of automated spectral analysis an important tool for the identification of multiple components. The challenge is further exacerbated by the disparity in component distribution within a mixture, especially when spectral features only occur in small sections of a map and are obscured by stronger matrix spectra. In those cases, a statistical tool such as principal component analysis (PCA) is often required for optimal analysis.

Figure 1: Nicolet iS50 FTIR spectrometer shown with the iS50 Raman accessory in the main sample compartment.

In this note, a complete workflow to identify the multiple components within an over-the-counter (OTC) drug tablet using FT-Raman mapping is described. The capability of PCA to extract additional compositional information from the measured spectra is also demonstrated.

Experimental

The cross section of an OTC bilayer tablet containing a blend of excipients and an active pharmaceutical ingredient (API) was examined in this study. Spectra were measured at 8 cm^{-1} resolution and 16 scans at each measurement point using a Nicolet iS50 FTIR spectrometer, configured with a CaF_2 beamsplitter, InGaAs detector and iS50 Raman accessory (Figure 1). The laser wavelength was 1064 nm with a spot size of approximately 50 microns and was applied at a power of 500 mW. The area mapped was approximately 2 x 3 mm at 45 microns steps (Figure 2). Analysis of spectral maps was carried out using the OMNIC Atlμs and OMNIC Specta software.

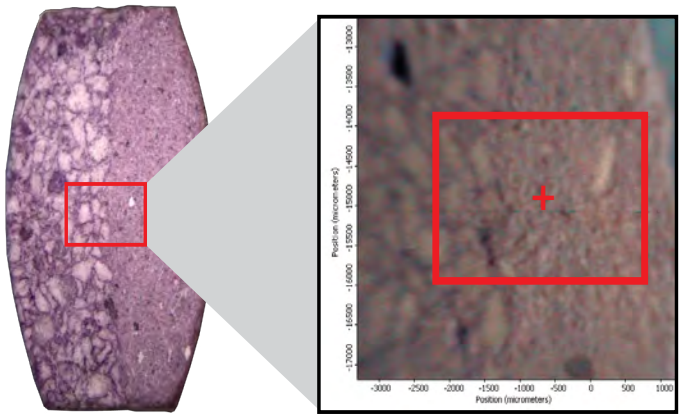

Figure 2: Cross section of tablet and area mapped.

Results and discussion

Preliminary Spectral Analysis

The area mapped consisted of three readily identifiable regions. Two layers of the tablet could be visually distinguished while the third contained white particles with an approximate dimension of 250 x 800 microns. Representative spectra from each of these regions are shown in Figure 3.

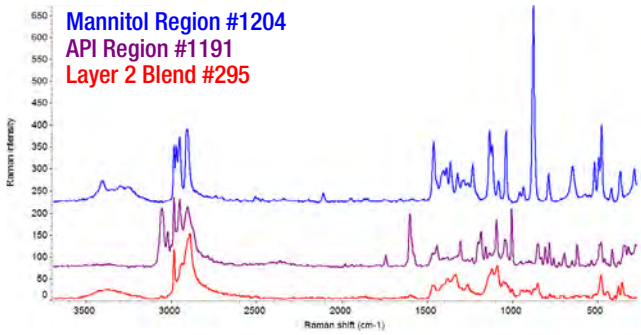

Figure 3: Representative map spectra from different regions of the tablet.

Through a library search, the spectra of the first layer yielded very high match values to mannitol. The distinct spectra from the white particles were also unequivocally assigned to the active pharmaceutical ingredient (API) of the tablet. The spectra of the second layer are matched to lactose monohydrate in the library search, but with relative low match values. Multi-component library searches were subsequently performed on the spectra from this layer (referred to henceforth as the Layer 2 Blend). The search results (Figure 4) reveal that this layer of the tablet is a blend of excipients consisting chiefly of lactose monohydrate, beta cyclodextrin and microcrystalline cellulose.

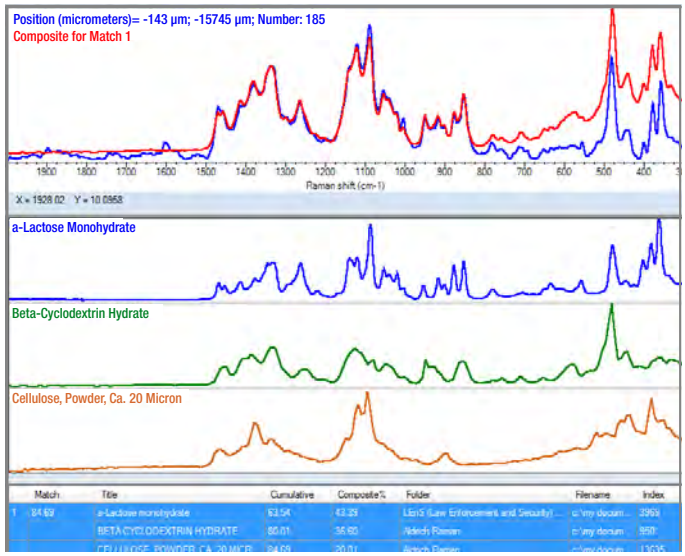

Figure 4: Multi-component search results for a spectrum from the Layer 2 Blend containing multiple excipients. The comparison of the measured spectrum to the composite library match spectrum is shown in the top of the figure, and the individual components are shown below.

Creating chemical maps

Three chemical maps were generated for the API, the Layer 2 Blend and mannitol, using 1755–1730 cm^{-1} (peak area), 1334 cm^{-1} (peak height) and 875 cm^{-1} (peak height), respectively. The results are shown in Figure 5. From these maps based on spectral features unique to each material, information on the component distribution and interdependencies can be readily visualized.

Principal component analysis

As described above, an initial inspection of the sample indicated three main spectral regions: API particles, a mannitol layer and the Layer 2 Blend. However, a PCA analysis yielded four distinct components, as summarized in Figure 6. By visual inspection and library comparison, the first three components modeled mannitol, the Layer 2 Blend and the API, respectively. The fourth component was an excellent library match to acesulfame potassium, a sugar substitute known to be used as an excipient in pharmaceutical dosage formulations. Closer evaluation of the map spectra confirmed the presence of this material in some very small regions of the map. It is also worthy to point out that the PCA analysis was able to extract an almost pure spectrum of acesulfame potassium, even though its features were heavily obscured by those from the Layer 2 Blend spectrum in the experimentally measured spectra.

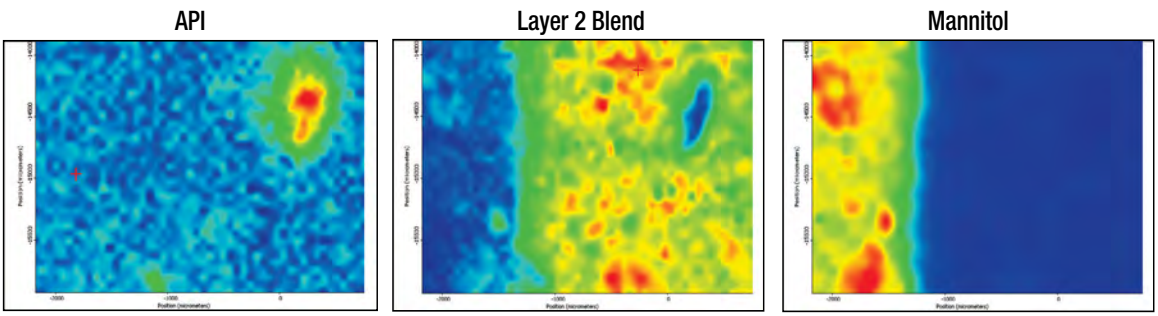

Figure 5: Maps created based on peak heights and area. High to low intensities in the maps are described by using the colors red to blue.

Conclusions

The analysis presented here demonstrates that recognition and spatial distribution of key materials in pharmaceutical dosage forms can be accomplished through FT-Raman mapping. The multi-component search method is effective in deconvoluting the spectra to yield the main components, when the measured spectra for each component have constant relative ratios, and the pure spectra of the components are available in the library. When considering a spectral map containing known components with well isolated spectral features, maps calculated from peak heights or areas are sufficient. However, as demonstrated in the case of acesulfame potassium, where a minor component occupies a very small portion of the total map area and has physical dimensions too small to permit the acquisition of a "pure" spectrum, PCA is a powerful analysis tool to detect and identify that component. The described workflow and its associated principles are applicable for comparing already-marketed drugs and providing valuable information in pre-formulation development, formulations assessment, scale-up and failure mode analysis.

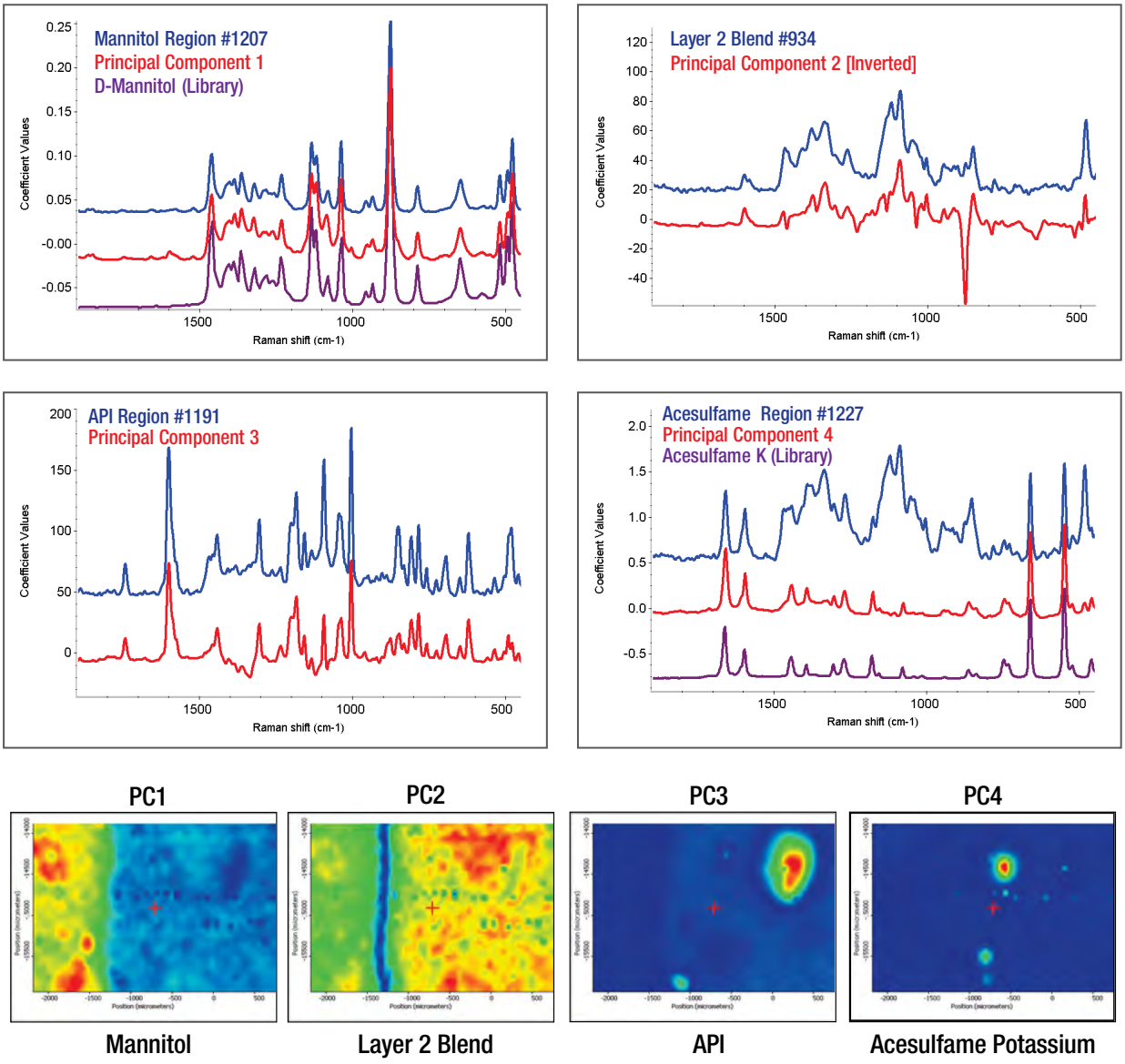

Figure 6: Top spectral plots show the spectra of the four identified components calculated by PCA: the experimentally measured Raman spectra (blue), the PCA components (red), and library spectra (magenta) when available. Maps show the distribution of each component across the measured area.

Find out more at **www.thermofisher.com/ftir**

APPLICATION NOTE

No. AN52910

Characterizing amber and its imitations with dispersive Raman spectroscopy

Author:
Alex Rzhevskii, Thermo Fisher Scientific, Madison, WI

Key words

Raman spectroscopy, Raman microscope, dispersive Raman, amber, copal, resin

Introduction

Amber is a tree resin that has been fossilized over millions of years through polymerization, cross-linking of the long carbon chain organics, and expulsion of volatiles within the resin. Amber has a wide variety of applications, ranging from its traditional use in jewelry, art and craft objects, and folk medicine, to modern applications in skin care products, perfumes, and blood conservation devices. Authentic amber is a highly demanded commodity and its high value has fostered an extensive imitation market that abounds with both natural and synthetic resins. Copal is an example of one of the natural resins that is used as an amber imitation. It is a less mature tree resin product that has not gone through the entire fossilization process and, as a result, it is less expensive than amber.

Distinguishing authentic amber from its imitations is important for scientific, commercial and personal reasons. There are several simple chemical and physical tests that can be used to authenticate amber. These tests include solubility in organic solvents, floating in salt water for testing specific gravity, assessing melting points, and even evaluating hardness using scratch tests. The main limitation of those tests arises from the possible compromise in specimen integrity, which can be prohibitive when dealing with items of artistic, archeological or historical significance. To that end, Raman spectroscopy offers an attractive solution to the identification and characterization of amber, largely due to its non-destructive sample handling.

While FT-Raman spectroscopy, in the near-infrared (1064 nm) region, has been used successfully to analyze amber[1-3] because it minimizes the substantial florescence originating from the amber resin, dispersive Raman spectroscopy has important advantages over FT-Raman. The use of lasers of shorter wavelength (e.g., 780 nm), especially, in Raman microscopy allows for sample analysis on a sub-micrometer scale and results in significantly faster spectral acquisition, because of the high laser power density developed in the small focused laser spots coupled with more effective Raman scattering that is inversely proportional to the 4th power of the laser wavelength[4]. Furthermore, confocal Raman microscopy can provide useful information about the chemical composition of the relict biomaterials and inorganic inclusions[5].

In this note, the spectra of amber and some of its common imitations obtained using a dispersive Raman spectrometer are compared and discussed.

Experimental

Samples of authentic and altered amber and its common imitations were used in this study, including: 1) Baltic amber from a contemporary bead necklace, 2) a metal-incrusted ear-ring made of, supposedly, a synthetic resin, 3) a pipe bit made of melted and pressed Baltic amber; 4) West African copal, 5) Indonesian copal, 6) a sandarac from Australia, 7) a pine tar, 8) a mastic resin.

Raman spectra were acquired with a Thermo Scientific DXR™ Raman microscope using 780 nm laser excitation and 14 mW of power at sample. The typical exposure time was set to 5 minutes to maximize signal-to-noise ratio. The real-time autofluorescence correction was enabled to minimize fluorescence effects in the spectra. No further smoothing of spectral data was applied.

Results and discussion

Distinguishing amber from its synthetic forgeries by Raman spectroscopy is rather straightforward. Figure 1 shows the "fingerprint" region of the Raman spectra of an authentic Baltic amber and a synthetic resin, as well as a reference spectrum of bisphenol-A. The spectrum of the synthetic resin (Figure 1.2) bears little similarity with that of amber (Figure 1.1), but has features that can be unambiguously attributed to the bisphenol-A, the component of an epoxy resin. Thus, in the "fingerprint" spectral region, amber can be readily distinguished from synthetic plastics due to a significant difference in chemical composition and the identification of the synthetic plastics can be conducted using a search against extensive Raman spectral libraries of polymers.

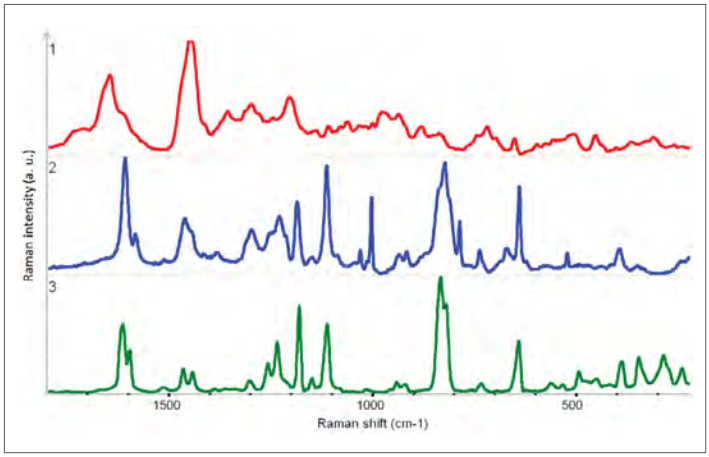

Figure 1: Raman spectra of: (1) authentic Baltic amber from a contemporary bead necklace; (2) synthetic resin from an ear-ring; and (3) bisphenol-A from the Nicolet Standard Collection of Raman Spectra. The spectra are normalized to the most intense spectral bands.

Discrimination between amber and copal is slightly more involved because of their chemical similarities. Figure 2 shows the Raman spectra of amber and two copal samples of different origins. The most conspicuous features in all spectra are the bands at 1646 cm^{-1} and 1450 cm^{-1}, resulting from the exomethylene stretching ν(C=C), and the scissoring type deformation $\delta(CH_2)$ vibration in resin structure, respectively. It has been shown [2-4] that the intensity ratio of the bands at 1646 cm^{-1} and 1450 cm^{-1} (I_{1646}/I_{1450}) is a good indicator of the maturity of fossilized resins. In general, the ratio is >1 for immature resins such as copal, and <1 for mature resins such as amber. Our experiment results conform to that criterion. In Figure 2, the peak height ratio I_{1646}/I_{1450} is about 0.8 for amber (1) and 2.5 and 1.1. for copal (2) and (3), respectively. In addition, there are noticeable differences between amber and copal in the spectral region below 1400 cm^{-1}, which is dominated by a series of less intensive peaks, especially, in the 800-500 cm^{-1} range. It was found that thermal and mechanical alteration of the amber leads to noticeable spectral changes in the region of 1800 - 1400 cm^{-1}, as shown in Figure 3.

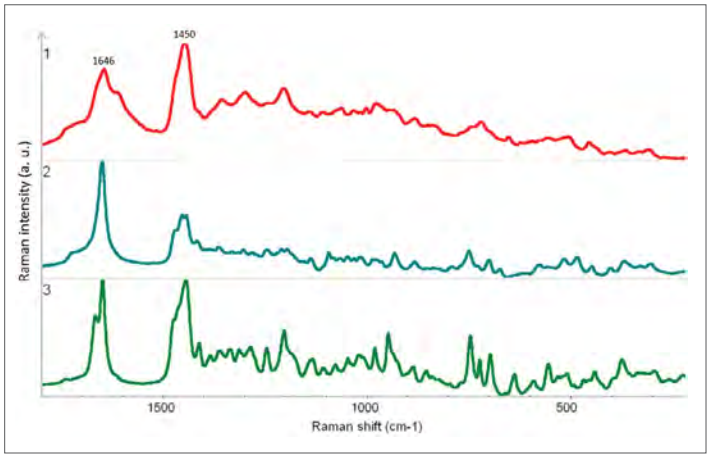

Figure 2: Raman spectra of (1) melted and pressed Baltic amber from a pipe bit; (2) Indonesian copal; and (3) West African copal. The spectra are normalized to the most intense spectral bands.

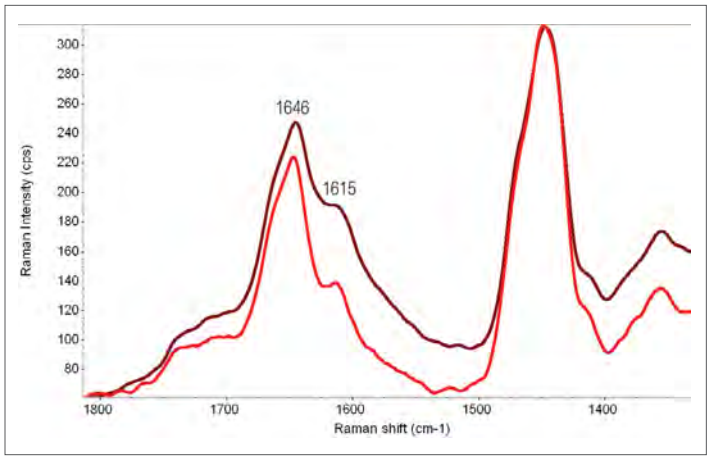

Figure 3: The Raman spectra of Baltic amber from bead necklace (red) and melted and pressed amber from a pipe bit (brown).

The band at 1646 cm^{-1} becomes broader, and the intensity of the shoulder at about 1615 cm-1 associated with the stretching of aromatic C=C increases in the spectrum of the processed amber. In [6], these changes have been observed and attributed to the increase of the aromaticity as the result of the thermal impact to the material.

Raman spectroscopy can be used to differentiate amber from other types of natural resins that look similar to amber. Figure 4 shows the Raman spectra of three different resins. In the spectrum of mastic resin (1), the ratio I_{1646}/I_{1450} is <1 indicating its similarity to amber. However, the band at 1646 cm^{-1} in the spectrum of mastic resin exhibits a prominent shoulder at 1710 cm^{-1} less noticeable for amber (Figure 2.1) that is ascribed to the stretching mode ν(C=O). For the pine tar (2) and sandarac from Australia (3), the ratio I_{1646}/I_{1450} is >1 and ≈1, respectively, typical for natural resins. In the spectrum of pine tar (2), there is also a salient side peak at about 1615 cm^{-1}.

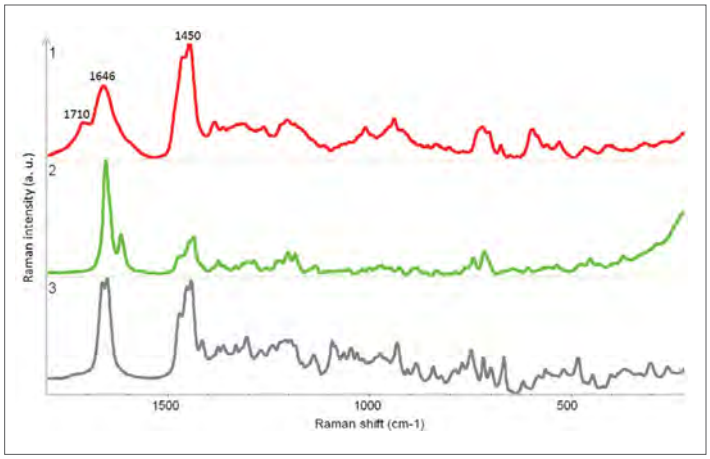

Figure 4: The Raman spectra of: (1) a mastic resin; (2) a pine tar; and (3) a sandarac from Australia. The spectra are normalized to the most intense spectral bands.

All the collected spectra feature high signal-to-noise ratios and sufficient spectral resolution, allowing for the observation of fine spectral details for differentiation purpose.

Conclusions

Dispersive Raman spectroscopy is a practical tool for non-destructive identification and authentication of amber and its imitations made of natural and synthetic resins.

The spectral characteristics of amber are demonstrated to be vastly different from, for example, epoxy resin often used for amber imitation. The fluorescence typical for amber, copal and other natural resins are effectively suppressed by using a 780-nm excitation, or it can be removed with a real-time automated fluorescence correction procedure available in Thermo Scientific™ OMNIC™ software. The use of dispersive Raman instrumentation along with visible lasers enabled shorter sampling times in comparison with FT-Raman, where spectral acquisition times as long as hours are often required[5].

References

1. Beck C.W. *Spectroscopic investigation of amber, Applied Spectroscopy Reviews*, Vol. 22, 57–110, 1986

2. Edwards H.G.M., Farwell D.W. *Fourier transform-Raman spectroscopy of amber*, Spectrochimica Acta, Part A, Vol. 52, 1119-1125, 1996.

3. Brody R.H., Edwards H. G.M , Pollard A.M., *A study of amber and copal samples using FT-Raman spectroscopy*, Spectrochimica Acta, Part A, Vol. 57, 1325–1338, 2001.

4. Vandenabeele P., Grimaldi D.M., Edwards H.G.M., Moens L. *Raman spectroscopy of different types of Mexican copal resins, Spectrochimica Acta*, Part A, Vol. 59 2221-2229, 2003.

5. Edwards H.G.M., Farwell D.W., Jorge Villar S.E. *Raman microspectroscopic studies of amber resins with insect inclusions, Spectrochimica Acta*, Part A, Vol. 68, 1089–1095, 2007.

6. Badea G.I., Caggiani M.C., Colomban P., Mangone A., Teodor E.D., Teodor E.S., Radu G.L. *Fourier Transform Raman and Statistical Analysis of Thermally Altered Samples of Amber*, Applied Spectroscopy, Vol. 69, 1457-1463, 2015.

Find out more at **www.thermofisher.com/raman**

ThermoFisher SCIENTIFIC

AN52910_E 12/16M

thermo scientific

APPLICATION NOTE AN52984

Confocal Raman analysis of a transdermal nicotine patch by a DXR2 Raman Microscope

Author

Mohammed Ibrahim, Ph.D.
Thermo Fisher Scientific, USA

Application benefit

Confocal Raman microscopy provides a facile means to analyze multilayer polymers and to identify the active pharmaceutical ingredient (API) in a nondestructive manner with minimal sample preparation.

Keywords

Confocal Raman microscopy, Transdermal patch, Chemical mapping, Multilayer polymer

Figure 1: DXR2 Raman microscope

Introduction

Transdermal patches are medication delivery systems that adhere to the skin and deliver drugs through a controlled release into the skin and then into the bloodstream. Nicotine transdermal patches are a form of nicotine replacement therapy used to aid in smoking cessation.

Transdermal patches have multiple layers: the release liner, the adhesive, the membrane, and the backing. The release liner protects the adhesive and drug formulation and is removed prior to application. The adhesive adheres the patch to the skin. The membrane layer (or layers) contains the drug and controls the rate of diffusion of the drug out of the patch and into the skin. The backing is the outermost layer of the patch and protects the formulation while the patch is worn.

It is important to understand the composition of a transdermal patch to perform quality control and product improvement, and to monitor the drug release mechanism. Traditional methods of analysis are typically destructive, either requiring dissolving the sample for extraction (e.g., GC-MS, LC-MS) or physically cross-sectioning the patch (e.g., SEM, TEM). Using confocal Raman analysis by the Thermo Scientific™ DXR™2 Raman Microscope, the layers of a commercially available transdermal nicotine patch were examined without sample destruction.

Experimental

A transdermal nicotine patch sample was mounted onto a gold-coated microscope slide with the backing layer facing the microscope objective, and the release liner at the bottom. Raman confocal line depth profiling and area depth profiling were performed with a DXR2 Raman microscope (Figure 1) using 532 nm laser, 5 mW laser power at the sample, 50X objective, 25 µm confocal pinhole aperture, and with auto exposure (S/N = 200). For the line depth profiling (Z-profiling), a depth of 220 µm was probed by using a 5 µm step size (containing 45 points or spectra). For the area depth profiling, a vertical X-Z area of 120 µm (X) by 245 µm (Z) was probed by using a 5 µm step size along the Z-axis and 20 µm along the X-axis. The area is composed of 350 points or spectra.

ThermoFisher SCIENTIFIC

To correlate an optical image with the Raman profile, a small cross sectional piece of the nicotine patch was mounted vertically on the glass slide.

The Thermo Scientific™ OMNIC™ for Dispersive Raman Software Suite, which includes Thermo Scientific™ OMNIC™ Atlμs™ Software, was used for data collection, processing, and analysis, including identification of the layer composition and estimation of the layer thickness. The multi-component spectral analysis was performed using Thermo Scientific OMNIC Specta Software.

Results and discussion

A Raman line depth profile map obtained using the OMNIC software suite is shown in Figure 2a. In the figure, the depth profile is displayed in a 2-D contour map and reveals the changes in the Raman peaks (vertical lines) as the focal point probes through the layers. The rainbow color scheme of the contour map shows the intensity of the Raman peaks as color, with red indicating the highest intensity and blue the lowest intensity. A total of six layers were identified with thicknesses ranging from ~15 µm to ~75 µm. The thickness of each layer was estimated by the full width at half maximum (FWHM) value method described in the Thermo Scientific Application Note 51718[1]. Figure 2b shows the optical image of the physically cross-sectioned sample. The optical image provides a visual representation of the layer thickness based on contrast and although it is comparable to the chemical image, some of the layers are not easily identifiable.

Figure 3 shows the representative Raman spectra for each layer in the Raman line depth profile. The chemical composition of each layer was initially identified by performing a library search against the Thermo Scientific High-Resolution Raman Polymer Library using OMNIC software.

Layer 1, the backing is poly(ethylene terephthalate) or PET. Layers 2 and 4 are composed of microporous polyethylene (PE) that acts as a controlled release agent for nicotine, which is located at the ethylene/vinyl acetate copolymer (EVA) reservoir layer (layer 3). Layer 5 is a polyisobutylene (PIB) adhesive and PET. Layer 6, the release liner is also composed of PET.

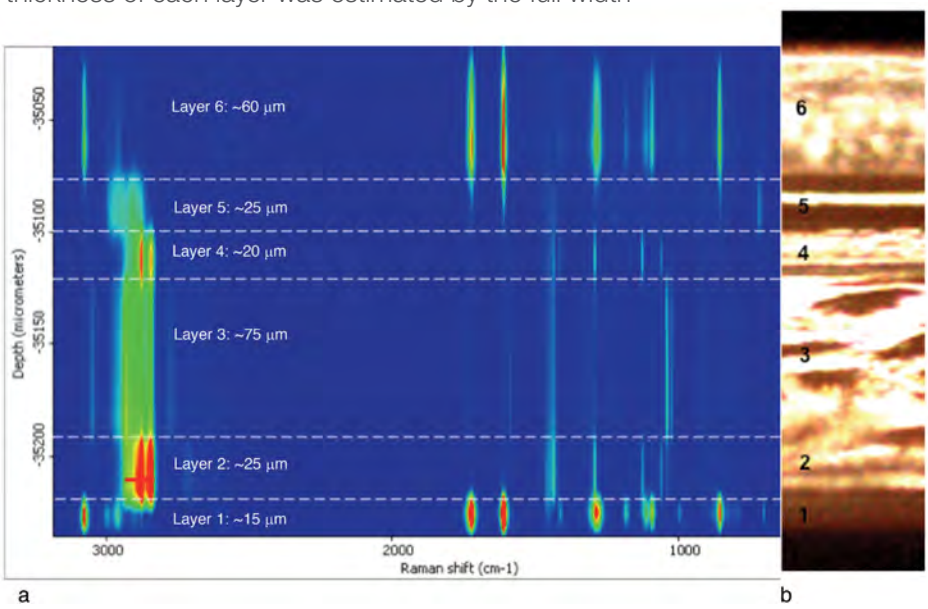

Figure 2: a) Raman line depth map (Z-map) for the transdermal nicotine patch. The dashed white lines indicate the approximate depth of each of the six layers. **b)** An optical image of the cross section.

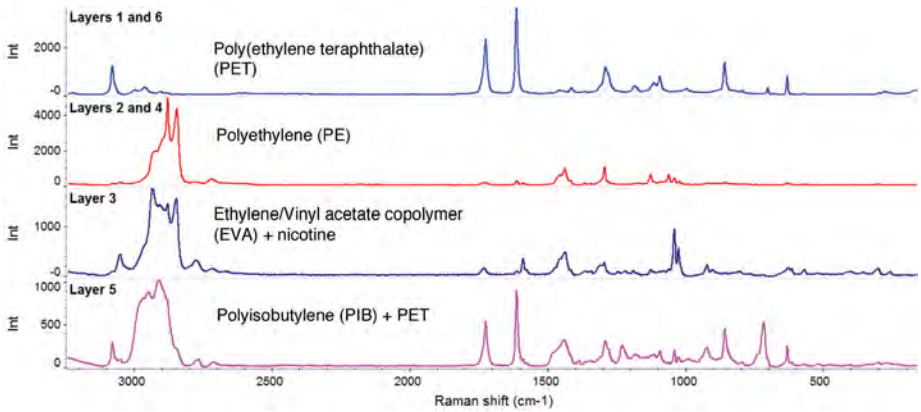

Figure 3: Representative Raman spectra for each layer of the patch.

The presence of nicotine in the EVA reservoir layer (layer 3) was identified by the OMNIC Specta software using the Multi-Component Search option, as shown in Figure 4. The patented Multi-Component Search allows one to identify constituents in mixture samples without the tedious manipulations required by the traditional search and subtract processes. Not only did the search identify S-(-)-nicotine as the second component (green in Figure 4), in addition to the EVA (orange), it also provided the composite value (%) of the two components. The composite value is a scaling factor indicating the amount of each found reference represented in the composite spectrum. It should be noted, however, that the composite values cannot be taken as a quantitative percentage of the materials, which requires measurements by a primary quantitative analytical technique.

Figure 5 shows correlation profile images obtained from the Raman confocal area depth (X-Z) profiling of the same nicotine patch sample. Each of the images was obtained by using the correlation between the map spectra and the reference Raman spectrum of each layer. The red color in the images indicates the highest correlation to a specific reference spectrum, whereas the blue indicates no correlation. For example, the EVA+nicotine correlation image (Figure 5, right) shows a single red colored layer indicating that this layer has the highest correlation to the EVA+nicotine reference spectrum, thus showing that this is the layer where these two components are located. The presence of 6 layers in these images is consistent with results of the confocal line depth profile analysis (Figure 2). In addition, the X-Z correlation images here reveal relatively uniform thickness of the layers.

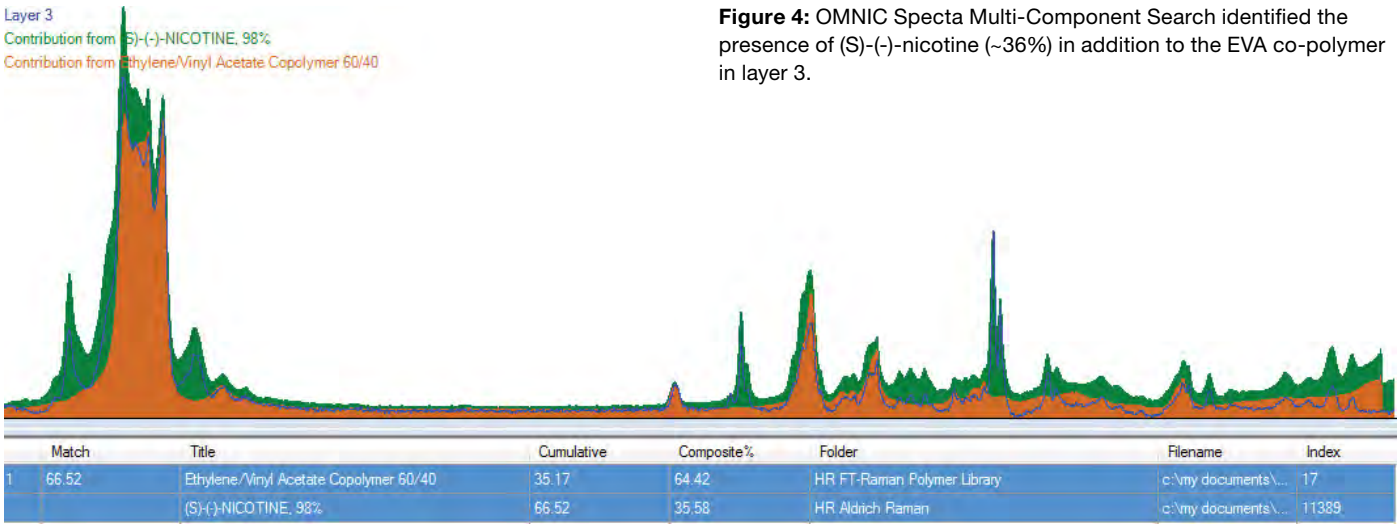

	Match	Title	Cumulative	Composite%	Folder	Filename	Index
1	66.52	Ethylene/Vinyl Acetate Copolymer 60/40	35.17	64.42	HR FT-Raman Polymer Library	c:\my documents\...	17
		(S)-(-)-NICOTINE, 98%	66.52	35.58	HR Aldrich Raman	c:\my documents\...	11389

Figure 4: OMNIC Specta Multi-Component Search identified the presence of (S)-(-)-nicotine (~36%) in addition to the EVA co-polymer in layer 3.

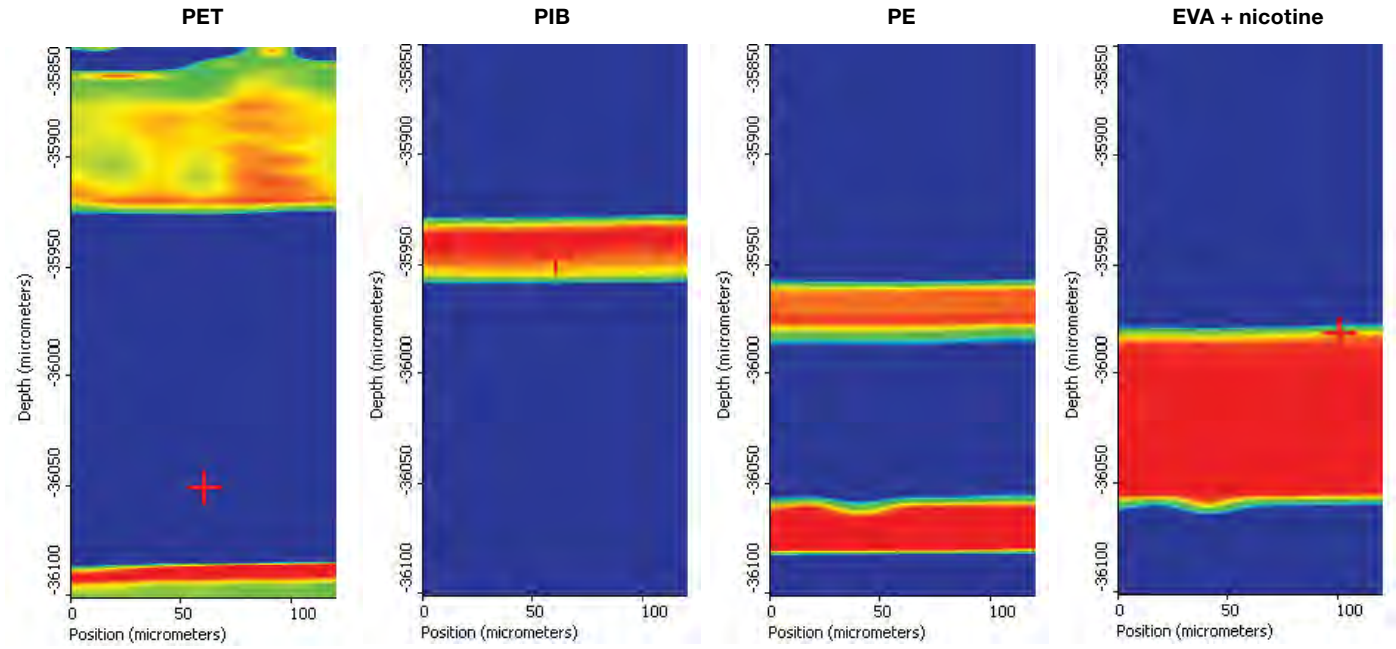

Figure 5: X-Z correlation profile images generated by the reference Raman spectrum of each layer.

Conclusion

Existing techniques for analyzing a multilayer polymer like a transdermal nicotine patch are labor intensive, time-consuming, and would require destruction of the sample. Using confocal Raman analysis, the analysis was quick, and the sample integrity was preserved. The chemical composition of each layer was determined using OMNIC for Dispersive Raman and OMNIC Specta software suites. OMNIC Specta Multi-Component Library Search identified the constituents in layer 3, a mixture of nicotine and an EVA co-polymer, which is easier than tedious manipulations required by traditional search and subtract processing.

References

1. Guillory P., Deschaines T., Henson P. *Confocal Raman microscopy analysis of multilayer polymer films*, Thermo Scientific Application Note 51718, 2008.

Find out more at **thermofisher.com/Raman**

ThermoFisher SCIENTIFIC

thermo scientific

APPLICATION NOTE AN53001

In situ density determination of polyethylene in multilayer polymer films using Raman microscopy

Authors

Mohammed Ibrahim, Ph.D.
Herman He, Ph.D. and
Rui Chen, Ph.D.
Thermo Fisher Scientific
Madison, WI, USA

Keywords

Polyethylene (PE), density, Raman Microscopy, DXR2 Raman Microscope, Partial Least Squares (PLS)

Application benefits

Polyethylene density determination based on Raman microscopy and Partial Least Squares (PLS) regression is applicable for both pellet and film samples. The confocal capability of Raman microscopy allows for *in situ* density determination of PE layers within multilayer polymer films, without the need for tedious and challenging sample preparations.

Thermo Fisher Scientific solutions

- DXR2 Raman Microscope
- OMNIC software
- TQ Analyst software

Introduction

Thermo Scientific DXR2 Raman Microscope

Polyethylene (PE) is one of the most common plastics in the world with an annual global production of around 80 million tons.[1] Unlike other commercial polymers, PE can be manufactured across a range of densities that are related to the spacing between the polymer chains.[2] For examples, High-Density PE (HDPE, 0.941-0.965 g/cm^3) is mainly comprised of linear PE chains that can closely approach each other, thus creating very densely packed networks. Conversely, Low-Density PE (LDPE, 0.910-0.940 g/cm^3) has excessive branching that causes a less compact molecular structure. Linear Low-Density PE (LLDPE, <0.940 g/cm^3), too, has a large number of branches, but the branches are shorter than those in LDPE. Because the density of PE can be controlled and varied, it provides an important mechanism to control its properties to suit different applications. PE density is therefore a vital part of the material characterization and selection process.

There are several standard methods for PE density measurement, such as ISO 1183-1/ASTM D792 (immersion method)[3], ISO 1183-2/ASTM D1505 (density gradient method),[4] and ASTM D4883 (ultrasound method)[5]. These methods, however, are primarily geared towards PE samples in a “pure” form such as pellets and single-layer films. Challenges arise when PE is present in multilayer films, which are widely used in food, pharmaceutical and consumer product packaging. Extensive sample preparations, including microtoming and separation of layers using solvents, are required to isolate the PE layer(s) before analysis, which can be labor-intensive and time-consuming.[6]

ThermoFisher SCIENTIFIC

To that end, Raman microscopy could offer an *in situ* density determination of PE layers in multilayer films by leveraging its confocal capability. Raman spectroscopy has long been utilized to investigate the structure of polymers, including molecular conformation, orientation, and crystal structure.[7-9] Combined with multivariate analyses such as principal component analysis (PCA) and partial least squares (PLS) regression whereby statistically observed spectral variations are correlated with known sample properties, crystallinity, density and melting point can be predicted.[7] Existing literature, however, has also been limited to bulk PE pellets. In our previous report,[10] we expanded the scope of the methodology to include PE films. It is demonstrated that Raman microscopy in combination with a PCA based discriminant analysis can qualitatively distinguish HDPE and LDPE in both pellet and film forms. In this application note, we will describe the development of a Partial Least Squares (PLS) model to quantitatively determine the density of PE layers in both single-layer and multilayer films using Raman microscopy.

Experimental

A total of 25 PE samples (12 pellets and 13 films) with different known densities (Table 1) were used for developing a PLS model for density determination. All samples were used as received. A clear transdermal nicotine patch sample was used for identifying the PE layers and *in situ* determination of PE layer densities. The sample was mounted onto a gold-coated microscope slide with the backing layer facing the microscope objective, and the release liner at the bottom.

A Thermo Scientific™ DXR2™ Raman Microscope was used for collecting Raman data. For each of the pellet samples, Raman spectra were collected from 3 different pellets and averaged. For each of the film samples, Raman spectra were collected from 3-4 locations across the surface of the sample. An averaged spectrum was then used for final analysis. A 532 nm laser was used with 2 mW laser power at the sample. A 10x objective and a 50 µm slit aperture were used to obtain more representative spectra from the samples. Total acquisition time for each spectrum was 30 seconds (3 second exposure x 10 exposures). For the transdermal nicotine patch sample, Raman confocal line depth profiling was performed using a 532 nm laser, 5 mW laser power at the sample, 50x objective, 25 µm confocal pinhole aperture, and with auto exposure (S/N = 200). A depth of 220 µm was probed by using a 5 µm step size (containing 45 points or spectra).

Thermo Scientific™ OMNIC™ software was used for instrument control and data acquisition. Thermo Scientific™ TQ Analyst™ software was used for chemometric analysis of the Raman data.

Results and discussion

Raman spectra of HDPE, LDPE, and LLDPE

Representative Raman spectra of HDPE, LDPE, and LLDPE samples are shown in Figure 1. There are noticeable differences among three types of PE samples in both CH stretching (2900-3100 cm^{-1}) and CH_2 bending and twisting (1250-1500 cm^{-1}) regions. The intensity of the symmetric CH_2 stretching mode at 2848 cm^{-1} (relative to the asymmetric CH_2 stretching mode at 2882 cm^{-1}) decreases in the order of LLDPE > LDPE > HDPE (Figure 1A). In the CH_2 bending and the CH_2 twisting region (Figure 1B), the intensity of the CH_2 bending mode at 1416 cm^{-1} (relative to the CH_2 bending mode at 1440 cm^{-1}) is higher for HDPE than for LDPE. The 1416 cm^{-1} peak is completely absent for the LLDPE film sample (#19). This observation agrees with the previous reports that the 1416 cm^{-1} and 1440 cm^{-1} peaks are indicators of crystalline and amorphous PE phases, respectively.[7,8] The higher the crystallinity, the higher the density. Since the CH_2 bending region (1400-1500 cm^{-1}) is sensitive to the density of PE, it was selected for subsequent quantitative analysis.

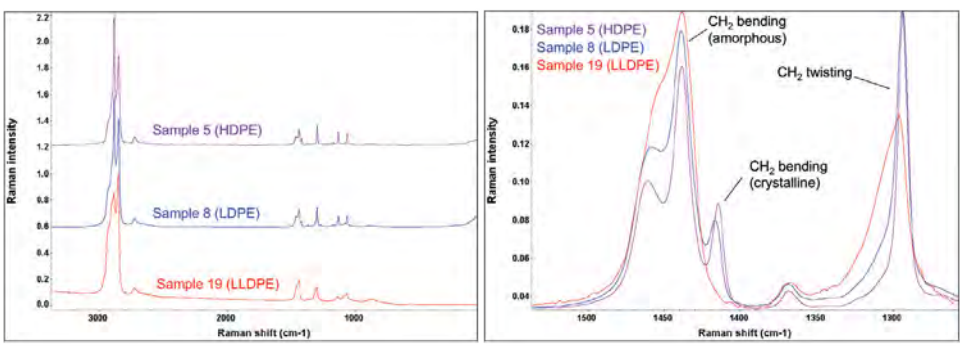

Figure 1: Representative Raman spectra of HDPE, LDPE, and LLDPE samples. **(A)** Full spectral range in stack view. **(B)** CH_2 bending and CH_2 twisting region in overlay view.

Data processing

Peak area for pathlength correction option in the TQ Analyst software was used to normalize Raman spectral intensities. The peak area of the CH_2 bending mode at 1440 cm^{-1} was used for the normalization (1422-1452 cm^{-1} range, Figure 2A). An averaged two-point baseline correction was used to account for baseline shifts/noise.

Developing a PLS model for PE density determination

Partial Least Squares (PLS) algorithm[11] from the TQ Analyst software was used to develop a model for PE density determination. PLS is a quantitative regression algorithm through statistical analysis. It uses spectral covariance and factorial analysis to extract significant and relevant chemical information from sample spectra as factors, then correlate them with sample properties such as concentration, crystallinity and density. A total of 20 samples, a mix of pellets and films, were used as the calibration standards. Five additional pellet and film samples with density values spread across the density range of the samples were selected as the validation standards (Table 1). A spectral range of 1400-1500 cm^{-1} with averaged two-point correction for baseline (Figure 2B) was used in the method.

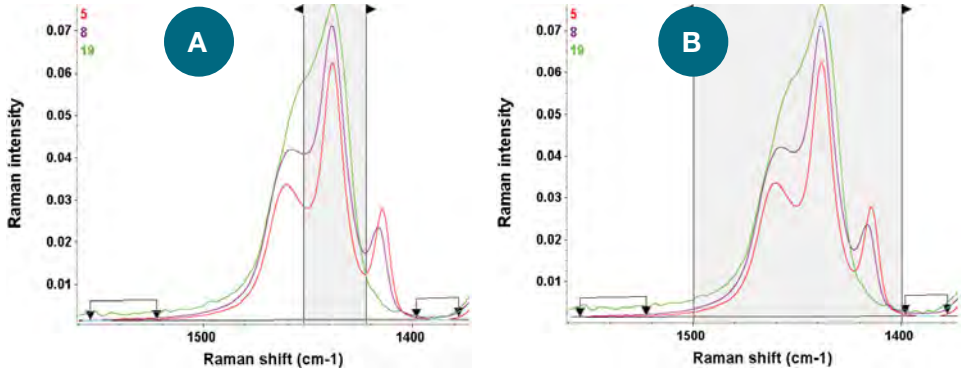

Figure 2: (A) Peak Area Ratio to normalize Raman spectral intensities, showing the CH_2 bending peak region for normalization. **(B)** Spectral range used for PLS calibration. In both cases, an averaged two-point option was used for baseline correction.

	Sample #	Actual Density (g/cm^3)	PE Type	Usage	Calculated Density (g/cm^3)	Difference (g/cm^3)	% Difference
Pellets	1	0.9460	HDPE	Calibration	0.9454	0.0006	0.06%
	2	0.9505	HDPE	Calibration	0.9486	0.0019	0.20%
	3	0.9510	HDPE	Calibration	0.9509	0.0001	0.01%
	4	0.9470	HDPE	Validation	0.9523	-0.0053	-0.56%
	5	0.9620	HDPE	Calibration	0.9564	0.0056	0.58%
	6	0.9600	HDPE	Calibration	0.9594	0.0006	0.06%
	7	0.9195	LDPE	Calibration	0.9236	-0.0041	-0.45%
	8	0.9170	LDPE	Calibration	0.9183	-0.0013	-0.14%
	9	0.9235	LDPE	Calibration	0.9250	-0.0015	-0.16%
	10	0.9300	LDPE	Calibration	0.9264	0.0036	0.39%
	11	0.9235	LLDPE	Calibration	0.9295	-0.0060	-0.65%
	12	0.9185	LLDPE	Calibration	0.9259	-0.0074	-0.81%
Films	13	0.9496	HDPE	Calibration	0.9568	-0.0072	-0.76%
	14	0.9606	HDPE	Calibration	0.9556	0.0050	0.52%
	15	0.9460	HDPE	Calibration	0.9456	0.0004	0.04%
	16	0.9247	LDPE	Calibration	0.9225	0.0022	0.24%
	17	0.9258	LDPE	Calibration	0.9241	0.0017	0.18%
	18	0.9297	LDPE	Calibration	0.9276	0.0021	0.23%
	19	0.8598	LLDPE	Calibration	0.8604	-0.0006	-0.07%
	20	0.8650	LLDPE	Calibration	0.8623	0.0027	0.31%
	21	0.8881	LLDPE	Validation	0.8812	0.0069	0.78%
	22	0.9008	LLDPE	Calibration	0.8993	0.0015	0.17%
	23	0.9040	LLDPE	Validation	0.9072	-0.0032	-0.35%
	24	0.9236	LLDPE	Validation	0.9215	0.0021	0.23%
	25	0.9367	LLDPE	Validation	0.9349	0.0018	0.19%

Table 1: PE samples and their densities.

*Rows highlighted in green are the samples used for validation.

Figure 3 shows the calibration results for PE densities obtained with the 3-factor PLS model. The inset is the Predicted Residual Error Sum of Squares (PRESS) plot. In the current case, a 3-factor model suffices as the contribution from the 4th and 5th factors are negligible. The calibration curve has a correlation coefficient of 0.9914. The RMSE (Root Mean Square Error) values are 0.00360 for the calibration samples and 0.00432 for the validation samples, respectively. The results are also summarized in Table 1. For all 25 samples, the calculated densities are within ±0.81% of the actual values. It is important to note that the percent differences do not exhibit any bias between pellets and films, indicating that the sample form (pellets vs. films) has no bearing on the model performance.

Density Determination of PE films

Figure 4 demonstrates an example of applying the Raman spectrum and the PLS model to predict the density of a PE film sample. The predicted density is 0.9014 g/cm^3, showing a good agreement with the actual density of 0.9008 g/cm^3.

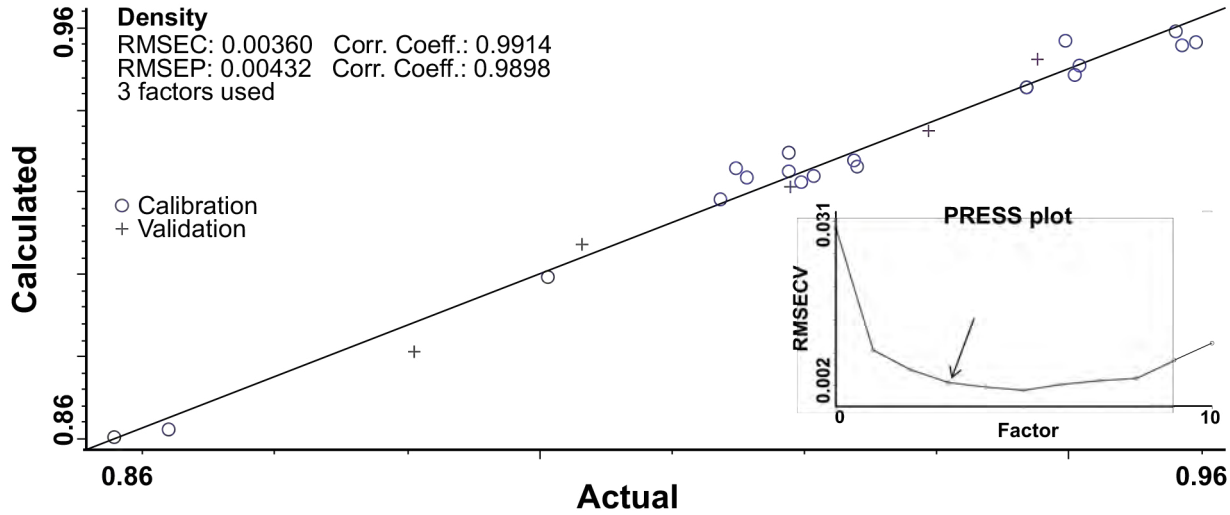

Figure 3: Calibration results for PEs of different densities using a PLS quantitative analysis. The ○ denotes calibration standards and the + denotes validation standards. Inset is the PRESS plot for the PLS calibration. Three factors were used in the current PLS calibration model.

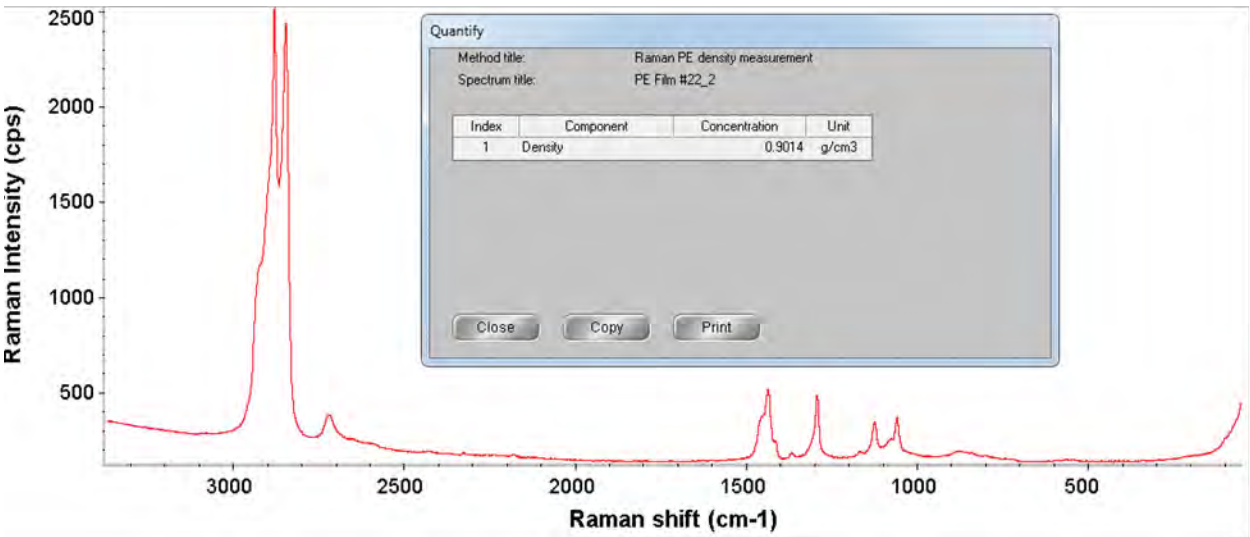

Figure 4: Prediction of the density of a PE film sample using its Raman spectrum and the PLS model. The known density of the film is 0.9008 g/cm^3 and the predicted density is 0.9014 g/cm^3.

Figure 5A shows the Raman confocal depth profile of a clear transdermal nicotine patch. A total of 6 polymer layers were identified, including two PE layers – PE layer 1 (part of the backing layer) and PE layer 2 (closer to the release liner). There are perceptible differences in the Raman spectra between the two PE layers (Figure 5B and 5C). Applying the PLS model, the densities are determined to be 0.9150 g/cm^3 for PE Layer 1 and 0.9583 g/cm^3 for PE Layer 2, placing PE layer 1 in the LDPE /LLDPE class and the PE Layer 2 in the HDPE class. The classification of the PE layers based on the predicted densities conforms to other reports: LDPE/ LLDPE is used in the occlusive backing layer for its flexibility whereas HDPE is used as the rate-controlling membrane as an integral part of the reservoir diffusion control machanism.[12-13] While the exact densities of the two PE layers are not available, the results presented here nonetheless demonstrates the advantage of using Raman microscopy combined with the PLS method for density determination. The confocal capability of Raman microscopy allows for *in situ* PE density determination in multi-layer films without the need to isolate the individual PE layers.

Conclusions

Raman microscopy is a powerful analytical tool for PE density determination. Since PE chains in crystalline and amorphous domains exhibit unique Raman features in the CH_2 bending region, a PLS model based on the Raman features in the 1400-1500 cm^{-1} region was successfully developed. The model is applicable for both pellet and film samples, showing a good agreement between actual and predicted density values. Applying the model to a real-world multilayer film containing two PE layers, the predicted density values correctly place the two layers into their respective PE classes. More importantly, the confocal capability of Raman microscopy allows for *in situ* density determination of PE layers within multilayer polymer films, without the need for tedious and challenging sample preparations required by many other techniques. The presented methodology should be of interest for PE manufacturers as well those who perform failure analysis, reverse engineering, and polymer composites development.

Acknowledgement

The authors would like to thank Wanda Weatherford at Chevron Phillips Chemical Company for providing PE pellet samples and Rajesh Paradkar at Dow Chemical Company for providing PE film samples.

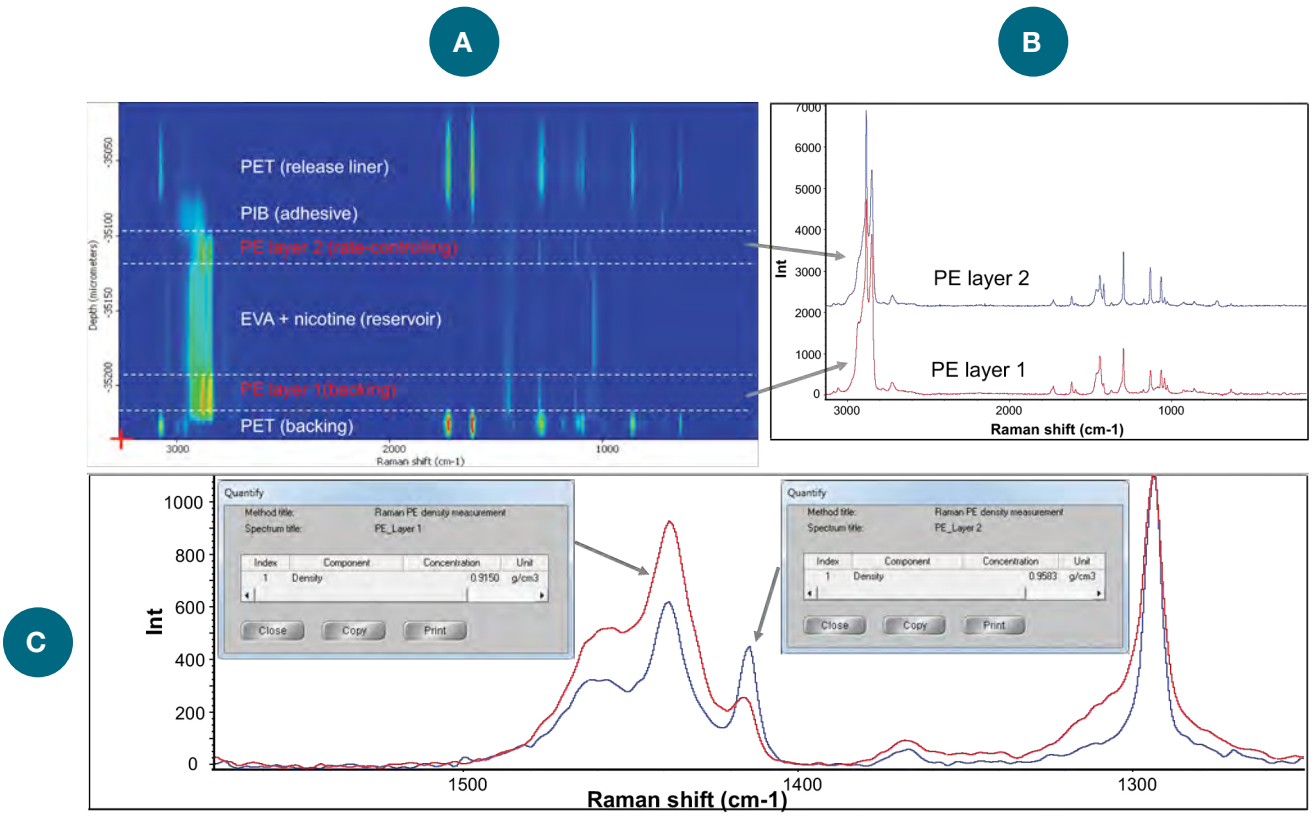

Figure 5: (A) Confocal Raman line depth map of a multilayer polymer patch, showing the presence of two types of PE layers. **(B)** Raman spectra of the two PE layers in full spectral range. **(C)** Raman spectra of the two PE layers in the CH_2 bending and CH_2 twisting region. The insets in **(C)** show the calculated densities of the two PE layers using the 3-factor PLS model. PET = poly(ethylene terephthalate), EVA = ethylene/vinyl acetate copolymer, PIB = polyisobutylene.

thermo scientific

References

1. Piringer O.G. and Baner A.L., ed. *Plastic Packaging: Interactions with Food and Pharmaceuticals*. 2nd ed. Weinheim: Wiley-VCH; 2008.
2. Polyethylene, The Essential Chemical Industry – online, http://www.essentialchemicalindustry.org/polymers/polyethene.html, retrieved on 11/27/2017.
3. (a) ISO 1183-1:2012, Plastics – *Methods for determining the density of non-cellular plastics – Part 1: Immersion method, liquid pyknometer method and titration method*; ANSI New York, NY. (b) ASTM D792-13, *Standard test methods for density and specific gravity (relative density) of plastics by displacement*; ASTM International, West Conshohocken, PA, 2013.
4. (a) ISO 1183-2:2004, *Plastics – Methods for determining the density of non-cellular plastics – Part 2: Density gradient column method*. ANSI New York, NY. (b)ASTM D1505-10, *Standard test method for density of plastics by the density-gradient technique*; ASTM International, West Conshohocken, PA, 2010.
5. ASTM D4883-08, *Standard test method for density of polyethylene by the ultrasound technique*; ASTM International, West Conshohocken, PA, 2008.
6. Mieth A., Hoekstra E., and Simoneau C. *Guidance for the identification of polymers in multilayer films used in food contact materials*: *User guide of selected practices to determine the nature of layers*, EUR 27816 EN, 2016; doi: 10.2788/10593.
7. Sato H., Shimoyama M., Kamiya T., Amari T., Sasic S., Ninomiya T., Siesler H.W., and Ozaki Y. *Raman spectra of high-density, low-density, and linear low-density polyethylene pellets and prediction of their physical properties by multivariate data analysis*, J. Appl. Polym. Sci., 2002, 86, 443–448.
8. Strobl G.R. and Hagedorn W. *Raman spectroscopic method for determining the crystallinity of polyethylene*, J. Polym. Sci. B Polym. Phys., 1978, 16, 1181-1193.
9. Williams K.P.J. and Everall, N. J. *Use of micro Raman spectroscopy for the quantitative determination of polyethylene density using partial least-squares calibration*, J. Raman Spectrosc. 1995, 26, 427-433.
10. Ibrahim M. and He H. *Classification of polyethylene by Raman spectroscopy*, Thermo Scientific Application Note AN52301, 2017.
11. Thermo Scientific Product Overview. *TQ Analyst Software Chemometric Algorithms*, 2009.
12. Kearney C. J. and Mooney D.J. *Macroscale delivery systems for molecular and cellular payloads*, Nat. Mater., 2013, 12, 1004-1017
13. Allen L. V. and Ansel H. C., ed. *Ansel's Pharmaceutical Dosage Forms and Drug Delivery Systems*, 10th ed. Lippincott Williams & Wilkins; 2013.

Find out more at **www.thermofisher.com/Raman**

ThermoFisher SCIENTIFIC

APPLICATION NOTE

No. AN52959

Simultaneous rheology and Raman spectroscopy during the melting and recrystallization of polypropylene

Authors: Nathan C. Crawford and David Drapcho

Introduction

Rheology is the study of the flow and deformation of matter, including fluids to solid-like materials (and anything in between). Rheological measurements are commonly used to examine or induce bulk physical material changes, such as melting, crystallization, gelation, and/or polymerization etc. Raman spectroscopy, on the other hand, is a vibrational spectroscopic technique that can provide insights to these processes at the molecular level, both chemically and morphologically. However, until very recently[1], Raman studies are often conducted *ex-situ*, whereby Raman spectra are acquired prior to and after the observed physical transformation. The true chemical/morphological changes driving these processes are largely left uncaptured, leaving much room for data interpretation and speculation surrounding these dynamic physicochemical relationships.

The Thermo Scientific™ HAAKE™ MARSXR (Figure 1) is a fully integrated RheoRaman system that enables simultaneous rheology and Raman spectroscopy measurements. The seamless hyphenation of these two techniques allows for real-time, *in-situ* measurements of both physical and chemical/morphological properties with great ease. This multimodal analytical tool offers several advantages compared to the traditional *ex-situ* approach. First, data collection efficiency is greatly improved by combining multiple one dimensional experiments into a single multifaceted experiment. Secondly, because both techniques are employed simultaneously, sample fidelity is preserved and the transformation of the material is captured in real-time. And finally, sample consumption is reduced, which can be beneficial for new material/formulation development where sample quantities are limited and/or expensive.

Figure 1:
The Thermo Scientific HAAKE MARSXR RheoRaman system.

In this note, a MARSXR RheoRaman system was used to investigate the temperature-dependent melting and crystallization of polypropylene, as well as the isothermal crystallization process. The melt and crystalline phase transitions of polymeric materials are commonly correlated with variations in viscous and elastic behavior during rheological analysis. In addition, these phase transitions are often associated with spectral pattern changes in characteristic Raman peaks during spectroscopic investigation. Measurements performed *ex-situ* are often challenging to compare due to discrepancies in temperature control, slight deviations in sample composition, and differences in processing history. The *in-situ* RheoRaman system, on the other hand, completely eliminates these discrepancies, allowing for a more valid analysis of the melt and crystalline phase transitions from both the macroscopic and molecular levels.

ThermoFisher SCIENTIFIC

Materials and methods

Materials

Polypropylene (Ineos Olefins and Polymers, USA, R12C-00 random copolymer) pellets were used for this study. The pellets were melted at 190 °C on the rheometer to form a continuous, disk-shaped specimen for testing.

Rheometer

Rheological measurements were performed using the Thermo Scientific™ HAAKE™ MARS™ III rheometer, equipped with a 20 mm diameter stainless steel parallel-plate rotor. In order to extract viscoelastic behavior of the polypropylene, all measurements were conducted in the oscillatory mode. Oscillatory measurements were performed at 1 Hz with a constant strain of 0.1%, while data were collected every 5 s. To soften the polypropylene and help it conform to the measuring geometry, all samples were initially loaded at 190 °C. For the melt-to-crystallization phase transition study, the temperature was decreased from 190 °C to 30 °C, at a rate of 5 °C/min. For the isothermal crystallization studies at 138 °C and 150 °C, temperature was rapidly decreased from 190 °C to 10 °C above the target temperature. The temperature was then slowly decreased until it reached the test temperature (either 138 °C or 150 °C). The temperature was then held constant for a maximum of 1 h (3600 s), while the isothermal recrystallization process was observed.

Spectrometer

Raman spectroscopy measurements were performed using the Thermo Scientific™ iXR™ Raman Spectrometer. The iXR system employed a 532 nm, 10 mW laser, a triplet spectrograph providing Raman spectra over the range 3500 to 50 cm^{-1} Raman shift (Stokes) at 5 cm^{-1} resolution, and a CCD camera cooled to -50 °C. Alignment of the laser, Raman scatter, and aperture selection within the spectrometer were all software controlled. The minimum exposure collection time is 0.1 s. For the data presented here, the exposure collection time was 4 s and 2 sample exposures were averaged per spectra collection.

RheoRaman coupling

The Raman spectrometer (Thermo Scientific iXR Raman Spectrometer) and rheometer (Thermo Scientific HAAKE MARS III) are coupled together using the Thermo Scientific™ HAAKE™ RheoScope module (Figure 2).

The iXR Raman spectrometer is free-space coupled to the rheometer with an optical train which uses two plane mirrors to direct the incident laser into the RheoScope module. Within the RheoScope, a series of mirrors directs the laser beam into a 20x objective, where the laser light is focused through a 2 mm thick fused silica window into the sample (perpendicularly to the flow or vorticity plane). Raman scattered light is collected in a 180° backscatter geometry using the 20x objective, and back into the spectrometer through the same optical train as the incident laser (eventually to the spectrograph inside the spectrometer). Free-space coupling of the laser to the rheometer, and the iXR spectrometer design, allow easy Raman excitation laser wavelength interchange to permit optimization of the laser wavelength to the sample (785 and 455 nm laser sets are also available).

The sample is positioned between the silica window and the rotor geometry attached to the rheometer measuring head (Figure 2). The objective can be adjusted for interrogation at different penetration depths within the sample, as well as positioned at various radial locations along the optical slit (from the true center to outer edge of the sample). An electrical heating element is positioned below the fused silica window to provide temperature control during testing. Cooling was provided from a temperature-controlled circulator with a 50:50 mixture of ethylene glycol and water. All instrumentation is controlled through the Thermo Scientific™ OMNIC™ and RheoWin software packages.

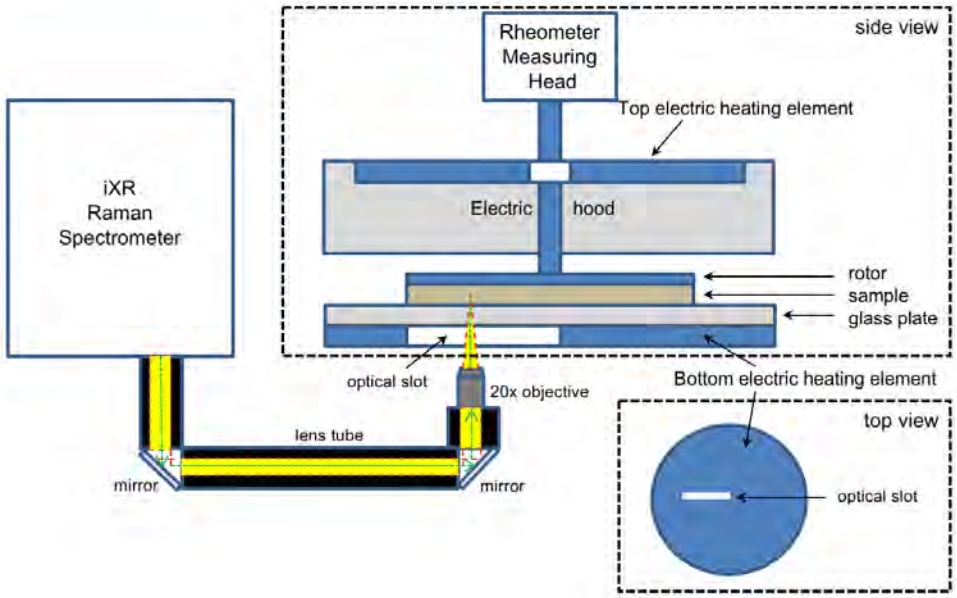

Figure 2: Schematic diagram of the MARSXR RheoRaman system (showing side and top views of the rheometer sample stage). The iXR Raman spectrometer is free-space coupled to the MARS rheometer using plane mirrors that direct light into a 20x long-working-distance objective. The objective focuses the incoming laser (green dashed line) and collects the back-scattered Raman light (yellow) coming into and out of the sample (which sits atop the rheometer stage). The optical path from the spectrometer to the rheometer is enclosed in lens tubes (black). The optical slot in the bottom heating plate permits passage of the laser beam and scattered Raman light.

The electric heater allows for a maximum temperature of 300 °C and a minimum temperature of -5 °C, with a maximum heating/cooling rate of 10 °C/min. An active electrical hood was also used to provide temperature control from above, eliminating the potential for a temperature gradient within the sample (Figure 2).

Results and discussion

The physicochemical and morphological relationships during polymer crystallization are of critical importance for polymer processing. Here we use the new MARSXR RheoRaman system to investigate the crystallization process of polypropylene (PP). Representative Raman spectra for PP at three different temperatures are shown in Figure 3. In general, the spectrum at 53 °C shows sharp peaks across the examined spectral range. These sharp spectral features suggest a high degree of conformational order, indicative of semicrystalline and crystalline structures. As temperature increased to 120 and 173 °C, these peaks began to broaden and merge together. The broadening of spectral peaks is commonly ascribed to melt behavior in polymeric materials.

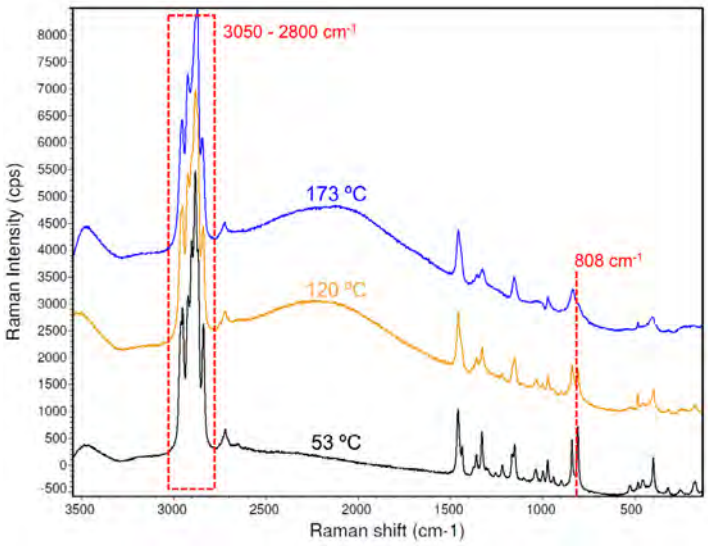

Figure 3: Raman spectra for polypropylene at 53 °C (black), 120 °C (yellow), and 173 °C (blue). The dashed line at 808 cm^{-1} and dashed box from 3050-2800 cm^{-1} indicate relevant Raman bands to the recrystallization of polypropylene.

Specific indicators in the Raman spectra for PP are the skeletal deformation of helical chains within the crystal (808 cm^{-1} peak) and the CH stretching region (3050-2800 cm^{-1} spectral range). The intensity of the 808 cm^{-1} peak will be used as a measure of the crystallinity of PP[2], and the intensity in the CH stretching region is used as a measure of the overall Raman scattering intensity during the crystallization process. For further analysis, the 808 cm^{-1} peak height was normalized by the peak area between 880 and 780 cm^{-1}. The 880-780 cm^{-1} spectral region contains skeletal chain vibrations of all conformations during the melt-to-recrystallization process[2], while the spectral features in the 3050-2800 cm^{-1} range were integrated into a total peak area. These indicators (normalized helical chain vibration peak height and overall CH stretching peak area) were then tracked throughout the melt- to crystalline-phase transition and overlaid with the in-situ rheology data (Figure 4).

The melt and recrystallization process of polypropylene was probed rheologically using small amplitude oscillatory shear measurements (Figure 4), where the storage modulus (G') and loss modulus (G") were measured as a function of temperature. G' and G" are measures of a material's elastic and viscous behavior, respectively. A liquid-like material will be more viscous than elastic (i.e., viscously dominated), and as a result, G" will be greater than G'. Conversely, a solid-like material will display more elastic than viscous behavior (i.e., elastically dominated), where G' will be greater than G".

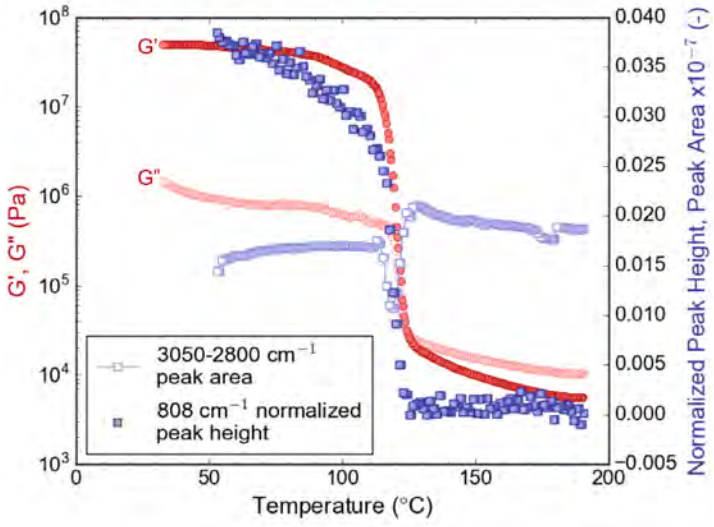

Figure 4: Polypropylene recrystallization: G' and G" (filled and open circles, respectively; plotted on the left y-axis) and the normalized 808 cm^{-1} Raman shift peak height and the 3050-2800 cm^{-1} peak area (filled and open squares, respectively; plotted on the right y-axis) as a function of decreasing temperature from 190 to 30 °C.

Initially, at high temperatures (>150 °C), G" was consistently greater than G', indicating the PP specimen was in the melt state and displaying liquid-like behavior. As the temperature decreased from 150 °C to 100 °C, an abrupt and drastic increase in both G' and G" was observed at ~125 °C. By the time the temperature reached 100 °C, G' had increased by four orders of magnitude, while G" increased by two orders of magnitude. The temperature range from 150 to 100 °C can be viewed as the melt-to-crystalline transition region for this polypropylene material. As the temperature further decreased to below 100 °C, G' was significantly greater than G" by more than a full order of magnitude, indicating the polypropylene had transitioned into the semicrystalline and/or crystalline state, and was exhibiting solid-like behavior.

The observed plateau regions and increase in G' and G" are in direct agreement with the Raman spectral data (Figure 4). In the melt region (~190-130 °C)$^{-1}$, the normalized 808 cm^{-1} peak height was near zero and remained unchanged by the decreasing temperature. However, as the PP melt began to crystallize, the normalized 808 cm^{-1} peak height significantly increased and was in unison with the abrupt increases in both G' and G". Also, as the PP sample started to crystallize, the total peak area of the CH stretching region decreased rapidly before any measurable growth of the 808 cm^{-1} band was observed. The decrease in intensity in the 3050-2800 cm^{-1} spectral region is postulated to be caused by the formation of crystallites in the PP matrix. Crystallites with dimensions on the same order of magnitude as the wavelength of the incident laser (532 nm) would scatter light, thereby creating a loss in the Raman signal intensity of the CH stretching bands. The minimum in the CH stretching profile was directly aligned with the observed crossover between G' and G" and the maximum slope of the normalized 808 cm^{-1} peak profile. The correlation between changes in the Raman spectral features and the rheological response indicate that the crystallization rate was at its maximum when the crystallite concentration was greatest. After the observed decrease in intensity, the integrated area of the CH stretching region returned to a value close to what was detected in the melt phase.

In order to further evaluate the crystallization process of PP, isothermal crystallization studies were performed at 150 and 138 °C. The PP samples were heated at a minimum of 5 min at 190 °C (to fully melt the specimen), rapidly cooled at 10 °C /min to 10 °C above the crystallization temperature, and then cooled at a slower rate of 2 °C /min until the set crystallization temperature was reached. The crystallization temperature was then held constant for a maximum of 1 h (3600 s) to observe the isothermal crystallization of PP as a function of time. Simultaneous rheology and Raman spectroscopy data were acquired in-situ during crystallization at 138 and 150 °C (Figures 5 and 6, respectively). At both isothermal temperatures, the PP material was initially viscously dominated G' < G" displaying liquid-like behavior. As time progressed, a crossover in G' and G" was observed; where the moduli increased 2 to 3 orders of magnitude. The crossover at 138 °C occurred at 84 s into the isothermal curing process, while it took 2150 s for the crossover to be observed at 150 °C. After the observed crossover, G' and G" reached a plateau and the crystallization process was considered stabilized and complete.

Similar to the previous experiments, the rheology and Raman data were in agreement during the isothermal crystallization studies (Figures 5 and 6). The observed increase in the elastic and viscous moduli directly correlates with the increase in the normalized 808 cm^{-1} peak height. Although not shown here, a minimum in the CH stretching band intensity was again observed as the specimen transitioned from the liquid to the solid state.

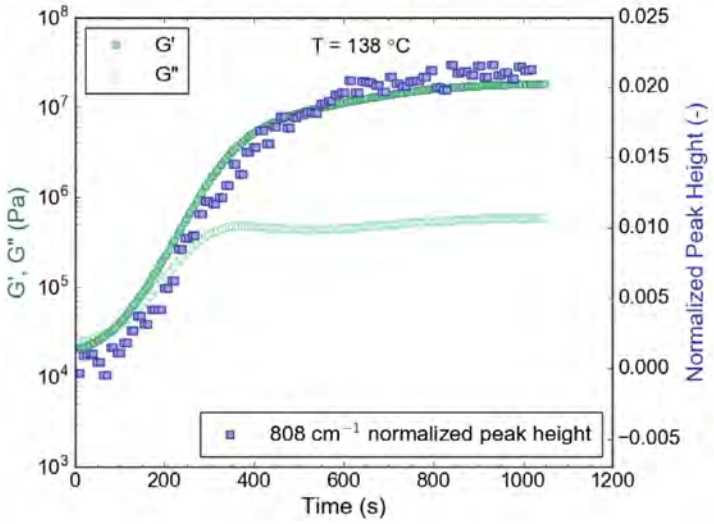

Figure 5: Polypropylene isothermal recrystallization at 138 °C : G' and G" (filled and open circles, respectively; plotted on the left y-axis) and the normalized 808 cm^{-1} Raman shift peak height (filled squares; plotted on the right y-axis) as a function of time.

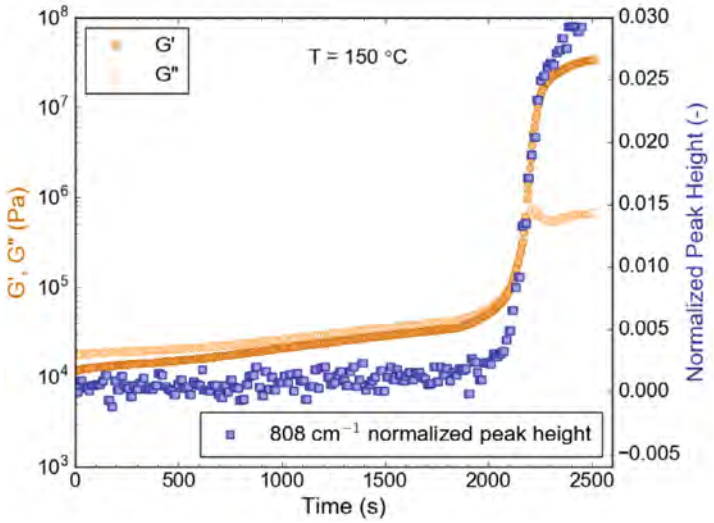

Figure 6: Polypropylene isothermal recrystallization at 150 °C : G' and G" (filled and open circles, respectively; plotted on the left y-axis) and the normalized 808 cm^{-1} Raman shift peak height (filled squares; plotted on the right y-axis) as a function of time.

thermo scientific

Conclusions

A MARSXR system was employed to simultaneously measure the rheology and Raman spectroscopy of polypropylene during the melt-to-crystallization transition process. This multimodal analytical tool allowed the bulk structural properties of polypropylene (G' and G") to be directly correlated with conformational changes at the molecular level (helical chain vibrations and CH stretching) in real-time. The data revealed that the rate of crystallization reached its maximum (indicated by rapid increases in G', G", and the normalized 808 cm^{-1} peak height) when the crystallite concentration was greatest (signified by a decrease in the overall Raman spectral intensity in the 3050-2800 cm^{-1} region). The observed correlation between the macroscopic and molecular level measurements exemplifies the unique analytical capability unleashed by hyphenating rheology with Raman spectroscopy. While this work focusses on the melting and crystallization of PP, the underlying principles demonstrated here should be applicable for a wide range of material processes including gelation, polymerization, curing behavior, as well as other shear-induced phenomena.

References

1. A.P. Kotula, M.W. Meyer, F. De Vito, J. Plog, A.R. Hight Walker and K.B. Migler, Review of Scientific Instruments, 87, 105105 (2016); DOI 10.1063/1.4903746.
2. R.A. Khafagy, Journal of Polymer Science: Part B: Polymer Physics, DOI 10.1002/polb

Find out more at **thermofisher.com/mars**

ThermoFisher SCIENTIFIC

AN52959_E 06/17M

thermo scientific

APPLICATION NOTE AN53002

Investigating cocoa butter crystallization using simultaneous rheology and Raman spectroscopy (RheoRaman)

Author

Nathan C. Crawford and
Mohammed Ibrahim
Thermo Fisher Scientific
Madison WI, USA

Keywords

Cocoa butter, crystallization, Raman spectroscopy, rheology, RheoRaman, *in situ*, storage modulus G', loss modulus G"

Thermo Fisher Scientific solutions

- HAAKE MARS 60 rheometer
- iXR Raman Spectrometer
- HAAKE RheoRaman module
- OMNIC for Dispersive Raman software

Application benefits

Simultaneous rheology and Raman spectroscopy measurements were used to examine the isothermal crystallization of cocoa butter (CB). The results indicate that CB crystallized by first hardening into an amorphous solid. The amorphous solid then underwent a morphological transition to form a crystalline solid. Without coupling these two separate analytical techniques, the observed amorphous-solid to crystalline-solid transformation would have been left undetected. Alone, each technique suggests a single-stage process, however, only when the two techniques are coupled is the multi-phase crystallization process revealed, further exemplifying the unique analytical capability unleashed by hyphenating rheology with *in situ* Raman spectroscopy.

Introduction

Cocoa butter (CB) is an edible vegetable fat extracted from the cocoa bean. CB is commonly used in home and personal care products (such as ointments and lotions) and CB is a vital ingredient in chocolate. CB forms the continuous phase within chocolate confections and is responsible for the chocolate's texture, snap, gloss, melting behavior, and resistance to fat bloom. These physical characteristics are a direct result of CB's triacylglycerol (TAG) composition and overall crystalline structure.

In general, TAG molecules assume a tuning fork configuration and the TAG "forks" assemble to form crystal lattice structures. During crystallization, the TAG molecules slow down as the CB oil cools and the TAGs come to rest in contact with one another, forming what are known as "sub crystalline cells."[1] Once the sub-cells are formed, they are thermodynamically driven to aggregate into larger and more stable crystalline structures.[2] The self-assembly of sub-cell structures and their further aggregation is governed by a balance of intra- and inter-molecular interactions. Depending on the molecular level packing and orientation of the TAGs, CB can form different types of crystal lattice structures (or polymorphs), where some crystal structures are more desirable than others. Overall, CB crystallization is a highly complex, multistage process. Understanding the isothermal crystallization behavior of CB is vital for improving chocolate manufacturing processes and maintaining product quality.

ThermoFisher SCIENTIFIC

In this note, rheology coupled with *in situ* Raman spectroscopy was used to examine the isothermal crystallization of cocoa butter. Raman spectroscopy is a highly sensitive, relatively fast, and nondestructive technique that can probe the molecular structure and conformation in both liquid and solid TAG assemblies, as well as intra- and inter-TAG interactions. With simultaneous Raman spectra and rheological data, molecular-level interactions and conformational shifts during the isothermal crystallization of CB were directly correlated with the changes in bulk viscoelastic properties, providing unique insight into the multifaceted crystallization behavior of cocoa butter.

Materials and methods

Materials

Commercially available, organic cocoa butter (*Theobroma cacao*) was acquired from Inesscents™ (Ashland, OR, USA).

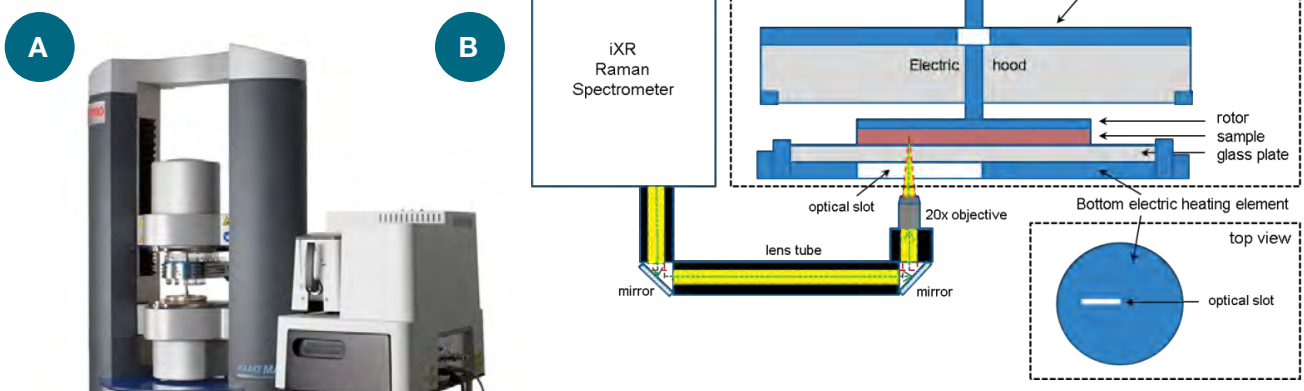

Figure 1. (a) The Thermo Scientific™ HAAKE™ MARSXR RheoRaman System. **(b)** Schematic diagram of the MARSXR RheoRaman system (showing side and top views of the rheometer sample stage). The iXR Raman spectrometer is free-space coupled to the MARS rheometer using lens tubes and mirrors that direct light into a 20x objective. The objective focuses the incoming laser (green dashed line) and collects the back-scattered Raman light (yellow) coming out of the sample sitting atop the rheometer stage.

Raman spectroscopy

Raman spectroscopy measurements were performed using a Thermo Scientific™ iXR™ Raman Spectrometer. A 532 nm laser was used with 10 mW laser power at the sample. The spectral range was 50-3500 cm^{-1}. The spectra were collected using a 2-second exposure time and 4 sample exposures. Data acquisition and processing were controlled by the Thermo Scientific™ OMNIC™ Software for Dispersive Raman. For the data presented here, Sequential Raman spectra (in parallel with the Rheological measurements) were collected over a predetermined time window using the time series collection function of the SERIES software within the OMNIC for Dispersive Raman software package.

Rheology

Rheological measurements were performed using a Thermo Scientific™ HAAKE™ MARS 60 Rheometer equipped with a serrated 35 mm diameter plate rotor at a gap height of 1 mm. The serrated plate was used to prevent slip at the sample-rotor interface. All measurements were conducted in the oscillatory mode, with a frequency of 1 Hz and a constant strain of 0.1%. CB samples were loaded onto the rheometer at 60 °C and allowed to equilibrate for 10 min to erase any crystal structures and/or shear history from sample loading. After the equilibrium step, the temperature was rapidly decreased from 60 °C to 22 °C at a rate of 10 °C/min. The temperature was then held constant at 22 °C for 120 min, collecting data every 10 s.

RheoRaman coupling

The Thermo Scientific™ HAAKE™ MARSXR RheoRaman System consists of the iXR Raman spectrometer and the HAAKE MARS 60 rheometer coupled together using the HAAKE RheoRaman module (Figure 1a). The iXR Raman spectrometer was free-space coupled to the rheometer with an optical train which used a series of mirrors to direct the incident laser into the RheoRaman module (Figure 1b). Within the module, a mirror directed the laser beam into a 20x objective, where the laser light was focused into the sample (perpendicularly to the flow or vorticity plane). Backscattered Raman light was collected using the same 20x objective and guided back to the spectrometer using the same optical train as the incident laser (eventually to the spectrograph inside the spectrometer; Figure 1b).

The sample was positioned between a sandblasted glass bottom plate and the serrated 35 mm plate rotor (the textured plates were used to avoid slip at the sample-plate interfaces). An electrical heating element within the RheoRaman module provided temperature control from below the sample, while an active electrical hood was used to provide temperature control from above (eliminating the potential for a temperature gradient within the sample). Cooling of the sample was supplied from a temperature-controlled water bath circulator.

Results and discussion

Raman spectroscopy: Cocoa butter crystallization

Raman spectra for the liquid phase CB melt and the crystalline solid CB in the 500-3100 cm^{-1} range are shown in Figure 2. Prominent Raman features were observed in both the C–H stretching region (2700-3050 cm^{-1}) and the fingerprint region (1000-1800 cm^{-1}). More specifically, the lower Raman shift features include: the carbonyl (C=O) stretching region (1700-1800 cm^{-1}), the olefinic (C=C) band at ~1655 cm^{-1}, the CH_3 and CH_2 deformations (~1460 and 1440 cm^{-1}, respectively), the CH_2 twisting region (1250-1300 cm^{-1}), and the C–C stretching region (1000-1200 cm^{-1}).

The C-H stretching regions for the melted and solidified CB specimens are highlighted in Figure 3. Two strong peaks were observed at ~2850 cm^{-1} and 2882 cm^{-1}, which are attributed to symmetric and asymmetric CH_2 stretching, respectively.[2] The symmetric vibrational modes at 2850 cm^{-1} were dominant in the liquid (melt) phase, while the asymmetric vibrations at 2882 cm^{-1} were dominant in the solid phase. Thus, the 2850 cm^{-1} and 2882 cm^{-1} bands are strong indicators of amorphous and crystalline content, respectively.[3] Subsequently, the I_{2882}/I_{2850} peak intensity ratio was used to dynamically track crystal formation during the *in situ* RheoRaman measurements.

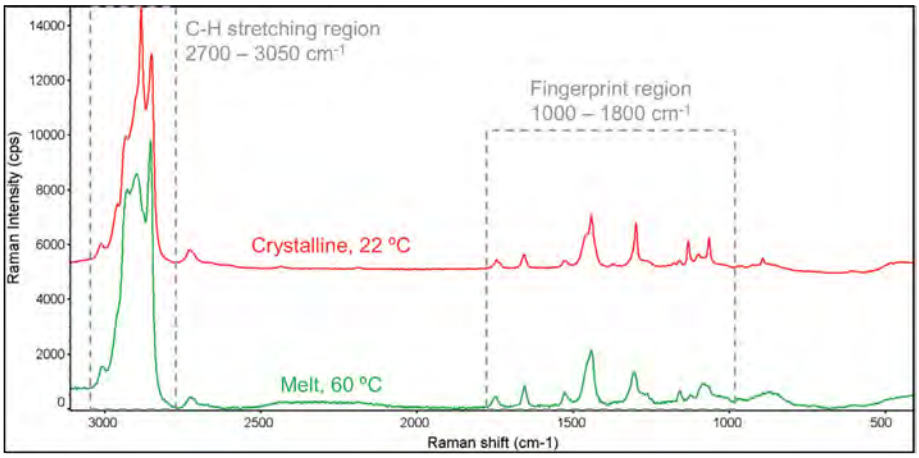

Figure 2. The full Raman spectra of melted and crystalline cocoa butter.

Figure 3. Raman spectra of the C-H stretching region (2700-3050 cm^{-1}) for melted and crystalline cocoa butter.

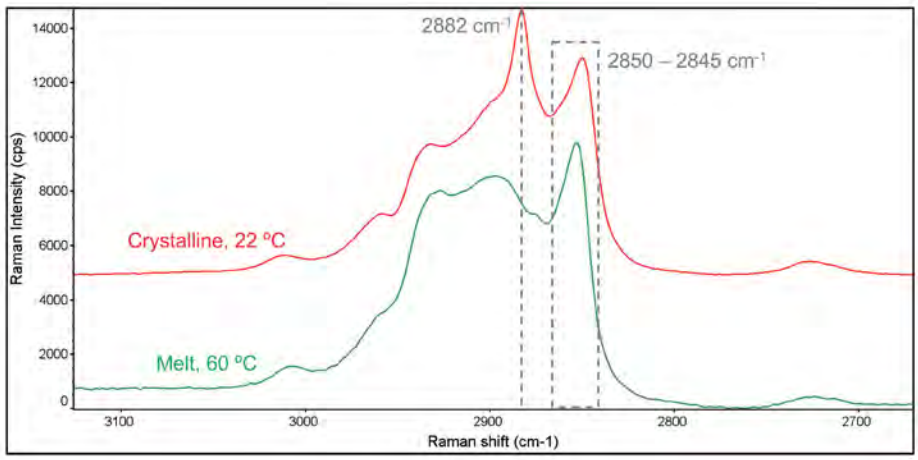

Although less intense than the C-H stretching region, approximately eight unique spectral features were identified in the fingerprint region (1000-1800 cm^{-1}; Figure 4). When comparing the CB melt state to the crystalline phase, the most significant changes were observed in the C–C stretching region (1000-1200 cm^{-1}). Two well-defined features emerged at 1130 cm^{-1} and 1063 cm^{-1} during the solidification process, which originate from the symmetric and asymmetric C-C stretching, respectively.[4,5] In the melt phase, all C-C stretching bands were relatively weak and broad due to the disordering effects of methyl gauche conformations.

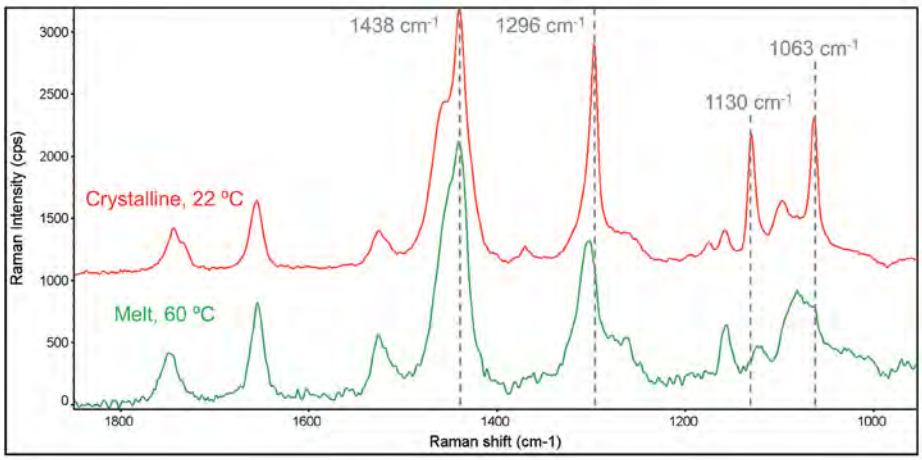

Figure 4. The 1000–1800 cm^{-1} Raman spectral range for melted and crystalline cocoa butter.

However, as the CB solidified, the backbone methyl groups were ordered into the trans-conformation, signified by the emergence of the peak at 1130 cm^{-1}. Therefore, in addition to the I_{2882}/I_{2850} peak intensity ratio, the I_{1130}/I_{2850} spectral marker was also used to track the crystalline-phase transition within CB via *in situ* rheoRaman measurements.

Simultaneous rheology and Raman spectroscopy (RheoRaman)

The melt-to-solid phase transition of cocoa butter was probed rheologically using small amplitude oscillatory shear measurements (Figure 5a), where the storage modulus G' and loss modulus G" were measured as a function of time at the isothermal temperature of 22 °C. G' and G" are measures of a material's elastic and viscous behavior, respectively. A liquid-like material will be more viscous than elastic (i.e., viscously dominated), and as a result, G" will be greater than G'. Conversely, a solid-like material will display more elastic than viscous behavior (i.e., elastically dominated), where G' will be greater than G". The overall magnitudes of G' and G", as well as their relative difference in magnitude, often reported as the ratio of G"/G', determines the general viscoelasticity and overall resistance to deformation for a given material.

The ratio of G"/G' (plotted on the right y-axis of Figure 5a) is commonly used to track viscoelasticity of a material:

$$\frac{G''}{G'} = \tan(\delta),$$

where δ is the phase angle defined as the shift or lag between the input strain and resultant stress sine waves (or vice versa) during an oscillatory shear measurement. The term "tan(δ)" is often referred to as the loss or damping factor. Values of tan(δ) less than unity indicate elastically dominant (solid-like) behavior, while values greater than unity indicate viscously dominant (liquid-like) behavior.

Unlike the individual moduli, tan(δ) can be used to quantify overall brittleness of a material and is commonly used to assess glass transition behavior. In general, as tan(δ) becomes smaller, the more G' deviates from G", and the more brittle (or glass-like) the material becomes.

During the initial portion of the isothermal hold at 22 °C from 0 to 5 min (immediately following the rapid decrease in temperature from 60 °C to 22 °C), both G' and G" increased as the CB transformed from a melted liquid to a soft semi-solid (Figure 5a). This initial increase in modulus is most likely due to a delay between the set temperature and the internal temperature of the loaded sample. Once the sample had reached thermal equilibrium and was at the isothermal set point of 22 °C, the moduli were relatively stable from 10 to 25 min. From 25 to 50 min, however, both G' and G" begin to gradually increase and then from 50 to 80 min, the moduli rapidly increased, where G' and G" increased by approximately 5 and 4 orders of magnitude, respectively. The exponential increase in the moduli indicates a solidification process, where the CB transformed from a pliable semi-solid to a more robust, hardened solid. At 80 min and beyond, growth in the elastic modulus slowed and eventually plateaued, showing no further significant change past 100 min. The viscous modulus, however, reached a slight plateau from 80 to 100 min and then proceeded to gradually decrease from 100 min and beyond.

During the increase in G' and G", a rapid decrease in the loss factor tan(δ) was observed from ~65 min and beyond (Figure 5a, right y-axis). The decrease in the loss factor indicates a deviation in overall magnitude between G' and G". As the CB hardened, the increase in G' exceeded the increase in G", triggering the decrease in tan(δ). At the end of the 120 min isothermal study, G' was more than a full order of magnitude greater than G" and the loss factor was approaching 0.01, indicating the CB had transitioned into a brittle glass-like solid.

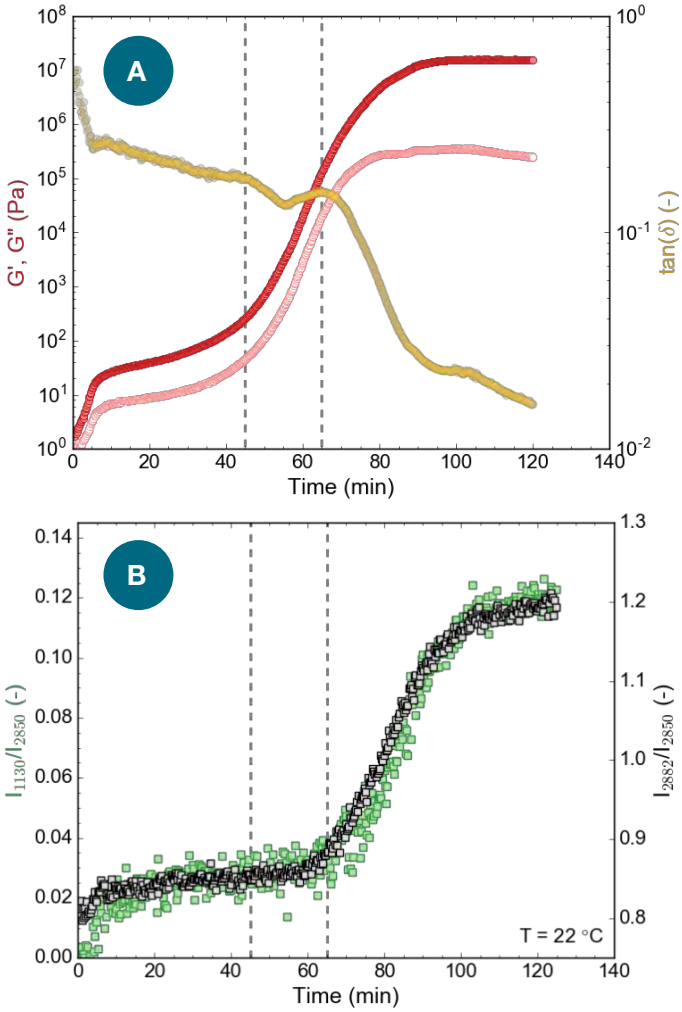

Figure 5. (a) Rheology: G' and G" (filled and open circles, respectively; plotted on the left y-axis) and tan(δ) (plotted on the right y-axis) and **(b)** Raman: the I_{1130}/I_{2850} (left y-axis, green) and I_{2882}/I_{2850} (right y-axis, black) peak intensity ratios for CB during isothermal crystallization at 22 °C. The vertical dashed line at 45 min indicates the increase of G' and G", while the dashed line at 65 min indicates the decrease in tan(δ) and increase in the Raman ratios.

The observed rheological behavior was further confirmed using simultaneous Raman spectroscopy (Figure 5b). Initially, both the I_{1130}/I_{2850} and I_{2882}/I_{2850} peak intensity ratios remained unchanged during the first ~65 min of the isothermal study. Then a sharp increase of the I_{1130}/I_{2850} and I_{2882}/I_{2850} ratios began at ~65 min, indicating the formation of crystal structures within the CB. As the CB further crystallized, both spectral markers continued to increase from 65 to 100 min. Beyond 100 min, the growth in both Raman features had subsided and the peak intensity ratios began to stabilize.

Overall, the rate of increase in the 1130 and 2882 cm^{-1} spectral ratios were similar to the rate of change for both G' and G" (i.e., they increased with similar slopes). However, there was a noticeable 15-20 min lag between the observed increase in G' and G" and the rise of the Raman intensity ratios. The sharp upturn in G' and G" indicates an increased resistance to deformation (i.e., a bulk hardening of the CB), signaling the start of the solidification process. The Raman spectral markers, on the other hand, are indicators of crystal formation. Thus, the time delay between the rheology and Raman profiles suggests that CB first hardens into an amorphous solid, followed by a transformation from an amorphous to a crystalline solid. This morphological transformation was signified by the subsequent increase in the Raman band intensities associated with crystal CB structures (the 1130 and 2882 cm^{-1} peaks). The temporal separation of the rheological and Raman spectral profiles indicates a clear distinction between bulk hardening of the CB and the formation of crystalline domains.

Interestingly, the increase in the Raman spectral features (I_{1130}/I_{2850} and I_{2882}/I_{2850}) directly correlated with the observed reduction in tan(δ) (Figure 5a and b). The loss factor is an indication of material brittleness and crystalline structures are commonly known to be brittle. Thus, it is reasonable that the formation of crystal domains at the molecular level (as indicated by Raman) coincides with the overall brittleness of the CB. As a result, the loss factor may be a more revealing indicator of bulk CB crystallization than G' and G" alone.

Conclusions

Simultaneous rheology and Raman spectroscopy measurements were used to examine the isothermal crystallization of cocoa butter. This multimodal analytical technique allowed the bulk mechanical properties of cocoa butter (G', G", and tan(δ)) to be directly correlated with conformational changes at the molecular level ($\nu_{as}(CH_2)$ mode at 2882 cm^{-1} and the ν_s(C-C) mode at 1130 cm^{-1}) in real-time. After rapid cooling (10 °C /min) and at an isothermal temperature of 22 °C, there was a noticeable time lag between the rheological response (G' and G") and the Raman spectral profiles. The observed time delay indicates that CB crystallized by first hardening into an amorphous solid, manifested by a sharp increase in G' and G" while the Raman features remained unchanged. The amorphous solid then underwent a morphological transition to form a crystalline solid, signified by the increase in Raman features associated with crystal CB structures (1130 and 2882 cm^{-1}). Without coupling these two separate analytical techniques, the observed amorphous-solid to crystalline-solid transformation would have been left undetected. Alone, each technique suggests a single-stage process, however, only when the two techniques are coupled is the multi-phase crystallization process revealed, further exemplifying the unique analytical capability unleashed by hyphenating rheology with *in situ* Raman spectroscopy. While this work focusses on the isothermal crystallization of CB, the underlying principles applied here should be applicable for a wide range of material processes including gelation, polymerization, curing behavior, as well as other shear-induced phenomena.

thermo scientific

References

1. K. Sato, *Crystallization of Lipids: Fundamentals and Applications in Food, Cosmetics, and Pharmaceuticals*. Hoboken, NJ: John Wiley & Sons, 2018.
2. S. Bresson, D. Rousseau, S. Ghosh, M. El Marssi, and V. Faivre, *Raman spectroscopy of the polymorphic forms and liquid state of cocoa butter*, Eur. J. Lipid Sci. Technol. 113, 992–1004, 2011.
3. R. G. Snyder, H. L. Strauss, and C. A. Elliger, *C–H stretching modes and the structure of n-alkyl chains*. 1. Long, disordered chains, J. Phys. Chem. 86, 5145–5150, 1982.
4. R. J. Meier, *Studying the length of trans conformational sequences in polyethylene using Raman spectroscopy: A computational study*, Polymer. 43, 517–522, 2002.
5. M. Zheng and M. Du, *Phase behavior, conformations, thermodynamic properties, and molecular motion of multicomponent paraffin waxes: A Raman spectroscopy study*. Vib. Spectrosc. 40, 219–224, 2006.

Find out more at **www.thermofisher.com/Raman**

ThermoFisher SCIENTIFIC

Other resources

Basic aspects of experimental design in Raman spectroscopy

Author

Alexander Rzhevskii • Thermo Fisher Scientific, Madison WI, USA

Abstract

This article discusses basic practical aspects of analytical instrument performance and experimental design that should be taken into consideration when characterizing microscale objects using a Raman microscope. Proper instrument alignment, optical objective magnification, confocal aperture, and sampling step settings must ensure sufficient spatial resolution and measurement precision to discriminate a Raman signal of the object from a surrounding matrix. The essential relationships between the spectral measurement parameters are considered theoretically and illustrated experimentally.

Read online ›

Spectroscopy, **2016**, Volume 31, Issue 11, p 40–45

Resonance Raman probes for organelle-specific labeling in live cells

Author

Andrey N. Kuzmin[1], Artem Pliss[1], Chang-Keun Lim[1,2], Jeongyun Heo[1], Sehoon Kim[1,2], Alexander Rzhevskii[3], Bobo Gu[1,4], Ken-Tye Yong[5], Shangchun Wen[4] & Paras N. Prasad[1]

1 Institute for Lasers, Photonics and Biophotonics, State University of New York, University at Buffalo, Buffalo, NY, 14260, USA.

2 Center for Theragnosis, Korea Institute of Science and Technology, Seoul 136-791, Republic of Korea.

3 Thermo Fisher Scientific, Waltham, MA 02451, USA.

4 Key Laboratory for Micro-/Nano-Optoelectronic Devices of Ministry of Education, School of Physics and Electronics, Hunan University, Changsha 410082, China.

5 School of Electrical and Electronic Engineering, Nanyang Technological University, 639798, Singapore.

Abstract

Raman microspectroscopy provides for high-resolution non-invasive molecular analysis of biological samples and has a breakthrough potential for dissection of cellular molecular composition at a single organelle level. However, the potential of Raman microspectroscopy can be fully realized only when novel types of molecular probes distinguishable in the Raman spectroscopy modality are developed for labeling of specific cellular domains to guide spectrochemical spatial imaging. Here we report on the design of a next generation Raman probe, based on BlackBerry Quencher 650 compound, which provides unprecedentedly high signal intensity through the Resonance Raman (RR) enhancement mechanism. Remarkably, RR enhancement occurs with low-toxic red light, which is close to maximum transparency in the biological optical window. The utility of proposed RR probes was validated for targeting lysosomes in live cultured cells, which enabled identification and subsequent monitoring of dynamic changes in this organelle by Raman imaging.

Read online ›

Sci. Rep. 6, 28483; doi: 10.1038/srep28483 (2016)

Tracking microplastics in the environment via FTIR microscopy

Authors

Michael Bradley, Suja Sukumaran, Steven Lowry, Stephan Woods
Thermo Fisher Scientific, Madison WI, USA

Abstract

Microplastics are particulates, roughly 20–1000 µm in size, originating from materials such as clothing, abrasive action on plastics, or engineered microbeads as found in some exfoliating cosmetics. The microplastics enter aquifers where the particles can be consumed by filter feeders. Microplastics are chemically stable, giving them a long lifetime in the environment and making excretion or digestion difficult. Analytically, the size and polymeric nature of microplastics makes Fourier transform infrared (FTIR) microscopy an ideal tool for detection and identification. Standard analyses typically start with a filtration step, extracting the material from the matrix. The analysis can proceed directly on the dried filter without further sample preparation. This simplicity in both sampling and analysis enables the rapid assessment of microplastic encroachment and can assist in the development of remediation techniques. We show examples from both prepared and field samples using microattenuated total reflection (ATR) FTIR.

Read online ›

Spectroscopy, **2017**, Special Issues Volume 32, Issue 8, p 17–23

Find out more at **www.thermofisher.com/ftir**

ThermoFisher SCIENTIFIC